Dissertation

Low Energy Neutrinos as geological and astrophysical Messengers

by

Kathrin Angela Hochmuth

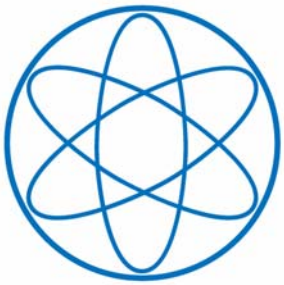

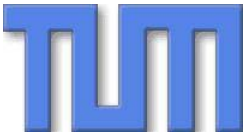

Technische Universität München
Physik Department
Institut für Experimentalphysik E15
Univ.-Prof. Dr. Lothar Oberauer

Low Energy Neutrinos as geological and astrophysical Messengers

Kathrin Angela Hochmuth

Vollständiger Abdruck der von der Fakultät für Physik der Technischen Universität München zur Erlangung des akademischen Grades eines

Doktors der Naturwissenschaften (Dr. rer. nat.)

genehmigten Dissertation.

Vorsitzender:		Univ.-Prof. Dr. Andrzej J. Buras
Prüfer der Dissertation:	1.	Univ.-Prof. Dr. Lothar Oberauer
	2.	Hon.-Prof. Allen C. Caldwell, Ph. D.

Die Dissertation wurde am 12.03.2008 bei der Technischen Universität München eingereicht und durch die Fakultät für Physik am 29.04.2008 angenommen.

Abstract

Future neutrino experiments will open up exciting possibilities to use neutrinos as messengers from diverse sources. A special focus of this thesis is put on neutrinos from the Earth's interior, the core of reactors and from the diffuse supernova neutrino background.

As a first main point, neutrinos originating from the decay of radioactive nuclei in the Earth, so called geoneutrinos, shall be discussed. These decays release a large amount of thermal energy. As the heat budget of the Earth and thus the mechanisms that e.g. power the Earth's magnetic field pose so far unresolved questions, a precision measurement of geoneutrinos that are directly linked to the heat production can deliver new information. Moreover, questions about the composition of the Earth can be answered, as presently information is only obtainable in an indirect way, i.e. via model dependent conclusions based on crustal and meteoritic samples.

We introduce a method to detect the direction of anti-neutrinos and analyze if it can be used to obtain angle dependent information on the Earth's structure. To that end we use information about the original neutrino direction that is encoded in the anti-neutrino detection reaction.

We also transfer the method of neutrino direction measurement to reactor neutrino experiments with two nuclear reactors as neutrino sources. We investigate how to monitor the individual power output of each reactor and the possibilities of locating strong neutrino sources. We also discuss, if a separation of two reactors is possible by watching the cores in "neutrino light". This proof of principle analysis could open up new ways of power reactor monitoring.

As a third main point we turn to another so far undetected source of neutrinos, namely the diffuse supernova neutrino background. These neutrinos originate from all supernovae that have occurred so far and form an overall cosmic background. We conduct a forecast of what can be learned about the supernova and star formation parameters from a measurement of both neutrinos and anti-neutrinos in future liquid scintillator detectors. The parameter space that determines the diffuse neutrino flux is large and independent measurements of the parameters do mostly not exist or are model dependent. Therefore, we conduct an analysis that considers this lack of information and gives realistic perspectives. Moreover, we show the results of an analytic fit to the diffuse neutrino spectrum, which reduces the parameter space considerably and illustrates the interdependence of the parameters. We again conduct an error forecast and relate our results to the full analysis.

Contents

Preface

Wie alles sich zum Ganzen webt, eins in dem andern wirkt und lebt!

Johann Wolfgang von Goethe, Faust, der Tragödie erster Teil

As Faust in Goethe's masterpiece, we strive to understand nature and the fundamental connections underlying everything we experience. Astroparticle and neutrino physics in particular are connecting different areas of physics and astrophysics. The neutrino, insignificant as it may seem, has had a great impact on particle physics in the last years and will continue to have this impact in years to come, with prospects that investigating the properties of the neutrinos can even shed light on fundamental questions in early universe cosmology.

This thesis is also a joint venture of different topics connecting theories concerning neutrinos from Earth and stars with large volume liquid scintillator detectors. These detector types, which presently exist in smaller versions are likely the future of neutrino experiments. In chapter 1 we give a brief introduction to the topics of this thesis concerning geoneutrinos, reactor neutrinos and diffuse supernova neutrinos. We concentrate in particular on liquid scintillator experiments, with which we intend a detection of the neutrino sources discussed here. A special focus is thereby on the proposed LENA detector, where a summary paper about the physics goals is published as

[I] T. Marrodán Undagoitia, F. von Feilitzsch, M. Göger-Neff, K. A. Hochmuth, L. Oberauer, W. Potzel and M. Wurm, "Low energy neutrino astronomy with the large liquid scintillation detector LENA," Prog. Part. Nucl. Phys. **57**, 283 (2006) [J. Phys. Conf. Ser. **39**, 278 (2006)] [arXiv:hep-ph/0605229].

The LENA detector concept is part of the LAGUNA initiative that explores the possibilities of future large volume detectors. We will discuss the detector types encompassed by the LAGUNA project in chapter 1. I am also a member of the LAGUNA project. A summary paper of detector concepts and the physics opportunities is published as

[II] D. Autiero *et al.*, "Large underground, liquid based detectors for astroparticle physics in Europe: scientific case and prospects," JCAP **0711**, 011 (2007) [arXiv:0705.0116 [hep-ph]].

In chapter 2 we discuss the properties of geoneutrinos, which are neutrinos produced inside the Earth by decays of natural radioactive elements. These neutrinos can act as a probe for the unknown structure of the Earth's interior. The LENA experiment will be able to detect a large number of these neutrinos. Moreover, we also investigate, whether a direction sensitive measurement of geoneutrinos is possible that can help to improve our knowledge further. These issues are treated in

[III] K. A. Hochmuth, F. von Feilitzsch, B. D. Fields, T. Marrodán Undagoitia, L. Oberauer, G. G. Raffelt, W. Potzel, M. Wurm, "Probing the Earth's interior with a large-volume liquid scintillator detector," Astropart. Phys. **27**, 21 (2007) [arXiv:hep-ph/0509136].

The directional spectroscopy with geoneutrinos was first discussed in

[IV] B. D. Fields and K. A. Hochmuth, "Imaging the Earth's interior: The angular distribution of terrestrial neutrinos," Earth Moon Planets **99**, 155 (2006) [arXiv:hep-ph/0406001].

Based on the techniques developed for directional measurements in chapter 2, we discuss the perspectives for the reactor neutrino experiment Double Chooz to separate its two reactors just by detecting the neutrinos in chapter 3. Thus one is able to monitor the individual power output of each reactor. Double Chooz will be the first reactor neutrino experiment of this type and thus can provide an important proof of principle for further reactor experiments. The results of this work are published as

[V] K. A. Hochmuth, M. Lindner and G. G. Raffelt, "Exploiting the directional sensitivity of the Double Chooz near detector," Phys. Rev. D **76**, 073001 (2007) [arXiv:0704.3000 [hep-ph]].

Chapter 4 is dedicated to neutrinos from supernova explosions, or more precisely to the diffuse supernova neutrino background, which is built up from all neutrinos that were released in the core collapse of supernova explosions during the history of our universe. These diffuse neutrinos might well be the next supernova neutrinos to be detected on Earth after SN 1987A. First, general properties of supernova neutrinos and the cosmic star formation history will be discussed before we will turn to the main part, an error forecast for a possible future measurement. In particular, we discuss what information can be obtained on the parameters of star formation and supernovae. This chapter also includes an extensive discussion of backgrounds expected in a liquid scintillator detector in the energy region relevant for the diffuse supernova neutrino detection. The discussion is based on

[VI] M. Wurm, F. von Feilitzsch, M. Göger-Neff, K. A. Hochmuth, T. Marrodán Undagoitia, L. Oberauer and W. Potzel, "Detection potential for the diffuse supernova neutrino background in the large liquid-scintillator detector LENA," Phys. Rev. D **75**, 023007 (2007) [arXiv:astro-ph/0701305].

The thesis concludes with a summary in chapter 5. In an appendix a short overview over the statistical methods relevant for this thesis shall be given. Moreover, we present some equations important to calculate neutrino oscillation effects.

During the time I spent as a Ph.D. student at the Max-Planck-Institut I have also worked in other areas of astroparticle phenomenology, which are not covered in this dissertation, but shall be mentioned here briefly.

Neutrino Mixing Matrices
In the field of neutrino theory and mixing we have worked on the phenomenology of Quark-Lepton Complementarity scenarios. Quark-Lepton Complementarity is the empirical relation that the sum of the solar neutrino mixing angle θ_{12} and of the Cabbibo angle, the mixing angle in the light quark sector, is equal to $\pi/2$. We have investigated two models that incorporate this relation in a natural way. In this respect, we have discussed the magnitude of branching ratios in lepton flavor violating processes and of the neutrino mixing angle θ_{13}, the prospects for neutrinoless double β-decay and leptogenesis. Especially, we have put emphasis on the discussion of possible signatures at future detectors to rule out or confirm these scenarios. The results can be found in

[VII] K. A. Hochmuth and W. Rodejohann, "Low and high energy phenomenology of Quark-Lepton Complementarity scenarios," Phys. Rev. D **75**, 073001 (2007) [arXiv:hep-ph/0607103].

Furthermore we have discussed the possibilities for a symmetric neutrino mixing matrix. This scenario is still within experimental bounds, but we expect it to be dismissed with the next generation of θ_{13}-experiments. The complete treatment can be found in

[VIII] K. A. Hochmuth and W. Rodejohann, "On symmetric lepton mixing matrices," Phys. Lett. B **644**, 147 (2007) [arXiv:hep-ph/0611030].

Finally we have discussed CP violating effects originating from bimaximal and tri-bimaximal mixing matrices in the charged lepton or neutrino sector.

These CP violating effects are connected to the magnitude of either the solar mixing angle θ_{12} or the atmospheric mixing angle θ_{23}. The results are published in

[IX] K. A. Hochmuth, S. T. Petcov and W. Rodejohann, "$U_{\rm PMNS} = U_\ell^\dagger U_\nu$," Phys. Lett. B **654**, 177 (2007) [arXiv:0706.2975 [hep-ph]].

Axion-Photon Mixing
The nature of the dark matter in the universe is still an unresolved problem. A possible candidate for dark matter could be the axion. The original axions are the Nambu-Goldstone bosons of the broken Peccei-Quinn symmetry explaining the non-observation of CP violation in strong interactions. Meanwhile, there are a number of axion-like particles under discussion that originate, for example, in some string theories. Axions and photons oscillate into each other in the presence of an external magnetic field. There are several known astrophysical sources that both emit ultra-high energy γ-rays and have strong magnetic fields. These sources are active galactic nuclei, which are ultra heavy black holes in the center of galaxies, the quiet galactic center of our Milky Way and similar galaxies or jets emitted from active galactic nuclei. These sources show characteristic spectra according to a power-law. We have investigated the effects axion-photon mixing can have on the spectra of these sources. We find that sizable gaps can occur in the spectrum, which can be detected with X- and γ-ray telescopes such as GLAST. Our complete analysis can be found in

[X] K. A. Hochmuth and G. Sigl, "Effects of axion-photon mixing on gamma-ray spectra from magnetized astrophysical sources," Phys. Rev. D **76**, 123011 (2007) [arXiv:0708.1144 [astro-ph]].

Chapter 1

Introduction

1.1 Neutrinos as messenger particles

With the beginning of the 21st century a golden era of neutrino physics has started. Finally, the solution to the long-standing questions regarding neutrino oscillations has been found. This success has initiated great activity in the field. There are numerous neutrino detectors presently running and planned for the next decades that open up exciting possibilities to detect the neutrino's intrinsic properties as well as to explore neutrino sources.

This duality in neutrino physics–the investigation of the neutrino's properties vs. the exploration of sources–has a long standing tradition. The Homestake experiment [1] was originally designed to detect solar neutrinos in order to explore the nuclear fusion cycles inside the sun. However, the unexpected small solar neutrino flux could not be explained with solar models [2]. Thus neutrino physics entered a period, where neutrino oscillations and the intrinsic properties of neutrinos became the dominant questions. Neutrino oscillations have been explored with numerous experiments such as Super-Kamiokande using atmospheric neutrinos [3], SNO using solar neutrinos [4] or KamLAND detecting reactor neutrinos [5]. Thus the magnitudes of solar and atmospheric neutrino mixing angles are well determined and there are now plans to investigate the third mixing angle, where only upper limits exist. This can be done with reactor experiments such as Double Chooz [6]. Possible CP violation in neutrino oscillations can be investigated with future long-baseline experiments, where high energy neutrinos are sent through the Earth [7, 8].

In order to oscillate neutrinos are required to be massive. This fact triggered theories exploring extensions of the standard model of particle physics explaining the neutrino mass. The question of the magnitude of the absolute

neutrino mass has been investigated by several experiments measuring the endpoint energy of the electron spectrum in beta-decays. The latest experiment, KATRIN, is supposed to measure the absolute mass with a sensitivity of 0.2 eV [9].

The introduction of neutrino masses raises more questions. When neutrinos are massless, anti-neutrino and neutrino are the same particle, apart from the helicity. The question, whether massive neutrinos are Majorana-like (neutrino and anti-neutrino are the same) or Dirac-like (neutrino and anti-neutrino are different particles) is investigated with neutrinoless double-beta decay experiments. There are numerous experiments planned to investigate the claim of the detected Majorana nature of the neutrino by the Heidelberg Moscow-collaboration [10]. The most advanced experiment with germanium crystals is GERDA, which is expected to start data taking in the beginning of 2009 [11], but also complementary studies with other isotopes are advancing quickly [12].

The neutrino has also impact on early universe cosmology, as the explanation of the smallness of the neutrino mass requires the introduction of heavy Majorana neutrinos, which in turn can help to explain the baryon asymmetry with their decays in the early universe [13]. Though, most of these theories can not be directly proven with experiments, there is great activity in this field that may ultimately lead to a theory consistent with all observations.

In recent years, however, the role of neutrinos as messenger particles to investigate diverse sources is rediscovered. This development encourages several plans to build large volume detectors that are able to obtain high statistics. Neutrinos can bring tidings in a wide energy range from the highest cosmic ray energies down to the sub-MeV scale. The highest energy ranges can be explored with neutrino telescopes such as IceCube [14], which is presently under construction at the south pole. With these neutrinos distant sources, such as quasars, and their distribution in the sky can be detected and questions about the emitters of high energy cosmic rays can be answered. On the low energy side of the spectrum, solar ^{7}Be neutrinos with an energy of 862 keV have been detected for the first time with Borexino, confirming the solar model with neutrino oscillations [15].

In this thesis we discuss anti-neutrinos in the low energy region from 1.8 to several 10 MeV that can be detected in liquid scintillator detectors via the inverse beta-decay reaction

$$\bar{\nu}_e + p \rightarrow n + e^+ \,. \tag{1.1}$$

This reaction has an energy threshold of 1.8 MeV, but has the advantage of delivering a clear coincidence signal with a prompt positron annihilation

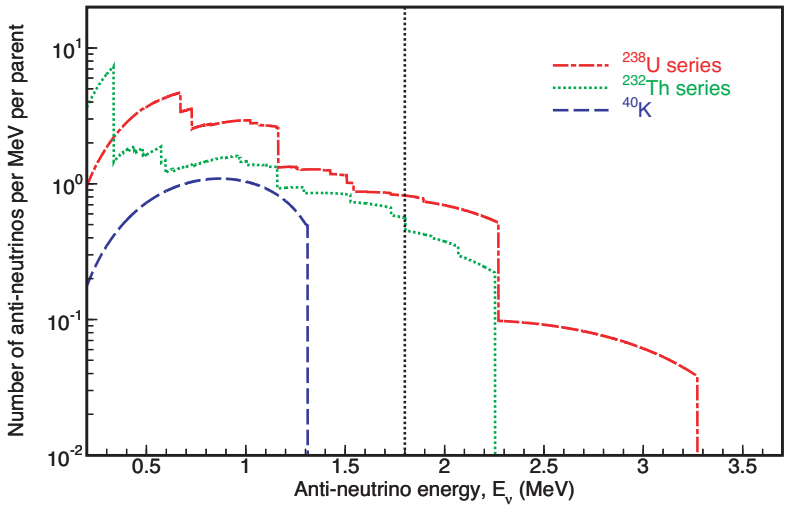

Figure 1.1: Energy spectrum of geoneutrinos. The vertical dotted line indicates the detection threshold at 1.8 MeV. Picture from [17].

event and delayed neutron capture. After scattering and thermalization the neutron released in reaction (1.1) is captured by a proton. Moreover, in this reaction the neutron is scattered in the forward direction with respect to the incoming neutrino, which allows one to obtain angle-dependent information on the position of the neutrino source. In this thesis we use neutrinos as messengers to obtain information about three neutrino sources: the Earth's interior, the core of nuclear power plants and the diffuse supernova neutrino background.

Geoneutrinos originate from the decays of natural radioactive isotopes inside the Earth. On first thought it may seem surprising that only little is known about the Earth's interior. However, information can only reach us in indirect ways, i.e. via extrapolation of isotope measurements in terrestrial surface samples and model dependent conclusions. The Earth's heat budget, the distribution and abundance of radioactive isotopes or the mechanisms governing the Earth's magnetic field are largely a mystery. Therefore, a measurement of the geoneutrino flux that is directly linked to the heat production inside the Earth would help to resolve open questions. Especially an angle dependent measurement of the geoneutrino flux could help to locate areas with a high radioisotope content. In the inverse beta-decay reaction, the main anti-neutrino detection reaction, information about the neutrino's initial direction is encoded, which we will explore in detail for the first time in the

context of geoneutrino detection[1]. In Fig. 1.1 we show the energy spectrum of geoneutrinos. The highest neutrino energies extend to 3.4 MeV and we have to consider a lower detection threshold of 1.8 MeV.

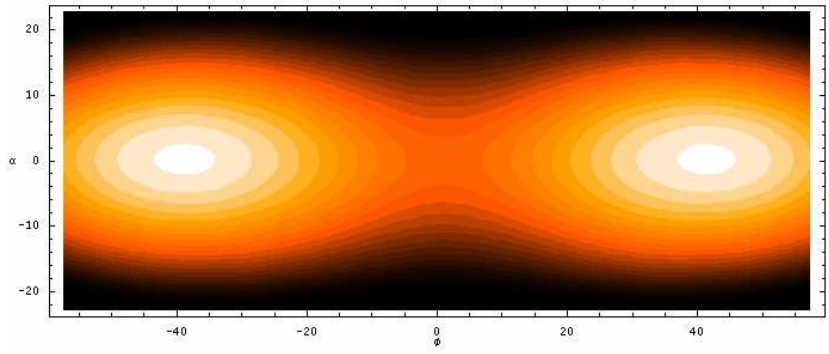

Figure 1.2: Artist conception of two reactor cores seen in neutrino light. The reactors are separated by an angle of about 90°.

We have extended the principles of angle dependent measurements to locate the cores of nuclear power plants just by looking at their neutrinos. For the first time, we investigate in detail the imaging power for the Double Chooz near detector with two reactor cores. The CHOOZ experiment has first measured this effect with a single reactor source and only 2,500 events [18]. In future reactor experiments, event rates of more than 10^6 can be expected per year. However, though the imaging of a single source is straightforward, the resolution of multiple source is a highly non-trivial exercise. We show an artist conception of two reactor cores as seen in "neutrino light" in Fig. 1.2.

With the diffuse supernova neutrino background (DSNB) we present a so far undetected source of neutrinos. These neutrinos have accumulated since the first supernova explosions and are detectable in an energy window between about 10–26 MeV in a liquid scintillator detector. Below 10 MeV we have the influence of reactor neutrinos and above about 26 MeV one is dominated by atmospheric neutrinos. In Fig. 1.3 we show the expected fluxes for different DSNB spectra resulting from numerical supernova simulations [19, 20, 21] and the expected backgrounds. Moreover, we show the upper limit on the flux above 19.3 MeV obtained by Super-Kamiokande [22]. A measurement of the diffuse neutrinos would be an exciting step towards confirming our beliefs about star formation and supernovae. We will investigate the information content on mean supernova neutrino energy, binding energy and

[1] Measuring the angle dependent fluxes of geoneutrinos has first been proposed by Fields and Hochmuth [16].

star formation parameters that is encoded in the DSNB. For the first time in this sector of neutrino physics, we apply a method that has previously been used in forecasting the performance of neutrino oscillation experiments.

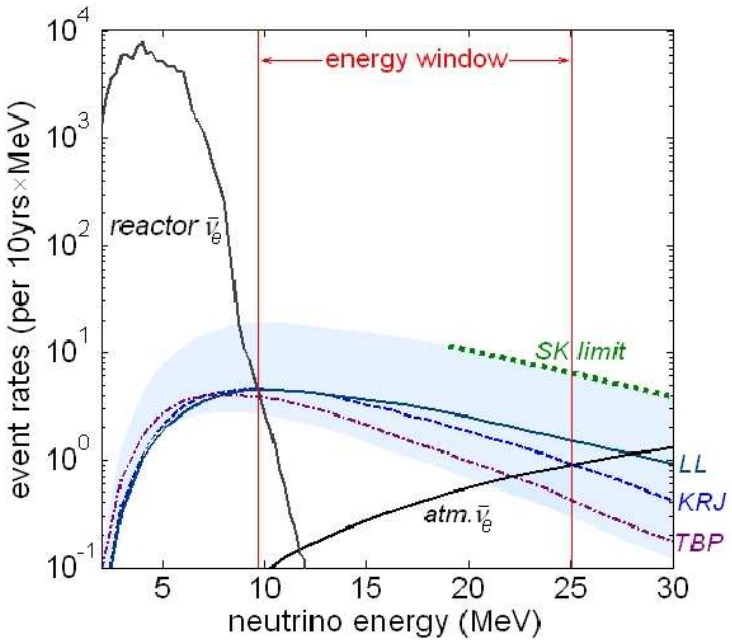

Figure 1.3: Comparison between the event rates of reactor, atmospheric and diffuse neutrinos for different supernova simulations as expected for LENA in Pyhäsalmi. The shaded region represents the uncertainties of the DSNB rates due to the star formation parameters. The Super-Kamiokande limit is indicated as green dotted [22]. A larger DSNB flux, e.g. close to the Super-Kamiokande bound, would considerably widen the energy window [23].

1.2 Low energy neutrino experiments

1.2.1 Liquid scintillator detectors

Numerous experiments have already explored the possibility to use scintillation light emitted after particle interactions in diverse materials. Excited molecules of scintillating materials emit photons that are subsequently detected with photomultipliers. Particularly well-suited materials for neutrino detection are liquid mineral oils that can reach a high radio-purity, are operational at room temperature and are available in large quantities. Experiments

like Borexino or KamLAND that are currently under operation and future experiments such as Double Chooz, SNO+ or LENA are developing and using these techniques successfully. We will only briefly introduce some principles of liquid scintillator technologies as we will return to this discussion in the subsequent chapters.

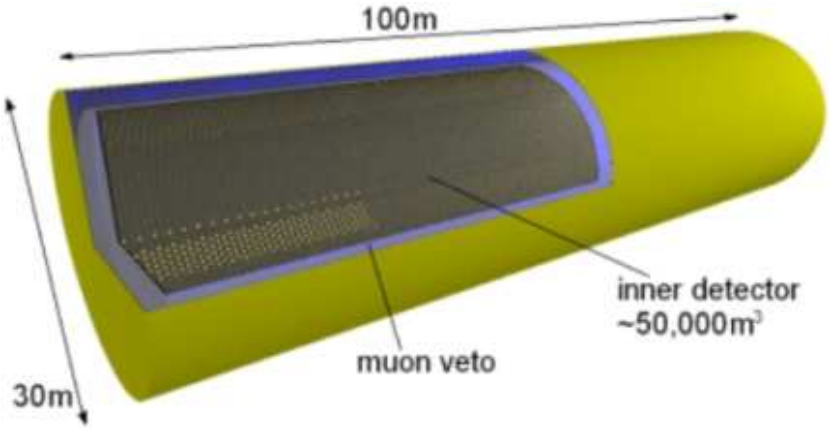

Figure 1.4: Schematic view of the LENA detector. With a length of $\sim$ 100 m and a diameter of $\sim$ 30 m the LENA detector is supposed to hold roughly 50 kton of liquid scintillator monitored by 13,000 photomultiplier tubes.

One option for the proposed LENA detector (Low Energy Neutrino Astronomy) [24] is to use a scintillator based on PXE (phenyl-o-xylylethane, $C_{16}H_{18}$). PXE has a high light yield, is non hazardous, has a relatively high flashpoint of 145°C, and a density of 0.985 g/cm^3 [25]. A possible admixture of dodecane ($C_{12}H_{26}$) increases the number of free protons and improves the optical properties. A blend of 20% PXE and 80% dodecane shows a decrease in light yield of about 20% relative to pure PXE, an attenuation length of about 11 m and an increase in the number of free protons by 25% [26]. In PXE-based scintillators the neutron is captured by a proton with nearly 100% efficiency within an average time interval of about 180 μs, subsequently emitting a 2.2 MeV gamma [25, 27]. However, one can also put an additive into the scintillator to enhance the detectable energy of the delayed-neutron signal. Both lithium [28] and gadolinium [18] loaded scintillators have been used in this way for neutrino experiments or are planned in the future [29]. With a concentration of about 0.1% by mass, Gd captures neutrons with 90% efficiency and isotropically emits a total energy of about 8 MeV in a gamma cascade with an average number of 3 photons. Note however, that in a Gd-loaded PXE/dodecane scintillator the light yield is reduced by typically

10–20% compared to an unloaded scintillator [27].

The LENA detector is supposed to hold approximately 50 kton of liquid scintillator that are monitored with roughly 13,000 photomultiplier tubes. A schematic view of the LENA detector can be seen in Fig. 1.4. A possible location for this experiment is the Pyhäsalmi mine in Finland. The physics goals of LENA encompass, for example, solar neutrino spectroscopy, the detection of proton decay [30], the observation of the first galactic supernova in "neutrino light" and the detection of geoneutrinos and diffuse supernova neutrinos [23]. It has also been under discussion to use the LENA detector for long-baseline neutrino oscillation experiments, where high-energy neutrino beams from accelerators are sent through the earth over distances of several hundred to thousands of kilometers [31]. With long-baseline experiments one could measure for example CP violation in ν oscillations. The LENA project is also part of the LAGUNA initiative, which will be discussed in Sec. 1.2.2.

Figure 1.5: Double Chooz site in France with near and far detector locations.

Double Chooz

The reactor neutrino experiment Double Chooz is designed to measure the last missing neutrino mixing angle $\sin^2 2\theta_{13}$ to a sensitivity below 0.03 in three years of run time [6]. The concept foresees two identical detectors, a near detector at a distance of $\sim$ 280 m and a far detector at a baseline of $\sim 1,050$ m to the reactor cores in order to reduce systematic errors. The near detector monitors the neutrino flux and the spectral shape without oscillations, whereas the far detector can access the spectrum after oscillations. The far detector will be operational in 2009, three years before the near detector

will start data taking. Both Double Chooz detectors will consist of about 10 tons of Gadolinium-loaded scintillator, with a Gd concentration of 0.1%. The detector site in France, close to the Belgian border, already hosted the preceding experiment CHOOZ, which had only one (far) detector. Figure 1.5 shows the detector site of Double Chooz and the locations of the near and far detectors.

Borexino

The solar neutrino experiment Borexino has started to take data at the Gran Sasso underground lab in spring 2007. Borexino uses 300 t of pseudocumene as a scintillating material with 1.5 g/l PPO as a wavelength shifter. As its first results Borexino presented the first real-time measurement of solar ^{7}Be neutrinos. This is the first spectral measurement in the sub-MeV region and confirms with $47 \pm 7_{\text{stat}} \pm 12_{\text{sys}}$ counts/(day$\cdot$100 ton) the standard solar model with ν oscillations [15]. As more than 99% of the solar neutrino flux is at energies below 2 MeV, this measurement is a first step towards precision monitoring and tests of the solar model. The lower limit for detection is 200 keV, as below this limit decays of ^{14}C intrinsic to the scintillator start to become important. Further physics goals of Borexino encompass the detection of neutrinos from the solar CNO cycle or geoneutrinos.

MiniBooNe

The MiniBooNe detector at the Fermi National Accelerator Laboratory consists of 800 tons of liquid scintillator [32]. MiniBooNe was designed to test the claim of the LSND experiment of a 4th (sterile) neutrino family that mixes with the three known families [33] and searches for ν_e appearance in an ν_μ-beam. MiniBooNe could not confirm the original claim of LSND of two neutrino appearance-only oscillations but still sees a so far unexplained excess of electron neutrinos at low energies [32].

1.2.2 LAGUNA initiative

The future of neutrino detection will be in the development of large volume detectors to increase event rates and statistics. These detectors, of course, are not built for a single measurement, but are supposed to be as versatile as possible to obtain new information on neutrinos and on other open questions, such as proton decay [30]. To explore, what type of detector has the greatest feasibility and to share R&D resources the LAGUNA (Large Apparatus for Grand Unification and Neutrino Astronomy) initiative has been started [34].

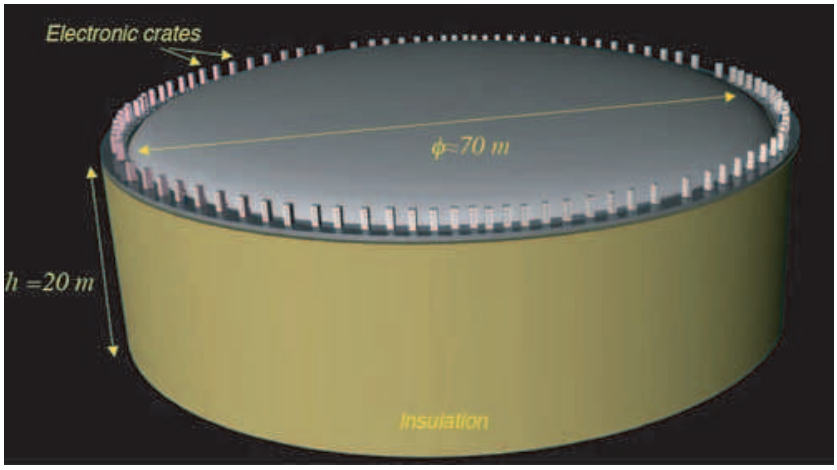

Figure 1.6: Schematic view of the proposed liquid argon experiment GLACIER.

There are three concepts of large volume detectors that are presently under discussion: A 50 kton liquid scintillator detector, a 100 kton liquid argon detector and a 1 Mton water Cherenkov detector. The three detector types shall be discussed briefly. The detection techniques of the 50 kton liquid scintillator detector LENA have been discussed Sec. 1.2.1.

The liquid argon experiment GLACIER (Giant Liquid Argon Charge Imaging Experiment) uses the time projection chamber technique with 100 kton of liquid argon at boiling point. A schematic view is shown in Fig. 1.6. Events are reconstructed in three dimensions by using ionization traces of particles (similar to a bubble chamber), scintillation and Cherenkov light [34]. Neutrinos are detected via capture on argon (charged current interaction) or elastic scattering on argon (neutral current interaction). The two main detection channels for neutrinos and anti-neutrinos are

$$\begin{aligned} \nu_e + {}^{40}\mathrm{Ar} &\rightarrow {}^{40}\mathrm{K}^* + e^- \\ \bar{\nu}_e + {}^{40}\mathrm{Ar} &\rightarrow {}^{40}\mathrm{Cl}^* + e^+ \,. \end{aligned} \tag{1.2}$$

Neutral current cross sections have approximately the same order of magnitude for all flavors below energies of 10 MeV. For the energy range that we consider in this thesis (20–40 MeV) they play a subdominant role, as they are roughly three orders of magnitude weaker than the charged current cross sections [35]. Figure 1.7, which is taken from Ref. [35] shows the cross sections up to 100 MeV. The dominant cross section is the one for electron neutrinos.

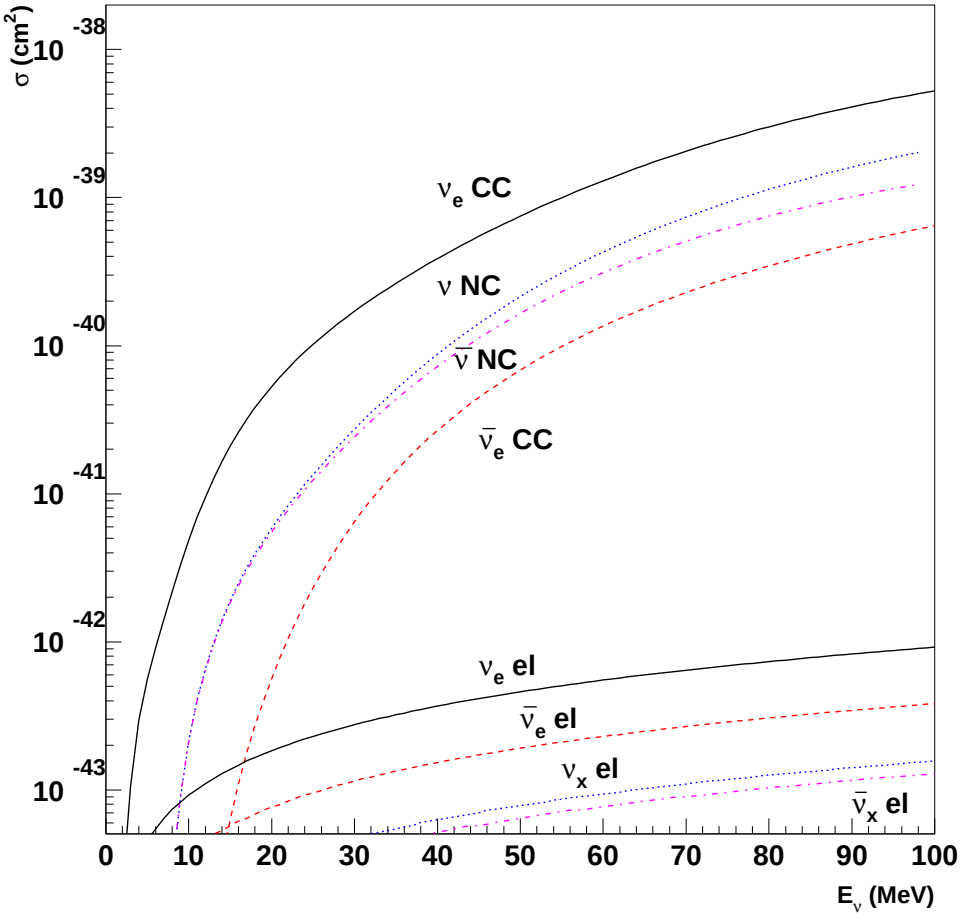

Figure 1.7: Cross section for neutrino and anti-neutrino elastic scattering as well as charged and neutral current interaction on argon. Shown is only the lower energy range. Figure taken from [35].

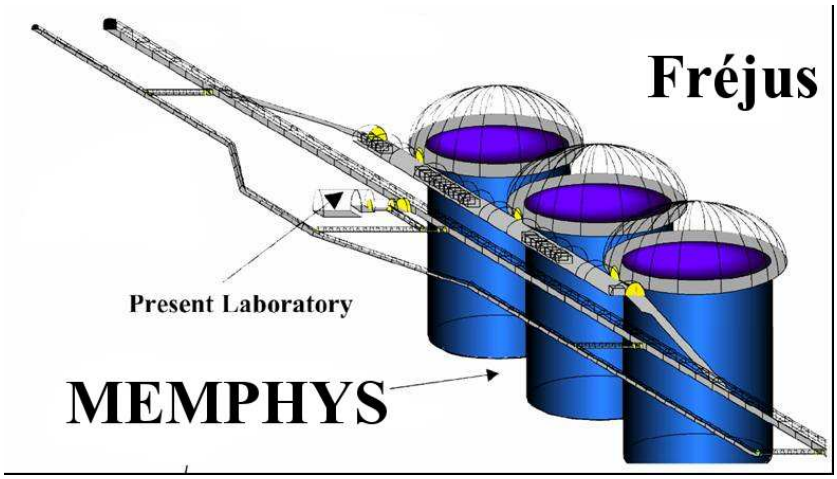

Figure 1.8: Schematic view of the megaton water Cherenkov project MEMPHYS.

The 1 Mton water Cherenkov project MEMPHYS (MEgaton Mass PHYSics) is an enlarged version of the Super-Kamiokande detector, but because of its size probably with multiple water tanks (see Fig. 1.8). The dominant anti-neutrino detection channels are again the inverse β-decay process, Eq. (1.1), and the capture on oxygen

$$\bar{\nu}_e + {}^{16}\mathrm{O} \rightarrow X + e^+ \,. \tag{1.3}$$

However, the detection threshold of water Cherenkov detectors lies above ~ 4 MeV, because of intrinsic radiation in the water. Hence, the neutron of reaction (1.1) cannot be detected. It is under discussion to add gadolinium trichloride to the water [37]. As discussed in Sec. 1.2.1, a neutron capture on gadolinium releases ~ 8 MeV, which is above the 4 MeV threshold. The summary paper Ref. [34] deals with these three detector types and carries out a comparison.

Chapter 2

Geoneutrinos in LENA

On first thought it may seem surprising that the Earth's interior is still not fully understood and that the processes and mechanisms governing the Earth are still a mystery. Information from the Earth's interior can only reach us in an indirect way, e.g. via extrapolation of isotope measurements in terrestrial surface samples. On the other hand, advancing technologies in neutrino physics have opened up a new method to probe the interior of the Earth. There are large numbers of neutrinos released by the decays of natural radioactive elements throughout the Earth that can help to gain more information on the heat budget and the radioactive isotope abundance. These so called geoneutrinos can be detected in liquid scintillator detectors such as LENA. At the moment, LENA has the greatest perspective to conduct a precision measurement of geoneutrinos, as high event rates are expected because of the large target mass. Liquid Argon and water Cherenkov detectors are not suitable for this task as geoneutrinos are below the energy threshold of these experiments.

In this chapter the present knowledge of the Earth's interior shall be discussed and models for the radioactivity content shall be introduced. We discuss the possibilities of an angle dependent measurement of the anti-neutrino flux in liquid scintillator detectors and investigate to what extent a liquid scintillator detector like LENA is sensitive to the angular dependence of the geoneutrino flux[1].

[1]This chapter is based on K. Hochmuth, F. v. Feilitzsch, B. Fields, T. Marrodán Undagoitia, L. Oberauer, W. Potzel, G. Raffelt and M. Wurm, Astropart. Phys. **27**, 21 (2007) and on B. Fields and K. Hochmuth, Earth Moon Planets **99**, 155 (2006)

2.1 The Earth's interior

First, we discuss what is presently known about the Earth's interior. The Earth has a radius of about 6,371 km. 70% of its surface are covered by water. The outermost layer of the Earth is the crust, which again can be divided into three parts on the continents (upper, middle and lower continental crust). Underneath the oceans lies the thin oceanic crust. The crust is covered by sediments of various thickness ranging from a few meters to several kilometers (see sediment map in [38]). Going deeper into the Earth one has the layers of the upper and lower mantle followed by the liquid outer and the solid inner iron core (see Fig. 2.1). The Earth has a total mass of 5.97×10^{24} kg, where

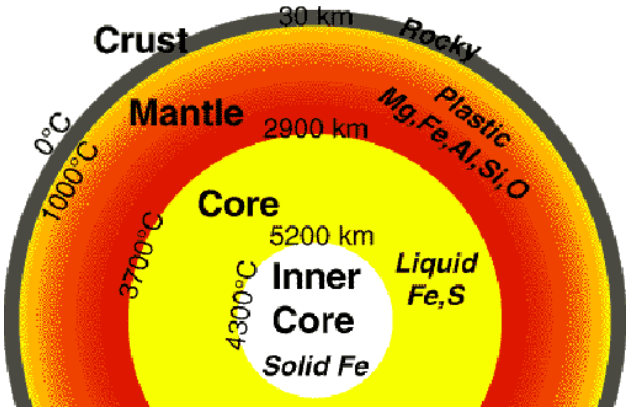

Figure 2.1: Schematic view of the structure of the Earth, picture from [41]

the core accounts for about 32%, the lower mantle for almost 50% and the upper mantle for 18%. The remainder ($\approx 0.4\%$) belongs to the crust [39].

First let us consider the Earth's iron core. It was noticed that acoustic scherwaves (transversal waves) only go down to a depth of 2,900 km [40]. As transversal waves cannot propagate through liquids the existence of a liquid zone (the outer core) was established. The solidity of the inner core was ascertained in 1936, as it was noted that compression waves (longitudinal waves) can propagate through the liquid outer core, but show a sudden increase in velocity at around 5,200 km. This led to the conclusion that the waves encounter a solid barrier, namely the inner core. The density of the core was rather well measured by monitoring seismic activities.

Information about the lower mantle, which extends from a depth of almost 700 km to about 2,900 km, is again based on the behavior of seismic waves. The upper mantle, which has a thickness of roughly 700 km, is the first layer where one has direct samples and therefore can investigate its composition in

greater detail. These samples mainly originate from volcanic regions. Apart from an increase in density due to the increase of the gravitational force, one expects the lower mantle to be similar to the upper mantle. The concentration of iron oxides is supposed to rise the closer one gets to the core.

The crust is the outermost layer of the Earth. The continental crust with a thickness of 40–70 km is again divided into three layers: upper, middle and lower crust. The continental crust is rather inhomogeneous, due to different phenomena like plate tectonics (subduction zones) or mountain regions. The oceanic crust has a thickness of only 6–10 km. Clearly, information about the continental crust is obtained easiest. But one has to note that the deepest drill holes (e.g. in Windischeschenbach, Germany) are only about 10 km deep. A schematic view of the Earth's layers and the temperatures inside can be seen in Fig. 2.1.

According to the model for the Earth's creation, the clump of material that formed the proto Earth was heated by radioactive decays and collisions with smaller objects. At the high initial temperatures ($\approx 2,000\,^{\circ}\mathrm{C}$), silicates (silicon-oxygen compounds) and metals were molten. The molten elements divided into a lithophile phase (elements that like to attach to silicates) and a siderophile phase (elements that like to attach to iron). As the siderophile phase is heavier it started to sink to the core [42]. This behavior explains the layering of the Earth. A detailed density profile of the Earth, the Preliminary Reference Earth Model (PREM), was constructed by Dziewonski and Anderson in 1981 by monitoring seismic activities [43].

The determination of the Earth's composition is based on multiple geological considerations, only few of which shall be presented here in short. A major aspect is to examine meteorites of various kinds. Especially carbonaceous chondrites[2] are used, which formed in the early days of the solar system and therefore represent the chemistry of sun and solar system most closely. They contain most of their elements in the form of silicates, which are the main compounds found also in crust and mantle. Another important aspect is of course to examine available terrestrial samples.

Based on this information and numerous crustal samples, geologists have deduced a model for the distribution and concentration of elements in the Earth called the Bulk Silicate Earth Model [45]. According to this model, radioactive elements can only be found in crust and mantle. We will discuss this model more deeply in the following.

[2]Carbonaceous chondrites are a primitive and mostly unaltered type of stony meteorites. They are probably the oldest objects in the solar system and are supposed to consist of the same materials as the proto solar system. For a classification of meteorites see [44].

Table 2.1: Important ν-emitting radioactive nuclides [46]. The branching ratio is 100% unless otherwise specified.

isotope	decay-chain	decay energy [MeV]	branching ratio
^{234}Th	U	0.273	
^{234}Pa	U	2.271	
^{214}Pb	U	1.024	
^{214}Bi	U	3.272	99.98%
^{210}Pb	U	0.064	
^{210}Tl	U	5.484	0.02%
^{210}Bi	U	1.163	
^{218}Po	U	0.265	0.02%
^{218}At	U	2.883	0.1% × 0.02%
^{228}Ra	Th	0.046	
^{228}Ac	Th	2.127	
^{212}Pb	Th	0.574	
^{212}Bi	Th	2.254	64.06%
^{208}Tl	Th	2.4	35.94%

2.1.1 Distribution of radionuclides in the Earth

Radioactive nuclides originating from supernova explosions have been incorporated in the Earth at its very beginning. The abundances of these nuclides have been established by mass spectroscopy of numerous probes. The dominant radioactive isotopes are ^{238}U, ^{232}Th and ^{40}K because of their high abundance and their long life-times. Although neutrinos from ^{40}K decays are not suitable for the geoneutrino measurement, as their energy lies below the threshold of the detection reaction Eq. (1.1), we include it for now in the discussion of geoneutino sources.

In Tab. 2.1 we list the neutrinos[3] released in the ^{238}U and ^{232}Th decay chains and the corresponding branching ratios. In total one has six neutrinos from the uranium and 4 from the thorium chain. In Tab. 2.2 the life-times and some important properties of these nuclides are displayed. Since the Earth's creation 4.5 Gyr ago these isotopes have decayed, thereby heating the Earth. The present-day heat loss through the Earth's surface is about 40 TW or 82 mW/m^2. But also lower values of 31 TW are under discussion [47], as the heat output under the oceans is not precisely known. To obtain these values for the heat loss, samples of the surface temperature and elemental composition

[3]Though geoneutrinos are of course anti-neutrinos, we will call them just neutrinos throughout this chapter.

of multiple places around the world are taken, whereas information on the bottom of the oceans is mostly extrapolated. The abundance ratios of the

Table 2.2: Properties of the main geoneutrino source nuclei [46].

isotope species	life time τ [Gyr]	released $\bar{\nu}_e$ n_i	isotopic abundance
^{40}K	1.84	1	0.0117%
^{238}U	6.45	6	99.2745%
^{232}Th	20.3	4	100%

radioactive elements in the Bulk Silicate Earth Model are Th/U ≈ 4 and K/U $\approx 1.14 \times 10^4$. According to the Bulk Silicate Earth Model there are only radioactive isotopes in the crust and mantle, as they are lithophile [45]. The core is not assumed to contain any significant amount of uranium, thorium or potassium. However, only 20 TW of the total energy are attributed to be produced by radioactive decays.

It is a matter of intense discussion, whether the heat generation is solely due to the decay of radioactive elements or whether there is also a contribution of primordial heat from the Earth's early days. The ratio of the heat production due to radioactivity to the total heat flow at the surface is known as the Urey ratio. In the Bulk Silicate Earth Model the Urey ratio is assumed to be 0.5, because according to this model only 20 TW of the Earth's heat is produced by radioactive decays. But other estimates take the Urey ratio to be much closer to 1 (around 0.8) [48, 49]. As the flux of geoneutrinos is directly linked to the number of radioactive decays and thus the generated heat, it is of great interest to measure these geoneutrinos. Hence one might be able to deduce the main contributor to the heat production.

Generally, one can obtain an approximate energy output per decay chain when summing the individual decay energies (see e.g. [46]), which are dominated by the α-decays as

$$E(\mathrm{U}) = 51.1 \text{ MeV} \tag{2.1}$$

$$E(\mathrm{Th}) = 42.7 \text{ MeV}\,. \tag{2.2}$$

In the case of potassium one has to take more care, as ^{40}K has two decay modes, one being electron capture to ^{40}Ar, the other β^--decay to ^{40}Ca. Taking the Fermi function for the β-decay one obtains a mean neutrino energy of 0.598 MeV [50] in 89% of all decays. The other 11% are delivered by electron capture with an energy of 1.505 MeV, thus giving a weighted average energy of

$$E(\mathrm{K}) = 0.69 \text{ MeV}\,. \tag{2.3}$$

Taking these energy values and the life times of the longest lived elements in the decay chain, which are ^{238}U and ^{232}Th (see Tab. 2.2) one obtains an equation for the total heat production H in units of TW, where $M(\mathrm{U})$, $M(\mathrm{Th})$, $M(\mathrm{K})$ is the total mass in units of 10^{17} kg of uranium, thorium and potassium respectively

$$H \approx \left[10 \frac{M(\mathrm{U})}{10^{17}\mathrm{kg}} + 2.7 \frac{M(\mathrm{Th})}{10^{17}\mathrm{kg}} + 3.4 \times 10^{-4} \frac{M(\mathrm{K})}{10^{17}\mathrm{kg}} \right] \mathrm{TW}\,. \qquad (2.4)$$

Based on the assumption of the Bulk Silicate Earth Model that 50% of the heat production is due to radioactive decays the total amount of uranium, thorium and potassium in crust and mantle is estimated to be: $M(\mathrm{U}) = 0.81 \times 10^{17}$ kg, $M(\mathrm{Th}) = 3.16 \times 10^{17}$ kg, $M(\mathrm{K}) = 0.49 \times 10^{21}$ kg. As the composition and abundances of the crust is believed to be understood rather well and as mantle samples are rare, one deduces the abundances for the mantle with mass estimates and elemental ratios that are believed to be constant [51] (and references therein). The mantle thus turns out to be depleted in radioactive isotopes.

There are various estimates for the abundances of uranium, thorium and potassium in crust and mantle[4], which differ by factors of 2–3. The maximum measured abundance values deliver a heat generation of approximately 40 TW originating from crust and mantle. We will return to this discussion when we introduce the geophysical models that can be investigated with LENA.

2.1.2 Radioactivity in the core

The core is believed to be responsible for the magnetic field of the Earth. However, the sources of the magnetic field are not fully understood, and the field seems to be generated in a complex interaction between core and mantle. The core itself is too hot to sustain a permanent magnetic field. Therefore, it is assumed that the magnetic field is powered by a geodynamo, where in a simplified picture the magnetic field is generated by the moving liquid outer core [52]. But there are several problems with this picture. One of them is how the energy for the geodynamo is provided. Taking energy from the inner core leads to a cooling and thus to a solidification of the core. But this process is constrained by the present day size of the inner core, leading to the conclusion that the core can be no older than 1.7 Gyr [52], which is obviously much less than the real age of Earth and core of more than 4 Gyr. This leads

[4] One can get an excellent overview of these abundances and their spread in the GERM Reservoir Data Base [51].

several authors to the conclusion that there are radioactive elements in the core providing heat and sustaining the geodynamo (see e.g. [52]).

There are further hints that radioactive isotopes might be hidden in the core. In comparison to meteoritic samples the crust and mantle are fairly depleted in potassium. Wasserburg *et al.* [53] found in 1964 that the potassium to uranium ratio of crust and mantle is 8 times lower than in chondrites. At first it was assumed that the volatile character of potassium led to a depletion during the Earth's formation [45]. This assumption was quickly ruled out, as the abundance ratios of all potassium isotopes largely stay the same in all samples, be it lunar, chondritic or terrestrial [54]. However, one would expect a lighter isotope to evaporate more easily.

Another idea would be that under certain conditions potassium can be incorporated in the core [55, 56]. Taking a potassium concentration as it is found in chondrites one would expect the core to contain 1,200 ppm of potassium [57]. According to Eq. (2.4) this would lead to a heat production of 8 TW.

It is assumed that core formation took place under high pressure conditions of 26–60 GPa and at temperatures between 2,100–3,900 °C [58]. In 1976, it has been proposed by Bukowinsky on a quantum-mechanical basis that potassium is able to form alloys with iron under high pressures and temperatures [59]. Under these conditions the valence electron of potassium is somewhat pressed into the inner electron shells thus giving potassium a more siderophile character. Although for a long time there had been no experimental evidence that such a process is actually possible, it has been shown recently under laboratory conditions that indeed potassium-iron alloys can form in an environment that was present at the Earth's creation. There are two different experimental approaches, which have been used to investigate this possibility.

Gessmann and Wood [57], as well as Rama Murthy, van Westrenen and Fei [58] have shown that in the presence of iron-sulfur alloys under a high pressure ($\approx$ 2 GPa) and temperature environment ($\approx$ 1,600 °C) potassium can be dissolved in iron melts. It seems to be the case that a potassium-sulfur molecule is built, which then again has a siderophile character. The authors of [58] find values of 60–130 ppm potassium in the melt. With a core mass of about 2×10^{24} kg this concentration would cause a heat production of 0.6–0.8 TW according to Eq. (2.4).

A slightly different approach has been chosen by Lee and Jeanloz [60]. They created pressures up to 26 GPa and heated pure potassium and iron to temperatures greater than 2,200 °C. A maximum value of 7,000 ppm potassium in the core is found to be possible. This seems to confirm the theoretical prediction of [59] rather well. Furthermore, there is no need for

the presence of sulfur. However, a concentration of 7,000 ppm potassium would, of course, exceed the 40 TW constraint of heat production, but it shows that the uptake of potassium in the core is highly possible. One also has to remark that the value of 7,000 ppm has to be taken as an upper limit as one can not assume to encounter such pure iron and potassium at the time of core formation.

The possibility of uranium being part of the core is taken up in the hypothesis of the existence of a georeactor in the Earth's center as proposed by Herndon in 1993 [61]. The assumption is that a "drop" of uranium sinks to the core taking up a sphere of 5 km radius with a temperature of 7,000 °C. As the concentration of ^{235}U was higher 4.5 Gyr ago, initial criticality was reached. More ^{235}U was provided by the fast breeder reaction of neutron capture on ^{238}U, and the subsequent decay of ^{239}Pu to ^{235}U. This georeactor would be responsible for a heat production of 3–10 TW, corresponding to a neutrino flux of 0.1–0.3 $\times 10^6$ cm^{-2}sec^{-1} on the surface. An experimental hint for the existence of such a reactor might be provided by the ^{3}He/^{4}He ratio, which is significantly increased in basaltic materials compared to the atmosphere. As ^{4}He is on Earth dominantly produced in the α-decay chains of uranium and ^{3}He originates from the ^{3}H-decay (produced in ternary fission) the conclusion was reached that the basaltic material has undergone an enrichment due to the georeactor (see discussion in [62] based on [63, 64]).

In any case, the neutrino flux of a core reactor would be measurable via its characteristic reactor spectrum. However, even if the reactor had never reached criticality, the uranium would still add to the heat production of the Earth. Additionally, it shall be emphasized with the hypothesis of the core reactor that there are models, which introduce uranium and maybe even thorium to the core, meaning that uranium and/or thorium show a siderophile behavior at high temperatures and pressures similar to potassium[5].

2.2 Feasibility studies for LENA

As we have seen in Sec. 2.1, information on the Earth's interior and its heat budget is mainly obtained via surface measurements and model dependent conclusions. Therefore a measurement of geoneutrinos that are linked directly to the abundances of radioactive elements would provide a novel way of obtaining information. We introduce in the following the geophysical models we use and discuss the consequences and detection prospects of a georeactor. We investigate the possibility of an angle dependent measurement of the

[5] A recent experimental analysis seems to disagree with this hypothesis in case of uranium [65].

neutrino flux and if this can be used to also obtain a directional dependent measurement of geoneutrinos, which would allow a tomography of the Earth. We present an analytical treatment of the angle dependent geoneutrino measurement in a scintillator detector before we discuss the results of a Monte Carlo study for the LENA detector.

2.2.1 Directional information from neutron displacement

In a scintillator detector, geoneutrinos are measured by the inverse beta-decay reaction, Eq. (1.1), with an energy threshold of 1.8 MeV. The total cross section is [66]

$$\sigma = 9.52 \times 10^{-44}\ \mathrm{cm}^2\ \frac{E_+}{\mathrm{MeV}}\frac{p_+}{\mathrm{MeV}}\,, \tag{2.5}$$

where E_+ is the total energy of the positron and p_+ its momentum. The visible energy $E_{\mathrm{vis}} = E_+ + m_e$ always exceeds 1 MeV because the positron annihilates with an electron of the target. By measuring the visible energy one can determine the neutrino energy as $E_\nu \approx E_{\mathrm{vis}} + 0.8$ MeV because the kinetic energy of the neutron is typically around 10 keV for small neutrino energies of order MeV and thus negligible. After thermalization the neutron is captured by a nucleus, thus tagging the inverse beta decay reaction.

Kinematics implies that the neutron is emitted roughly in the forward direction with respect to the incoming neutrino [67], this being the key ingredient for obtaining directional information. The maximum scattering angle can be easily derived as

$$\cos\theta_{\mathrm{max}} = \frac{\sqrt{2E_\nu\Delta - (\Delta^2 - m_e^2)}}{E_\nu}\,, \tag{2.6}$$

where $\Delta = m_n - m_p$ and m_n, m_p and m_e are the masses of the neutron, proton and positron, respectively. In this extreme case, the neutron and positron momenta are perpendicular to each other. For the maximum relevant geoneutrino energy of 3.2 MeV one obtains $\cos\theta_{\mathrm{max}} = 0.79$, which is equivalent to $\theta_{\mathrm{max}} = 37.8°$. However, most geoneutrinos have energies much nearer to the detection threshold and the maximum angles are closer to the forward direction. The average displacement ℓ between the neutron and positron events is then theoretically found to be about 1.7 cm [67].

The reactor experiment CHOOZ, using a Gd-loaded scintillator, has measured an average neutron displacement from the e^+ event of $\ell = 1.9 \pm 0.4$ cm [18]. However, once the neutron has been thermalized by collisions

with protons, it diffuses some distance before being captured so that the actual displacement varies by a large amount for individual events. In a PXE-based scintillator the average time interval between the neutrino reaction and the neutron capture on a proton is 180 μs, leading to an uncertainty σ of the displacement of about 4 cm for the x-, y- and z-direction [67]. With Gd loading σ is reduced to approximately 2.4 cm [67] because the neutron diffusion time is much shorter, on average about 30 μs [18].

2.2.2 PXE-based scintillator

One option for the proposed LENA detector is to use a scintillator based on PXE (phenyl-o-xylylethane, $C_{16}H_{18}$). As we have discussed in Sec. 1.2.1 PXE has a high light yield, it is non hazardous, has a relatively high flashpoint of 145°C, and a density of 0.985 g/cm^3 [25].

In this chapter we consider a detector with a total volume of about 70×10^3 m^3. This could be realized with a cylindrical detector of 100 m length and 30 m diameter. An outer water Cherenkov detector with a width of 2 m acts as a muon veto. In order to shield against external gamma and neutron radiation a fiducial volume of about 42×10^3 m^3 with a total number of 2.5×10^{33} free protons as target can be realized using a scintillator mixture as mentioned above with 20% PXE and 80% dodecane. In Monte Carlo calculations the light yield of events in LENA has been determined [30]. For events in the central detector region the yield $N_{\rm pe}$, measured in photo-electrons (pe) per MeV energy deposition, can be expressed as $N_{\rm pe} \approx 400$ pe/MeV $\times\, c$, where c is the optical coverage, which depends on the number and aperture of the photomultiplier tubes (PMTs). A maximal coverage $c_{\rm max} \approx 0.75$ [27] cannot be exceeded so that we assume the maximal light yield to be around 300 pe/MeV. For instance, the use of 12,000 PMTs with a diameter in aperture of 50 cm would result in an optical coverage of about 30% and a light yield of $N_{\rm pe} \simeq 120$ pe/MeV. This yield can be obtained either by using PMTs like in the Super-Kamiokande experiment or by smaller PMTs equipped with light concentrators as they were developed for the Counting Test Facility (CTF) at the Gran Sasso underground laboratory [68] and are now used in the Borexino experiment [15]. For events off the axis of the cylindrical LENA detector the light yield would be enhanced. Hence, low-energy spectroscopy even in the sub-MeV region should be possible in LENA.

For a detection of the positron-neutron displacement the ability of the detector to locate the absorption position of both particles is crucial. The experimental reconstruction of the location of both events is possible by analyzing the arrival times and the number of photons in each individual PMT. The position uncertainty depends on the total yield of registered photo-electrons.

In the CTF, the measured position uncertainty was around 10 cm in each direction for events with 300 photo-electrons and it was shown that the uncertainty scales with the inverse square-root of that number [69]. Therefore, we will use a Gaussian distribution for the uncertainty of the positron event reconstruction with equal width in each direction of

$$\sigma_{e^+} = 10 \text{ cm } \left(\frac{300 \text{ pe/MeV}}{N_{\text{pe}}} \frac{1 \text{ MeV}}{E_{\text{vis}}} \right)^{1/2} \tag{2.7}$$

where N_{pe} is the light yield and E_{vis} the visible energy released by the positron.

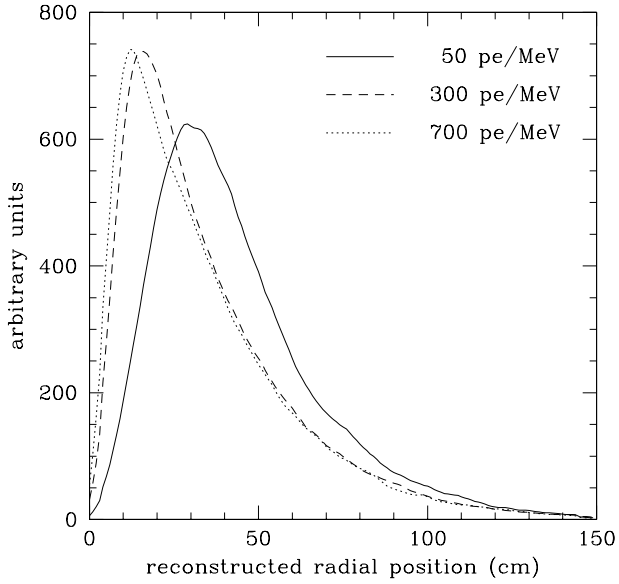

Figure 2.2: Monte Carlo simulation of the radial distribution of a 2.2 MeV γ-quantum in an unloaded PXE scintillator. The curves are for light yields of $N_{\text{pe}} = 50$, 300 and 700 pe/MeV as indicated.

In PXE-based scintillators the neutron is captured by a proton, which subsequently releases a 2.2 MeV gamma. This photon has a mean free path of 22.4 cm before its first Compton scattering so that the event reconstruction is much more uncertain than for the positron event. We have simulated this case by taking into account multiple Compton scatterings of the 2.2 MeV gamma. The position of each gamma emission, representing the position of the neutron capture, is reconstructed by composing the energy-weighted sum of each Compton scattering event, taking into account the instrumental res-

olution. The distribution of the reconstructed position in each direction follows roughly a Lorentzian form. In Fig. 2.2 we show the radial distribution of the reconstructed positions of these events for light yields of $N_{\mathrm{pe}} = 50$, 300 and 700 pe/MeV. Increasing the light yield does not significantly narrow the distribution because its width is dominated by the large Compton mean free path of the 2.2 MeV photon. With reduced light yield the position of the maximum as well as the mean value of the distribution shifts towards larger values. This is caused by the increased uncertainty of the instrumental resolution.

2.2.3 Gadolinium-loaded scintillator

In Sec. 1.2.1 we have discussed the properties of scintillators with the admixture of gadolinium. The advantage of a Gd additive is that the neutron of Eq. (1.1) is captured on a Gd nucleus with a total energy release of about 8 MeV, which are distributed on an average number of 3 photons.

For Gd-loaded scintillators we use the measurements performed in the CHOOZ experiment and assume a Gd concentration of about 0.1% by mass. The neutron response of the detector was measured with a ^{252}Cf-source and the position uncertainty of a neutron capture event was 19 cm at $1\,\sigma$ in each direction [70]. The distribution was Gaussian and the light yield was measured to be $N_{\mathrm{pe}} = (125 \pm 5)$ pe/MeV. The reconstruction was performed using only the information about the amplitude distribution of the PMTs. Based on these numbers, we assume the position resolution of the neutron event for the LENA detector to be Gaussian-shaped with a width in each direction of

$$\sigma_n = 19 \text{ cm } \left(\frac{125 \text{ pe/MeV}}{N_{\mathrm{pe}}} \right)^{1/2} . \tag{2.8}$$

In CHOOZ no information on the arrival time was used for the position reconstruction. However, the CTF measurements demonstrated that this yields the most valuable information, provided the time response of the PMTs is fast enough, i.e. a time jitter not much larger than 1 ns. Therefore, in a Gd-loaded scintillator one probably could achieve a much better neutron-event reconstruction so that our estimates are conservative.

2.2.4 Backgrounds

The KamLAND experiment has reported 152 events in the energy region relevant for geoneutrinos within a measuring time of 749 days and 3.5×10^{31} target protons [17]. Of these events 127 ± 13 are due to background [17]. The

most relevant background for the KamLAND site are reactor anti-neutrinos (80.4 ± 7.2 events). For the LENA detector positioned in the underground laboratory CUPP (Centre for Underground Physics in Pyhäsalmi) in Finland this background would be reduced by a factor $\simeq 12$, as the site is far away from reactors [26]. The Pyhäsalmi mine (longitude: 26° 2.709' E, latitude: 63° 39.579' N) has an overburden of 1,450 m of rock (4,060 m.w.e.). Hence we expect for LENA at CUPP a reactor background rate of about 240 events per year in the relevant energy window from 1.8 MeV to 3.2 MeV. This background can be subtracted statistically using the information on the entire reactor neutrino spectrum up to $\simeq 8$ MeV.

Another important background for KamLAND is induced by radio impurities. A large concentration of the long-lived isotope ^{210}Pb is present in the KamLAND scintillator. In the decay chain of ^{210}Pb the α-emitting isotope ^{210}Po is present. Thus the reaction $^{13}\mathrm{C}(\alpha, n)^{16}\mathrm{O}$ can occur, mimicking the signature of geoneutrinos due to neutron scattering on protons and the subsequent neutron capture. The number of these background events in KamLAND is estimated to be 42 ± 11 [17]. However, with an enhanced radiopurity of the scintillator, the background can be significantly reduced. Taking the radiopurity levels of the CTF detector, where a ^{210}Po activity of $35 \pm 12/\mathrm{m}^3\mathrm{d}$ in PXE has been observed [25], this background would be reduced by a factor of about 150 compared to KamLAND and would amount to less than 10 events per year in the LENA detector.

An additional background that imitates the geoneutrino signal is due to ^{9}Li, which is produced by cosmic muons in spallation reactions on ^{12}C and decays in a β-neutron cascade. Only a small part of the ^{9}Li decays falls into the energy window, which is relevant for geoneutrinos. KamLAND estimates this background to be 0.30 ± 0.05 [17]. At CUPP the muon reaction rate would be reduced by a factor $\simeq 10$ due to better shielding and this background rate should be at the negligible level of $\simeq 1$ event per year in LENA.

2.3 Models of the Earth

As we have already discussed in Sec. 2.1 there are several theories and models about the structure of the Earth's interior. For constructing our geophysical models we use the Preliminary Reference Earth Model [43] and the Bulk Silicate Earth Model [45] with the most dominant and abundant radioactive isotopes ^{238}U and ^{232}Th.

The flux of geoneutrinos is directly linked to the rate of radioactive decays and to the generated heat. Therefore, it is of great interest to measure the geoneutrino flux and thus deduce the main contributor to the heat produc-

tion. The elemental abundance ratios in the Bulk Silicate Earth Model are Th/U ≈ 4 and K/U $\approx 1.14 \times 10^4$ [45]. We emphasize again that, according to this model, radioactive isotopes are only in the crust and mantle because they are lithophile, whereas the core is void of any significant amount of uranium, thorium or potassium. Different estimates for their abundances in the crust and mantle differ by factors of 2–3 [51]. Based on these abundance measurements, a group of physicists has, in cooperation with geologists, constructed a reference model for the abundance values of uranium, thorium and potassium. They used the values referenced in the GERM reservoir data base [51] and derived a mean value for each element [71]. We will implement these abundances into our Reference Model of the geoneutrino angular distribution[6]. Our Reference Model is in accordance with the Bulk Silicate Earth constraint of a heat production of 20 TW due to radioactive decays in the crust and mantle.

The geoneutrino flux depends sensitively on location. The oceanic crust has a thickness of only 6–10 km and is found to be depleted in radioactive elements, whereas the flux on the continents is dominated by the crust [45, 51, 71]. Thus an experiment situated in the Pacific Ocean, e.g. on Hawaii, would have better access to the oceanic crust and the mantle. For an experiment located on a continent we have assumed a thickness of 50 km for the crust, implying a total neutrino flux in our Reference Model of 4.2×10^6 cm^{-2} sec^{-1} from uranium and 4.1×10^6 cm^{-2} sec^{-1} from thorium decays. For an oceanic site we have chosen the crust to be rather thick (50 km), but not included any sediments, which would add additional radioactivity. Our assumption of a uniform oceanic crust with a thickness of 50 km has been made for computational reasons. Still, this model for the Hawaiian detector site is valid as our event rate is slightly lower than the rate found in [71]. Moreover, if one wanted to determine the mantle contribution to the $\bar{\nu}_e$-flux, the oceanic crust would be a background to the measurement so that the assumption of a thick oceanic crust is conservative. In addition, as will become obvious in Sec. 2.5, changes in the crustal thickness of an oceanic site by even one order of magnitude cannot be resolved by the detector. The neutrino fluxes in this case are 1.25×10^6 cm^{-2} sec^{-1} from uranium and 0.88×10^6 cm $^{-2}$ sec^{-1} from thorium decays.

Besides our reference model we consider three "exotic" cases A, B and C, each of them either with a continental or an oceanic crust.

(A) Fully radiogenic model with additional uranium and thorium in the core, accounting for 20 TW additional heat production. (Integrated

[6]For a discussion of the angular spectra of this model and its uncertainties see Ref. [16].

neutrino flux increase of about 32% relative to the reference model in a continental location, and 116% in an oceanic location.)

(B) Same as A, but with 10 TW in the core. (Flux increase of 16% and 58%, respectively.)

(C) 20 TW in the Lower Mantle. (Flux increase of 41% and 148%, respectively.)

The zenith-angle distributions of the neutrino fluxes from these models have been determined along the lines of Ref. [16] and are shown in Fig. 2.3. We can see from the figure that the core contributes below a zenith-angle of 30°. The spike above 80° in the upper panel of Fig. 2.3 shows the dominant flux from the continental crust, whereas in the lower panel the spike is absent because of the low radioisotope content of the oceanic crust. Between 30° and 60° one can recognize the influence of the lower mantle.

To obtain the event rate in a scintillator detector, neutrino flavor oscillations have to be accounted for. Matter effects for oscillations are not important because of the small geoneutrino energies. Moreover, for geoneutrino energies of 1.8–3.2 MeV and $\Delta m^2_{12} = 7.9 \times 10^{-5}$ eV^2 the vacuum oscillation length is 57–101 km. The inclusion of distance to the geoneutrino source and of energy dependent survival probabilities would only contribute a negligible correction to a global reduction factor [72]. Therefore we include only a global $\bar{\nu}_e$ survival-probability factor of 0.57 (see Eq. (B.7) of appendix B) according to the KamLAND results [5]. Note that we have assumed $\theta_{13} \approx 0$, as this contribution is negligible for oscillations on this length scale. The annual event rates corresponding to our models, including the reduction factor, are shown in Tab. 2.3 for a 50 kton detector with a fiducial volume corresponding to 2.5×10^{33} protons. To calculate the rates we have used the cross section, Eq. (2.5).

Up to now we have assumed in all our models that the exotic heat source in the Earth's core is caused by uranium and thorium decays, i.e. the neutrino

Table 2.3: Annual event rates for 2.5×10^{33} target protons. Flavor oscillations have been included with a global reduction factor of 0.57.

Model	Continental Crust	Oceanic Crust
Reference Model	1.02×10^3	0.29×10^3
(A) 20 TW core	1.35×10^3	0.62×10^3
(B) 10 TW core	1.19×10^3	0.45×10^3
(C) 20 TW Lower Mantle	1.44×10^3	0.71×10^3

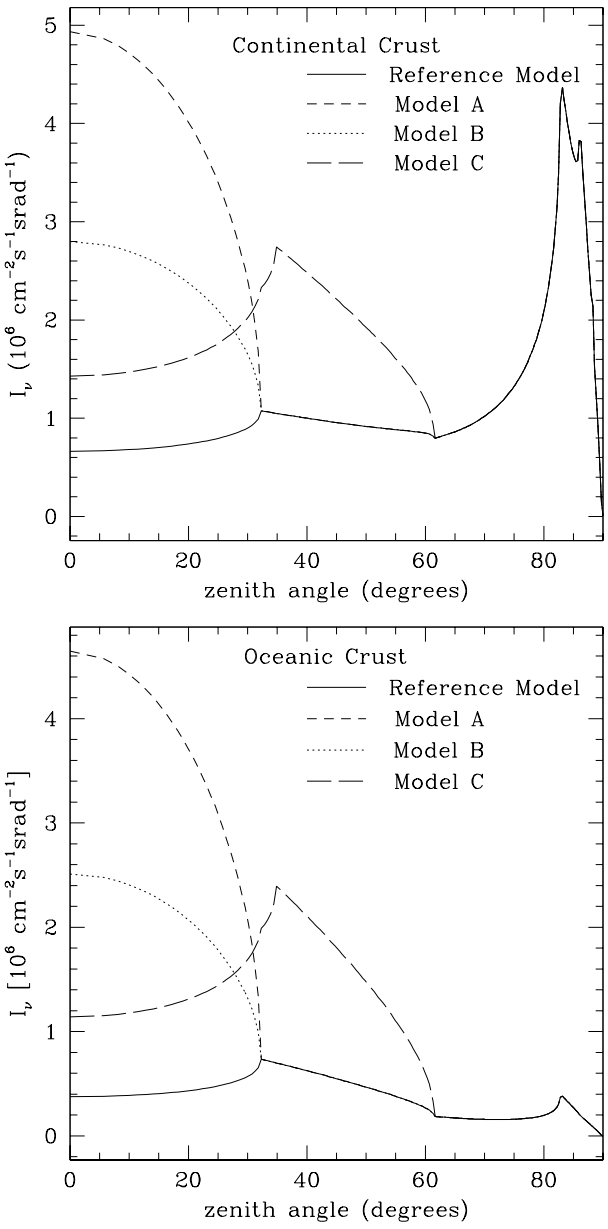

Figure 2.3: Zenith-angle distribution of the geoneutrino flux where $\theta = 0$ corresponds to the vertical direction. Shown is the total flux without flavor oscillations. Core contribution is below 30°, crustal neutrinos are seen above 80°. *Upper panel:* Continental crust. *Lower panel:* Oceanic crust.

spectrum from this additional source was taken to be identical with the geoneutrino spectrum from the crust and mantle. However, the possibility of a natural reactor in the Earth's core ("georeactor") has been discussed in the literature [61, 64]. In this case the neutrino flux could be similar to that from an ordinary power reactor with energies reaching up to about 8 MeV. With this assumption the total 4π-georeactor neutrino flux can be estimated to be $\Phi_\nu \simeq 1.9 \times 10^{23}$ s^{-1} for a thermal power of 1 TW. Taking into account neutrino oscillations, the distance to the center of the Earth, and the detection cross section we calculate an event rate of about 210 yr^{-1} TW^{-1} in LENA. At Pyhäsalmi one would observe about 2,200 events per year due to neutrinos from nuclear power plants. Assuming a systematic uncertainty for the neutrino flux from the power plants of 6.5%, as suggested in [17, 5], we conclude that LENA will be able to identify a georeactor of ≥ 2 TW after one year of measurement with a $3\,\sigma$ significance. The influence of the uncertainty of the mixing angle θ_{12} is negligible, because the flux of both the georeactor and the power plants depends on θ_{12} in the same way.

2.4 Analytic treatment

Before we come to a numerical analysis and the results of a Monte Carlo simulation, we present some analytical estimates of the angular resolution power, which is valid in the Gaussian limit.

The angular spectra are obtained with the formalism developed by Fields and Hochmuth [16] and are shown in Fig. 2.3 for the reference model and model A, B and C. Each model is characterized by the angle dependent intensity $I(\eta, \phi)$, where we have defined η to be the cosine of the zenith angle in Fig. 2.3. Thus $\eta = 0$ corresponds to the horizontal direction. In the axially symmetric case I is independent of the azimuth angle ϕ, which we will assume in the following. We introduce the quantity $\hat{I}(\eta)$, which is the angle dependent intensity normalized to 1. This quantity will be needed in order to obtain the geoneutrino distribution function.

To conduct an analysis of the signatures of different geophysical models in the detector we need to consider the distribution of the reconstructed neutron displacement, expressed in the relative coordinates x, y and z, where the z-axis is chosen as the vertical direction. As we assume that the $\bar{\nu}_e$-flux is axially symmetric, we do not have to consider the details of the distribution in the x- and y-direction, leading to an arbitrarily orientated neutron displacement in the x-y-plane of $\ell\sqrt{1-\eta^2}$, where ℓ is the neutron displacement introduced in Sec. 2.2.1. The neutron displacement in the z-direction is $\ell\eta$. We assume that the position resolution of both positron and neutron, σ_{e^+} and

σ_n, follows a Gaussian according to Eqs. (2.7) and (2.8). The uncertainty σ_ℓ of the displacement ℓ due to neutron scattering and diffusion in a Gd-loaded scintillator is ~ 2.4 cm for the x-, y- and z-direction [67]. This compares to $\sigma_\ell > 4$ cm in an unloaded scintillator, as the neutron capture on protons is slow compared to Gd. From these uncertainties we obtain a joint Gaussian curve with variance

$$L^2 = \sqrt{\sigma_\ell^2 + \sigma_{e^+}^2 + \sigma_n^2}\,. \tag{2.9}$$

Thus the distribution function in Cartesian coordinates is

$$f(x,y,z) = \int_0^1 \mathrm{d}\eta \frac{\hat{I}(\eta)}{(2\pi L^2)^{3/2}} \exp\left(\frac{-(\sqrt{x^2+y^2} - \ell\sqrt{1-\eta^2})^2 - (z-\ell\eta)^2}{2L^2}\right). \tag{2.10}$$

As introduced above $\hat{I}(\eta)$ corresponds to the normalized angle dependent intensity distribution characterizing a geophysical model. After a transformation to spherical coordinates Eq. (2.10) reads

$$\begin{aligned} f(\rho,\cos\theta) \;=\; & \int_0^1 \mathrm{d}\eta \left[\frac{\rho^2}{L(2\pi)^{3/2}}\,\hat{I}(\eta)\times\right. \\ & \left.\exp\left(-\frac{\rho^2+\lambda^2-2\lambda\rho\sqrt{1-\eta^2}\sqrt{1-\cos^2\theta}-2\lambda\rho\eta\cos\theta}{2}\right)\right], \end{aligned} \tag{2.11}$$

where we have introduced the dimensionless quantities $\rho = r/L$ and $\lambda = \ell/L$. We have here $\ell \approx 1.9$ cm and $L > 15$ cm, considering the light yields of less than 300 pe/MeV. Thus we can assume $\lambda \ll 1$ in the case considered here and expand Eq. (2.11) for small λ. Moreover, to investigate the behavior of Eq. (2.11) an expansion in Legendre Polynomials is useful. Because of the smallness of λ we find that only the dipole moment gives useful information. The quadrupole moment is very small compared to its variance, which we will also stress in the next section, where this will be again verified with a Monte Carlo simulation. Therefore, we write the reconstructed zenith-angle distribution in the form

$$\frac{\mathrm{d}\dot{N}}{\mathrm{d}\cos\theta} = \dot{N}\,\left(\frac{1}{2} + p\,\cos\theta\right) \equiv \dot{N}\,g(\cos\theta), \tag{2.12}$$

where the event rate $\dot{N}$ and the slope p are the two numbers that characterize a given configuration of geophysical model and type of detector. Thus with the distribution function (2.11) the dipole moment in this normalization is

$$p = \frac{3}{2}\int_0^\infty \mathrm{d}\rho \int_0^{2\pi} \mathrm{d}\phi \int_{-1}^1 \mathrm{d}\cos\theta f(\rho,\cos\theta)\cos\theta. \tag{2.13}$$

For small λ, Eq. (2.13) can be expanded to

$$\begin{aligned} p &= \frac{3}{2}\int_0^1 \mathrm{d}\eta \int_0^\infty \mathrm{d}\rho \int_0^{2\pi} \mathrm{d}\phi \int_{-1}^1 \mathrm{d}\cos\theta \rho^2 \left(\tfrac{1}{\sqrt{2\pi}}\right)^3 \cos\theta\, e^{-1/2\rho^2} \\ &\quad \times \left[1 + \rho\lambda(\sqrt{1-\eta^2}\sqrt{1-\cos^2\theta} + \eta\cos\theta)\right] \hat{I}(\eta) \\ &= \sqrt{\tfrac{2}{\pi}}\,\lambda\,\bar{\eta}, \end{aligned} \tag{2.14}$$

where we have introduced the weighted mean

$$\bar{\eta} = \int_0^1 \mathrm{d}\eta \hat{I}(\eta)\eta. \tag{2.15}$$

The expansion of Eq. (2.13) introduces an error of at most 1% compared to the full integration. In this limit the dipole moment is linearly dependent on λ and $\bar{\eta}$, meaning that one is only able to distinguish between models yielding different values of $\bar{\eta}$. The values of $\bar{\eta}$ for different geophysical models can be obtained with the formalism in [16]. In Tab. 2.4 the $\bar{\eta}$ values and the corresponding mean zenith angles $\alpha = \arccos\bar{\eta}$ are displayed for the Reference Model and the models with a core contribution of varying strength. In order to obtain the precision with which $\bar{\eta}$ can be determined the mean and variance of $g(\cos\theta)$ of Eq. (2.12) have to be calculated. We find a mean value of $\langle\cos\theta\rangle = \frac{2}{3}\sqrt{\frac{2}{\pi}}\,\lambda\,\bar{\eta}$ and a variance

$$\sigma^2_{\cos\theta} = \frac{1}{3} - \frac{8}{9\pi}\,\lambda^2\,\bar{\eta}^2. \tag{2.16}$$

For the present case, where $\lambda \ll 1$, this reduces to

$$\sigma_{\cos\theta} = \sqrt{\frac{1}{3}}. \tag{2.17}$$

Table 2.4: Coefficients $\bar{\eta}$ and corresponding zenith angle $\alpha = \arccos\bar{\eta}$ in degrees characterizing different geophysical models.

	Continental Crust		Oceanic Crust	
Model	$\bar{\eta}$	α	$\bar{\eta}$	α
Reference Model	0.3804	67.6°	0.6161	52.0°
2.5 TW core	0.4028	66.3°	0.6583	48.8°
5 TW core	0.4235	64.9°	0.6907	46.3°
10 TW core (Model B)	0.4604	62.6°	0.7371	42.5°
15 TW core	0.4924	60.5°	0.7689	39.7°
20 TW core (Model A)	0.5204	58.6°	0.7921	37.6°

Hence the standard deviation of $\bar{\eta}$ is

$$\sigma_{\bar{\eta}} = \frac{3}{2\lambda}\sqrt{\frac{\pi}{2}}\,\sigma_{\cos\theta} = \sqrt{\frac{3\pi}{8}}\,\frac{1}{\lambda}. \tag{2.18}$$

Therefore, with N events $\bar{\eta}$ of a specific geophysical model can be determined with a 1σ uncertainty of $\sigma_{\bar{\eta}}/\sqrt{N}$.

In order to distinguish between two different geophysical models i and j corresponding to $\bar{\eta}_i$ and $\bar{\eta}_j$ at the $n\sigma$-significance level, an event number

$$N_{s\sigma} = 2\,\frac{(n\sigma_{\bar{\eta}})^2}{(\bar{\eta}_i - \bar{\eta}_j)^2} = \frac{3\pi}{4\lambda^2}\,\frac{n^2}{(\bar{\eta}_i - \bar{\eta}_j)^2} \tag{2.19}$$

is required. Assuming for example $\lambda = 0.1$, which corresponds to $N_{\mathrm{pe}} \sim 120$ pe/MeV, an event number of 1.2×10^4 is required at the $1\,\sigma$ significance level to distinguish the reference model from the model with a 20 TW core contribution. This corresponds to an exposure of about 500 kton-years.

2.5 Monte Carlo study

After the analytical study of the previous section, which is only applicable for Gaussian distributions, we come now to a more general treatment of the situation by means of a numerical analysis, which is applicable to diverse distribution functions. To study the power of directional discrimination of a large liquid-scintillator detector we have performed a Monte Carlo simulation of a large number of geoneutrino events and the corresponding directional reconstruction. First, we give a short description of the Monte Carlo program: the code was written in the Fortran programming language. The neutrino spectrum has been generated according to the zenith-angle distribution depicted in Fig. 2.3 with direction angle θ. We have assumed that the detector response is independent of the event location, i.e. only the spatial separation between the event $\bar{\nu}_e + p \rightarrow n + e^+$ and the location of neutron capture is relevant. However, we consider a position resolution of point like events located at the central axis of the detector, which is a conservative assumption, as the light yield and hence also the position resolution increases for off-axis events. Thus each neutrino is assumed to react in the center of the detector at a position of (0,0,0) in spatial coordinates, which we take as the location of the prompt positron event. Then a random vector $\vec{p}_{e^+}$ is created according to a Gaussian distribution with a width in each direction given by Eq. (2.7). The actual spread of relevant visible energies is small so that we have always used $E_{\mathrm{vis}} = 1.4$ MeV as a typical value. The neutron event is, on average,

displaced from the prompt positron event by $(\ell\cos\theta, 0, \ell\sin\theta)$, as we assume azimuthal symmetry. As the displacement ℓ has a Gaussian uncertainty σ_ℓ in each direction due to neutron diffusion, we create a random vector $\vec{p}_n$ with this width. The resulting vector is again randomized with the uncertainty of the position reconstruction of the neutron event, which has the shape according to Fig. 2.2 for a PXE-based scintillator and a Gaussian-shape according to Eq. (2.8) for Gd-loaded scintillators. From this we can construct a vector $\vec{p}_{\bar{\nu}_e}$ for the reconstructed neutrino direction as

$$\vec{p}_{\bar{\nu}_e} = (\ell\cos\theta, 0, \ell\sin\theta) + \vec{p}_n - \vec{p}_{e^+}\,. \tag{2.20}$$

We have assumed that, on average, the neutron capture point is displaced by $\ell = 1.9$ cm in the forward direction relative to the e^+ event in agreement with the CHOOZ measurement [70]. The uncertainty of the displacement is taken to be $\sigma_\ell = 4.0$ cm for an unloaded PXE-based scintillator and $\sigma_\ell = 2.4$ cm for a Gd-loaded scintillator [67] as described in Sec. 2.2. The main uncertainty originates from the reconstruction of both events, i.e. the resolution of the detector. For an unloaded scintillator, the uncertainty of the reconstruction of the neutron event is larger than for Gd-loaded scintillators; due to the Gaussian shape of σ_n in Gd-loaded scintillators, the resolution could in principle become infinitely good. For PXE-based scintillators, however, we are limited by the intrinsic properties of the Compton scattering process in scintillators as discussed in Sec. 2.2.

For the sake of illustration we discuss the reconstructed zenith-angle distributions for the two extreme cases where all neutrinos come from the horizontal direction ($\cos\theta = 0$) or all of them come vertically from below, i.e with $\cos\theta = 1$. Thereby the angle between the reconstructed direction vector $\vec{p}_{\bar{\nu}_e}$ (normalized to 1) and the z-axis has been determined. Figure 2.4 displays the reconstructed zenith-angle distribution of both cases, each generated with 25,000 neutrino events and using a Gd-loaded detector with a light yield $N_{\rm pe} = 300$ pe/MeV. For $\cos\theta = 0$ we have a flat distribution, whereas for $\cos\theta = 1$ we have a definite slope, with about 30% more reconstructed events at $\cos\theta = 1$ than at $\cos\theta = 0$. Clearly, the method is suitable for locating neutrino sources. However, given the presently limited angular reconstruction capability of scintillator detectors, the only angular-distribution information that can be extracted is the slope of the distributions shown in Fig. 2.4. As an event-by-event reconstruction is not possible, we have analyzed the reconstructed $\cos\theta$-distribution by an expansion in Legendre polynomials up to the quadrupole moment. It is possible to extract the total event rate and the dipole contribution of the angular distribution, whereas a determination of higher multipoles is unrealistic. Therefore, coming to the same conclusion as in Sec. 2.4 we write the reconstructed zenith-angle distribution as in

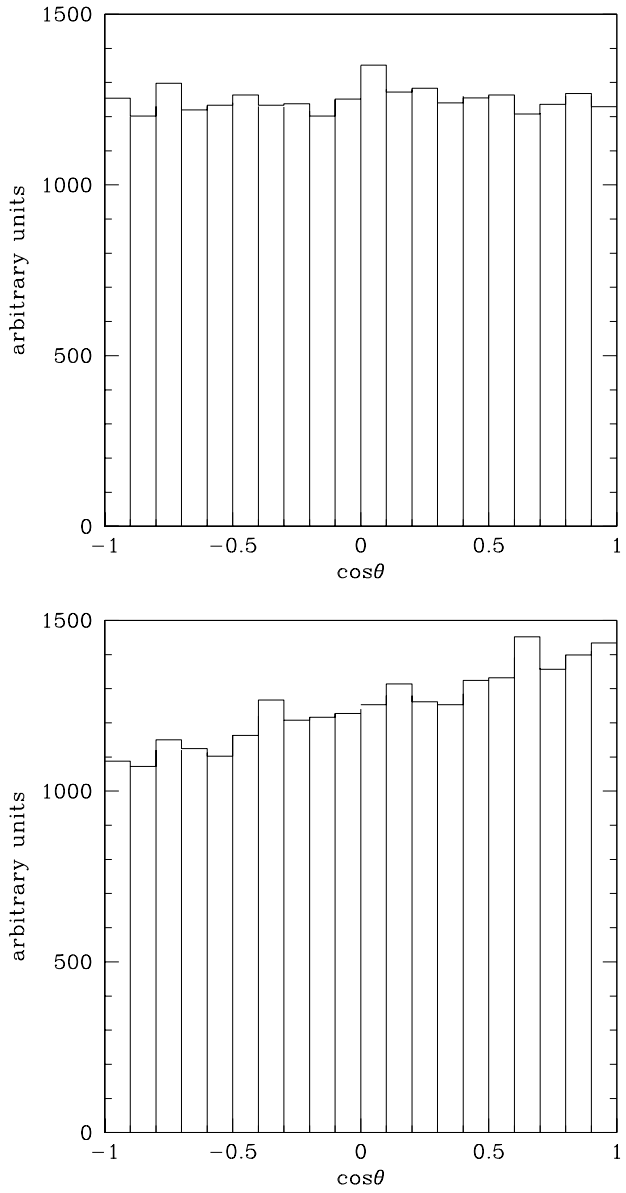

Figure 2.4: Monte Carlo example of reconstructed zenith-angle distribution of 25,000 events in a Gd-loaded detector. *Upper panel:* Neutrinos injected from the horizontal direction ($\cos\theta = 0$). *Lower panel:* Neutrinos injected from the vertical direction ($\cos\theta = 1$).

Eq. (2.12) with the numbers $\dot{N}$ and p characterizing a given configuration of geophysical model and detector type.

Table 2.5: Coefficient p for the reconstructed zenith-angle distribution for different Earth models and different detector types, always assuming a light yield of 300 pe/MeV.

Model	Coefficient p for scintillator detectors	
	Unloaded PXE	Gd-loaded
Continenal Crust		
Reference Model	0.0283	0.0377
(A) 20 TW core	0.0377	0.0521
(B) 10 TW core	0.0333	0.0459
(C) 20 TW Lower Mantle	0.0351	0.0485
Oceanic Crust		
Reference Model	0.0468	0.0646
(A) 20 TW core	0.0597	0.0824
(B) 10 TW core	0.0560	0.0772

The event rates for our fiducial detector size with 2.5×10^{33} target protons and different geophysical models have already been reported in Tab. 2.3. What remains to be determined by means of a Monte Carlo simulation are the corresponding coefficients p and their uncertainty. As mentioned above, we determine the coefficients numerically with a multipole expansion in Legendre polynomials. In Tab. 2.5 we show the results for p for different cases, always assuming a light yield of 300 pe/MeV. The uncertainty s_p of the measured p value scales with the inverse square root of the number of events N so that $s_p = \sigma_p \sqrt{N}$ is a quantity independent of N. The value of s_p can be derived analytically for $p = 0$, when combining Eq. (2.14) and Eq. (2.18) yielding

$$s_p = \frac{\sqrt{3}}{2} = 0.866, \tag{2.21}$$

which is valid for all $p \ll 1$. We have checked with our Monte Carlo that Eq. (2.21) indeed applies to all p values of interest to us.

In order to distinguish a geophysical model i from model j at the $1\,\sigma$ level, the required number of events is

$$N_{1\sigma} = \frac{2 s_p^2}{(p_i - p_j)^2} = \frac{3}{2} \frac{1}{(p_i - p_j)^2}. \tag{2.22}$$

A detection at the $n\sigma$ level requires n^2 times more events. This result is complementary to the one obtained in Eq. (2.19) for the Gaussian case. We

find that for a Gd-loaded scintillator, i.e. in the Gaussian case, the Monte Carlo results are in good agreement to the ones obtained in Sec. 2.4. For example, we find analytically $p = 0.0519$ for $\lambda = 0.126$, which corresponds to $\ell = 1.9$ cm and 300 pe/MeV. Correspondingly we find $p = 0.0485$ with our Monte Carlo (see Tab. 2.5). The difference is due to the break-down of our assumed analytical limit of $\lambda \ll 1$.

In the same way as for Tab. 2.5 we have calculated the slope p for different light yields of the scintillator and have determined the number of events it takes to distinguish each of the exotic models from the reference case. In Fig. 2.5 we display $N_{1\sigma}$ for these cases and the continental-crust situation as a function of the light yield N_{pe}, both for an unloaded PXE-type detector and a Gd-loaded one. In Fig. 2.6 we show the same for the oceanic crust. In the oceanic location we do not show model C because it corresponds to an increased flux from the mantle, i.e. it is essentially identical with the reference model except for the total flux and thus cannot be distinguished on the basis of the zenith-angle distribution. The actually calculated data points are shown explicitly, whereas the dashed lines are extrapolated. As expected, in the Gd-loaded case we see from Fig. 2.5 and Fig. 2.6 that the number of events continually decreases with increasing light yield, whereas for the unloaded scintillator the slope is much flatter for high light yields due to the non-Gaussian shape of the uncertainty of the neutron reconstruction. For light yields less than 100 pe/MeV the reconstruction capability of unloaded scintillators is even better than for Gd-loaded ones. As displayed in Fig. 2.6, in case of an experiment situated on the oceanic crust one needs about 40% less events than on the continents to distinguish the models from the reference model. However, the oceanic event rates are also reduced by more than 50%, as shown in Tab. 2.3. Therefore, locating the experiment on the oceanic crust does not bring an advantage.

Of course, the time required to achieve the discriminating power depends on the detector size. For our fiducial volume with 2.5×10^{33} target protons as in LENA one needs to scale with the event rates shown in Tab. 2.3. In a continental-crust location, all models produce an event rate of roughly 1,000 events per year, in full agreement with the KamLAND measurement [17]. For example, according to latest results one could expect light yields for the LENA detector (unloaded) of 250 pe/MeV [73]. So one could expect to distinguish model A from the reference model at $1\,\sigma$ after about 10 years. Assuming the same light yield for a Gd-loaded scintillator one would need roughly 5 years. Realistically, the LENA detector should have a lifetime of about 30 years. Thus for a meaningful distinction of even our most-optimistic model A from the reference case an unloaded 50 kton LENA detector is too small, as for a measurement at the $3\,\sigma$ level an exposure of 4,500 kton-years

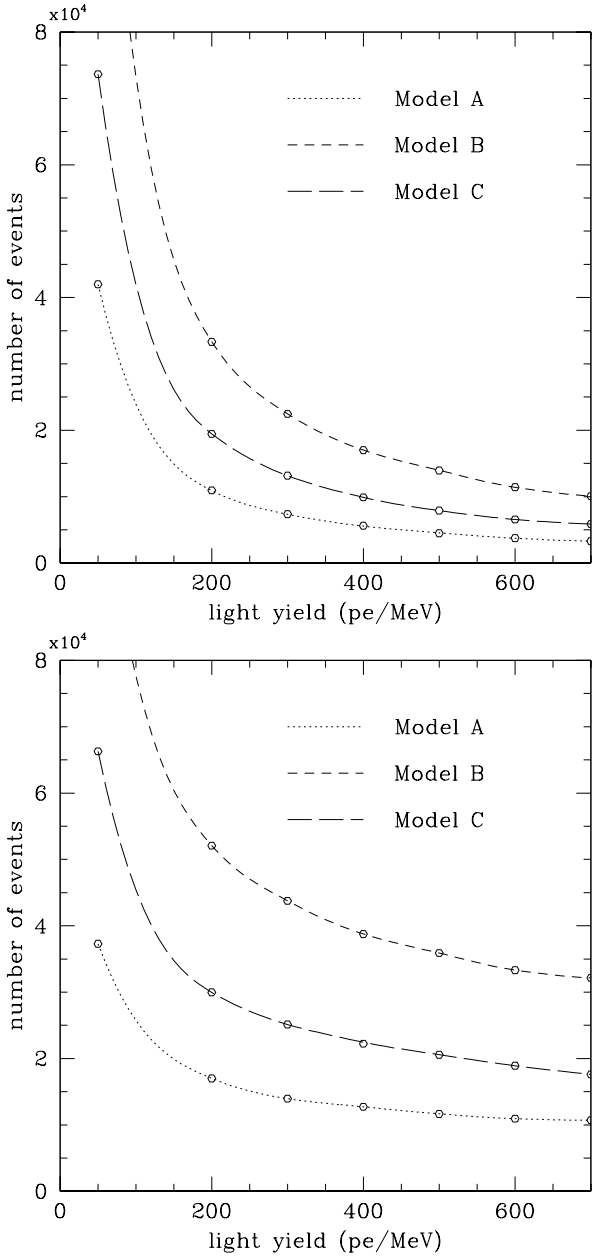

Figure 2.5: Number of events needed to distinguish between models A, B or C and the continental-crust reference model at 1σ significance. The points correspond to the values calculated with the Monte Carlo. *Upper panel:* Gd-loaded scintillator. *Lower panel:* Unloaded PXE-type scintillator.

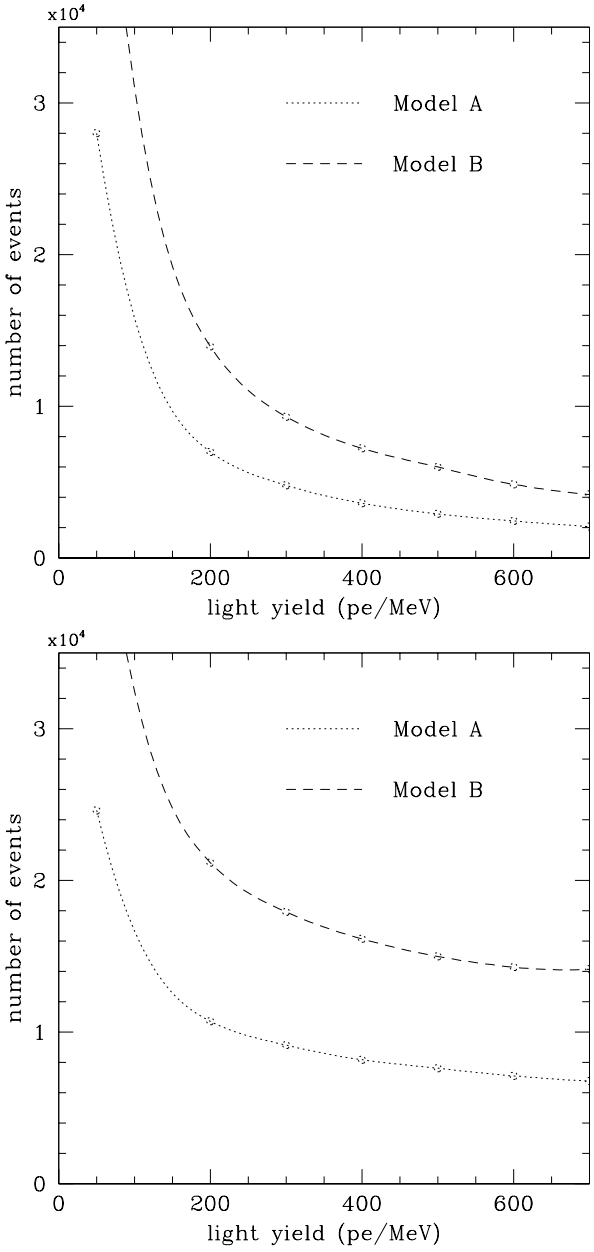

Figure 2.6: Same as Fig. 2.5 for oceanic crust. Model C was not included because the neutrino flux has almost the same angular distribution as the reference model so that an unrealistic high event number is needed for a discrimination.

is required. Still, considering the ongoing plans of several groups, it does not seem unlikely that more than one LENA-type detector will be built.

2.6 Summary of chapter 2

In summary we can say that a future large-volume scintillator detector such as the proposed 50 kt LENA would provide a high-statistics measurement of the geoneutrino flux. The event rate would depend strongly on the detector location, notably on whether an oceanic site such as Hawaii is chosen where a reference event rate of about 300 per year (50 kt scintillator) is expected or a continental site such as the Pyhäsalmi mine in Finland where the reference rate would be about 1,000 per year. Therefore, the geoneutrino flux could be measured with high significance and would allow one to distinguish between different geophysical models.

The forward displacement of the neutron in the inverse beta decay detection reaction provides directional information on the geoneutrino flux. We have studied if this effect can be used to distinguish between different geophysical models, notably if one could diagnose a strong exotic energy source in the Earth's core under the assumption that its neutrino spectrum is identical with that emitted by the crust and mantle. While a deviation from an isotropic flux can be ascertained with high significance, we find that a 50 kt detector with an expected realistic light yield of 250 pe/MeV is too small to distinguish between different geophysical models on the basis of the directional information alone, as even for our most-optimistic assumption an exposure of 500 kton-years would be required for a $1\,\sigma$ detection with an unloaded scintillator. However, we have chosen conservative assumptions for our analysis. Thus we have assumed events to occur only in the center of the detector, and relied on the CHOOZ measurement for the precision of the neutron reconstruction, which could be improved when considering the arrival times in the PMTs.

As an important result we find that placing the experiment on the oceanic crust is not useful for discriminating between different models. Though the background from the continental crust is reduced and a measurement of the inner layers seems more promising, we find that a discrimination requires more time than on the continents due to the reduced event rates. However, detector backgrounds should be included in a realistic assessment.

In our study we have only used the neutrino flux from the Earth, ignoring the contribution from power reactors because it depends strongly on location. For example, in Pyhäsalmi the neutrino flux from power reactors adds roughly 25% to the counting rate in the energy window relevant for geoneu-

trinos. This contribution is not negligible, but it does not change our overall conclusions.

We have also estimated the sensitivity of a LENA type detector for determining a hypothetical georeactor in the Earth's core. As a possible location the CUPP underground laboratory in Pyhäsalmi (Finland) was chosen and the background due to nuclear power plants was calculated. At CUPP a 2 TW georeactor could be identified at a statistical level of $3\,\sigma$ after only one year of measurement.

Concludingly, large-volume scintillator detectors of the next generation will be extremely useful to study the interior of the Earth in the "light of neutrinos". However, the prime information will be the total geoneutrino flux and its spectrum. It would be extremely challenging to use the directional information alone to distinguish between different geophysical models.

Chapter 3

Directional Sensitivity in Double Chooz

As we have already discussed in chapter 2, the directional sensitivity of liquid scintillator detectors relies on the forward displacement of the final-state neutron in Eq. (1.1) relative to the location of the final-state positron annihilation. This effect was first observed in experiments at the Gösgen reactor complex [74]. By reconstructing the vertices of the positron and neutron captures, one obtains an image of the neutrino source.

The CHOOZ experiment demonstrated the feasibility of this approach in that 2,500 events were enough to locate the source within a $1\,\sigma$ half-cone aperture of 18° [18, 70]. In principle, this method also allows one to determine the location of a galactic supernova explosion [18, 70] and the distribution of anti-neutrinos emitted by the natural radioactive elements in the Earth as we discussed in chapter 2, although in practice these applications are severely limited by the relatively small number of events.

In the following we investigate the potential of future reactor experiments to exploit the same effect, but with much larger statistics and point-like sources. We discuss the implementation of this method to separate and locate two reactor cores just by looking at their neutrinos. Moreover, we determine to what precision the power output of each individual reactor can be monitored, if we assume the locations of the reactors to be known. To that end we first discuss a two-reactor setup analytically, before we generate Monte Carlo data, which we analyze with the maximum likelihood method. In particular, the upcoming Double Chooz experiment [6] will be a first important test of the principles of directional measurements[1].

[1]This chapter is based on K. Hochmuth, M. Lindner, G. Raffelt, Phys. Rev. D **76**, 073001 (2007)

3.1 Experimental Setup

Double Chooz will operate two nearly identical cylindrically-shaped detectors at distances of roughly 280 m and 1,050 m to the reactor cores, respectively. As we have discussed in Sec. 1.2.1, both Double Chooz detectors will consist of about 10 tons of Gadolinium-loaded scintillator, with a Gd concentration of 0.1%. The near detector will register 1.6×10^5 $\bar{\nu}_e$-events per year, vastly exceeding the exposure of the CHOOZ experiment that was located at the far site of Double Chooz and had only a short data-taking period of about 3 months [70]. Thus one year of Double Chooz data correspond to 64 times the CHOOZ exposure and hence to an 8-fold improved angular resolution, implying that the neutrino source can be located within a $1\,\sigma$ half-cone aperture of 2.3°.

The Chooz nuclear power plant consists of two reactors that are viewed by the near detector at an angular separation $\phi = 30°$. We note here that an early version of the Double Chooz proposal foresaw a much smaller distance of about 100 m for the near detector, implying almost an order of magnitude larger statistics and a much larger separation angle of about 60°.

The final-state neutron of the inverse beta reaction Eq. (1.1) is captured by a Gd nucleus with an efficiency of 90%, releasing 2–3 γ rays with a total energy of about 8 MeV. Taking into account scattering and thermalization of the neutron, an average displacement $\ell = 1.7$ cm with an rms uncertainty of approximately 2.4 cm for the x-, y- and z-directions was calculated [67]. Experimentally, the CHOOZ experiment found $\ell = 1.9 \pm 0.4$ cm [18]. To be specific we will use

$$\ell = 1.9 \text{ cm}\,, \tag{3.1}$$

representing an average over the incoming neutrino energies and the outgoing neutron directions. The large spatial distribution of the neutron capture points as well, as the even larger uncertainty of the neutron and positron event reconstruction (see Eq. (2.7), Eq. (2.8) and discussion in chapter 2), imply that indeed only the average of the neutron displacement matters here.

The experimental output used for the directional information is a set of reconstructed displacement vectors $\mathbf{r}_i$ between the positron-annihilation and neutron-capture events, where $i = 1, \ldots, N$. In the Double Chooz near detector we have in one year

$$N = 1.6 \times 10^5 \tag{3.2}$$

events, originating from both reactor cores together. Unless otherwise stated we will always use this event number in our numerical estimates. Our main simplifying assumption is that for a single neutrino source the distribution of

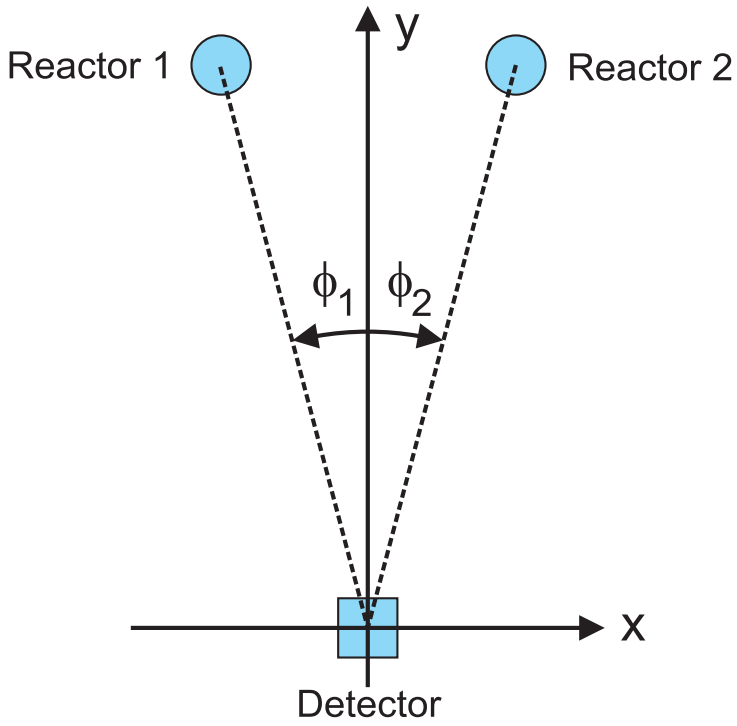

Figure 3.1: Geometric setup with two reactors and one detector. The angle ϕ_1 has positive sign and ϕ_2 has negative sign according to the mathematical sense of rotation.

the displacement vectors is a Gaussian with equal width L in each direction. In the first CHOOZ paper addressing the neutrino imaging of a reactor [18], an rms uncertainty for the neutron event reconstruction of 17–17.5 cm was given in their Fig. 2. Their Fig. 3 implies $L = 19$–20 cm and thus a positron event reconstruction uncertainty of 8–10 cm, in agreement with a similar result of the Borexino collaboration [25]. In a later CHOOZ publication [70], the rms uncertainty for the neutron event reconstruction was given as 19 cm. Assuming 9 cm for the average positron reconstruction uncertainty leads to

$$L = 21 \text{ cm}, \tag{3.3}$$

that we will use as our benchmark value. With the planned photomultiplier coverage in Double Chooz one does not expect to improve on this value [75] so that the CHOOZ characteristics provide a realistic estimate. For Double Chooz itself an independent quantitative estimate of this quantity is apparently not yet available, as Double Chooz will start data taking in 2008.

We will investigate a situation with two reactors that, together with the

detector, define the x-y-plane of our coordinate system. The y-axis is taken to point from the detector towards the reactors (Fig. 3.1). The detector views the reactors with azimuthal angles ϕ_1 and ϕ_2 relative to the y-direction. We have chosen ϕ_1 to have a positive and ϕ_2 a negative sense of rotation. The common zenith angle θ of both reactors is measured against the x-y-plane. We use $\theta = 0°$ for the true reactor locations, but in general θ can be a fit parameter (Sec. 3.3.4).

With this geometric setup, the two reactor sources produce a normalized distribution of positron-neutron displacement vectors $\mathbf{r} = (x, y, z)$ of

$$\begin{aligned} f(\mathbf{r}) &= \frac{1}{(2\pi)^{3/2}\, L^3}\, \exp\left[-\frac{(z+\ell\sin\theta)^2}{2L^2}\right] \times \\ &\sum_{i=1}^{2} b_i \exp\left[-\frac{(x+\ell\cos\theta\sin\phi_i)^2 + (y+\ell\cos\theta\cos\phi_i)^2}{2L^2}\right]. \end{aligned} \tag{3.4}$$

Here, b_i with $b_1 + b_2 = 1$ represent the individual reactor contributions to the total event number N. Moreover, we define the separation angle $\phi = |\phi_1 - \phi_2|$ and the average of the neutrino direction

$$\phi_c = b_1\phi_1 + b_2\phi_2\,. \tag{3.5}$$

3.2 Analytic Estimates

3.2.1 Width L of displacement-vector distribution

The width L of the distribution of the reconstructed positron-neutron displacement vectors $\mathbf{r}$ can be determined from the Double Chooz experiment itself. Assuming that the detector response is spherically symmetric, i.e. that the cylindrical detector has the same response in each direction, one can extract L from the z-distribution $f_z(z)$ of the displacement vectors. This distribution is equivalent to that from a single source, as we assume the detector to be in the same plane as the reactors (i.e. the x-y-plane). The distribution of L for many realizations, each with $N \gg 1$, is essentially Gaussian with

$$\frac{\sigma_L}{L} = \frac{1}{\sqrt{2N}}\,. \tag{3.6}$$

This equation stems from the usual distribution of standard deviations in statistics. One year's data provide L with a fractional precision of 1.7×10^{-3} so that its uncertainty is negligible for our further discussion. In addition, one could test deviations from the assumed Gaussianity of the distribution.

We will find that for realistic Double Chooz parameters the "double Gauss function" represented by Eq. (3.4) cannot be resolved and looks like a single, spherically symmetric Gaussian of width L. Therefore, in practice L can be determined from all three spatial directions or conversely, one can test if the detector response is indeed spherically symmetric.

3.2.2 Average neutron displacement ℓ

The average neutron forward displacement ℓ can be extracted from the y-distribution of the displacement vectors. Assuming a symmetric setup with $\phi_1 = -\phi_2 = \beta$, $f(\mathbf{r})$ factorizes as $f_x(x)f_y(y)f_z(z)$ and $f_y(y)$ is independent of the relative reactor strengths with

$$f_y(y) = \frac{1}{(2\pi)^{1/2}L} \exp\left[\frac{(y+\ell\cos\beta)^2}{2L^2}\right] \tag{3.7}$$

The average and variance are $\bar{y} = \ell\cos\beta$ and $\langle y^2 - \bar{y}^2\rangle = L^2$ so that

$$\begin{aligned} \ell &= \frac{\bar{y}}{\cos\beta}\,, \\ \frac{\sigma_\ell}{\ell} &= \frac{L}{\ell}\frac{1}{\cos\beta\sqrt{N}}\,. \end{aligned} \tag{3.8}$$

In Double Chooz we have $\phi = 2\beta = 30^\circ$ or $\cos\beta = 0.966$. For the purpose of determining ℓ, the two reactors almost act as a single source even at the near detector. After one year of data taking the $1\,\sigma$ uncertainty will be $\pm 2.9\%$. Scaled to 2,500 events, this forecast corresponds reasonably well to the ℓ uncertainty of $\pm 20\%$ found by CHOOZ.

3.2.3 Relative reactor strength

As a first nontrivial application we address the question of how well one can monitor the relative reactor strengths. With $\phi_1 = -\phi_2 = \beta$, only the x-distribution carries information on b_1 and b_2, and in particular

$$\begin{aligned} \bar{x} &= (b_1 - b_2)\,\ell\sin\beta\,, \\ \langle x^2 - \bar{x}^2\rangle = \int (x-\bar{x})^2 f(x)\,\mathrm{d}x &= L^2 + [(1-(b_1-b_2)^2]\,(\ell\sin\beta)^2\,. \end{aligned} \tag{3.9}$$

The variance is very close to L^2 because $L \gg \ell$. Setting

$$b = b_1 = 1 - b_2\,, \tag{3.10}$$

we can easily derive from Eq. (3.9) that

$$\begin{aligned} b &= \frac{1}{2}\left(1+\frac{\bar{x}}{\ell\sin\beta}\right), \\ \sigma_b &= \frac{L}{\ell}\frac{1}{2\sin\beta\sqrt{N}}. \end{aligned} \tag{3.11}$$

With $\sin\beta = 0.259$ we have after one year $\sigma_b = 0.053$. With $b = 0.5$ the $1\,\sigma$ uncertainty of each individual reactor strength is $\pm 10.7\%$, whereas the uncertainty of their sum is only $\pm 0.25\%$. Assuming a more favorable setup, based on the original Double Chooz proposal, with $\sin\beta = 0.707$ and $N = 10^6$ events, one obtains a monthly $1\,\sigma$ uncertainty of each individual reactor strength of $\pm 5.4\%$. According to [70] the monitoring of the neutron flux to determine the power output has a precision of 1.5%. However, this method has the advantage of operating continuosly. Nevertheless, the precision of our method has already the same order of magnitude and can provide an independent measurement of the thermal power.

3.2.4 Separation angle of reactors

We have seen that for the Double Chooz setup, the directional sensitivity of the near detector allows one to determine the integrated source strength of the two reactors separately, even though the uncertainty remains relatively large for one year of data. We now ask the opposite question if one can separate the "neutrino images" of the two reactor cores, assuming their relative strength is known, and assuming the detector characteristics L and ℓ have been established by other means precisely enough so that their uncertainty does not matter in the following.

We primarily discuss how well the separation angle $\phi = |\phi_1 - \phi_2|$ can be determined, assuming we know that there are exactly two sources in the x-y-plane that produce equal numbers of events. The obvious observables are the central coordinates $\bar{x}$, $\bar{y}$, and $\bar{z}$ of the displacement vector distribution and their variances.

At first one may think that the width of the observed distribution $f(\mathbf{r})$ is broadened in the x-direction if one has two sources because this distribution is a superposition of two Gaussian distributions of width L that are displaced relative to each other by the distance $2\ell\sin\beta$ where we have assumed $\phi_1 = -\phi_2 = \beta$. However, one easily finds in this case from Eq. (3.9) with $b_1 = b_2$

$$\langle x^2 - \bar{x}^2\rangle = L^2 + \ell^2\sin^2\beta\,. \tag{3.12}$$

The rms width of the x-distribution increases only quadratically in a small quantity with respect to the width L of a single source. For our parameters,

the rms width of the double Gauss function is the same as that of a single Gaussian within 3×10^{-4} and thus indistinguishable, even with five year's data of almost a million events. Analogous conclusions pertain to the higher moments of a single Gaussian compared to a double Gauss function when their separation is much smaller than their width. In other words, with the foreseen statistics of the Double Chooz near detector, the neutrino images of the two reactors are far too blurred to be separated. However, it is still possible to distinguish a single source from two sources if one takes advantage of the information encoded in the average coordinates of the displacement vector distribution. In the symmetric setup assumed here, information about the separation angle is provided by the distribution f_y that we have already used in Sec. 3.2.2 to determine ℓ if the separation angle is known. Turning this argument around we may instead solve for $\cos\beta$. Its uncertainty is

$$\sigma_{\cos\beta} = \frac{L}{\ell\sqrt{N}}\,, \tag{3.13}$$

which is 2.8×10^{-2} for our usual parameters and one year's data. If the separation angle is large, it can be ascertained with fairly good accuracy. On the other hand, for the Double Chooz geometry with $\cos\beta = 0.966$, the reactors could be barely separated on this basis, even with five year's data. Moreover, since the angular separation relies on a measurement of the quantity $\ell\cos\beta$, an independent precise determination of ℓ is necessary. Applying Eq. (3.13) to a single source with $\cos\beta = 1$ we have a $1\,\sigma$ uncertainty for the angular location of $(L/\ell)/\sqrt{N}$ that applies separately to the azimuthal and zenith angle. One year's data provide an angular uncertainty of $\pm 1.58°$. If both the azimuthal and zenith angle are not known, the corresponding $1\,\sigma$ half-cone aperture for the source location is 2.4°. Scaling this to 2,500 events leads to 19.2°, corresponding reasonably well to the CHOOZ value of 18° [18].

In a certain number of cases the value for $\cos\beta$ implied by the data will exceed unity and will thus be unphysical. In other words, in these cases one cannot distinguish a single source from two sources. Since $\cos\beta$ follows a Gaussian distribution and using the width Eq. (3.13), this will be the case with the "confusion probability"

$$p_{\text{confusion}} = \frac{1}{2}\left[1 + \operatorname{erf}\left(\frac{\cos\beta - 1}{\sqrt{2}\,\sigma_{\cos\beta}}\right)\right]. \tag{3.14}$$

This equation is derived from the cumulative distribution function of a Gaussian distribution and describes the probability that $\cos\beta$ is greater or equal to 1. For our usual parameters and one year's data we have $p_{\text{confusion}} = 10.9\%$. After five years this number reduces to 0.29%. Turning this around, in more

than 99.7% of all cases the data will imply the presence of two sources. Therefore, we estimate that the Double Chooz near detector takes five years to distinguish the two reactors from a single source with a $3\,\sigma$ confidence.

The reason for this relatively poor performance is that even for a separation angle as large as $\phi = 30°$, the relevant quantity $\cos(\phi/2) = 0.966$ is difficult to distinguish from 1 for the given statistics. On the other hand, if the separation angle is somewhat larger, the deviation of $\cos(\phi/2)$ from 1 itself quickly becomes of order unity so that $\cos(\phi/2)$ can be easily distinguished from 1. Assuming the same detector characteristics and $\phi = 90°$, we estimate that one could measure ϕ with a precision of a few degrees even after only one year.

On the other hand, determining the central angle ϕ_c, defined in Eq. (3.5) becomes more difficult if the separation angle is too large. For two equally strong reactors on opposite sides of the detector ($\phi = 180°$), the separation angle can be very well measured, whereas ϕ_c would remain poorly determined. One would conclude that there are two reactors at opposite sides without any information on their absolute direction.

3.2.5 Error estimate

Our estimates rely on the assumption that the uncertainties of the result are dominated by statistical errors. For the determination of the relative reactor powers the estimate is based on localizing the central value of the displacement-vector distribution, whereas the exact shape or Gaussian nature of the distribution is irrelevant. Therefore, we believe that here indeed statistical errors dominate.

The situation is very different for determining the separation angle of the reactors. Here the result depends on comparing the measured quantity $\ell \cos\beta$ with ℓ itself. In particular for small separation angles the result depends on subtracting two similar numbers so that the determination of a small β depends sensitively on how well ℓ is independently known. We have not specified how ℓ would be independently determined so that an objective budget of systematic errors is not available for this case.

3.3 Maximum likelihood estimate

3.3.1 The method of maximum likelihood

The analytic estimates of the previous section are based on simple properties of the displacement-vector distribution, notably the coordinates of its center

of gravity. Moreover, we have argued that the shape of the double-Gauss distribution Eq. (3.4) is very similar to that of a single Gaussian. Therefore, even for a five year exposure at the Double Chooz near detector, the shape of the displacement-vector distribution holds little additional information. If the shape mattered, it would be crucial to know from measurements or from Monte Carlo simulations of the detector how well it is represented by the double Gauss function of Eq. (3.4).

In order to demonstrate that our simple analytic estimates are correct we perform a maximum-likelihood analysis of the same cases as in the previous section, based on Monte Carlo data sets generated from the distribution Eq. (3.4). The Monte Carlo program was written in the Fortran. This exercise serves not only to corroborate the analytic estimates but also to show the distribution of quantities that are more difficult to extract analytically, if we, for example, do not assume that $\phi_1 = -\phi_2$ and have unequal reactor strengths. Moreover, with this method we can generate visualizations of our results.

The likelihood function of a set of N independently measured displacement vectors $\mathbf{r}_i = (x_i, y_i, z_i)$ is

$$L(\alpha) = \prod_{i=1}^{N} f(\mathbf{r}_i; \alpha)\,, \tag{3.15}$$

with $f(\mathbf{r}_i; \alpha)$ given here by Eq. (3.4), where α denotes the a priori unknown parameters b_1, b_2, ϕ_1, and ϕ_2. The set of parameters that maximizes the likelihood returns the best-fit points of a given data set. The maximum likelihood analysis is the most powerful analysis method for unbinned data. Therefore, it is useful to compare the analytic results of the previous section with the maximum-likelihood method applied to sets of Monte Carlo data. We have also displayed some characteristics of the maximum likelihood analysis in appendix A.

3.3.2 Relative reactor strength

As a first example we return to the task of determining the relative reactor strength. We assume that $\theta = 0°$ and $\phi_1 = -\phi_2 = 15°$ is known. Moreover, b is a free fit parameter according to Eq. (3.10), as the total number of detected neutrinos is, of course, known. Under these circumstances the distribution function factorizes and we will only keep $f_x(x)$ where we use $b_1 = b_2 = 0.5$ to generate Monte Carlo data sets for x with $N = 1.6 \times 10^5$ events (one year). For each realization we reconstruct b by a maximum-likelihood fit. In Fig. 3.2 we show the distribution of best-fit values from 1,000 runs together with a

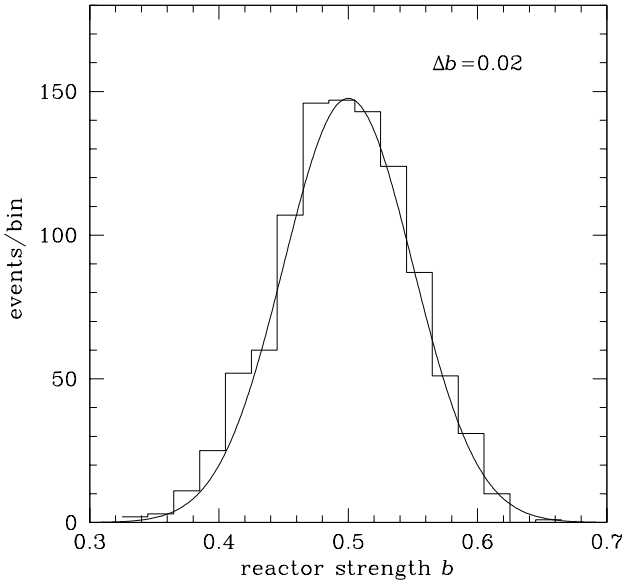

Figure 3.2: Distribution of best-fit values of the reactor strength b for 1,000 Monte Carlo realizations, assuming our usual parameters and 1 year of data. The bin width is $\Delta b = 0.02$. We also show a Gaussian of width $\sigma_b = 0.053$, representing the analytic estimate of Eq. (3.11).

Gaussian distribution centered at $b = 0.5$ and a width $\sigma_b = 0.053$ given by the analytic estimate Eq. (3.11). We see from this simple exercise that our analytic estimates can be confirmed with our Monte Carlo, as both results correspond very well to each other.

3.3.3 Reactor directions

As a next case we assume that the reactor strengths are known to be $b_1 = b_2 = 0.5$ and that the zenith angle for both sources is $\theta = 0°$, whereas the azimuthal reactor locations ϕ_1 and ϕ_2 are our fit parameters. Since the z-distribution factors out, we generate Monte Carlo data sets consisting of $N = 1.6 \times 10^5$ two-dimensional displacement vectors (x, y). For 5,000 Monte Carlo realizations we show the distribution of reconstructed best-fit central angles ϕ_c, according to Eq. (3.5) in the upper left panel of Fig. 3.3 together with a Gaussian of width 1.6°, which corresponds to the expected analytic width. Again we see that the numerical result agrees well with the analytical one. Our analytical results are therefore sufficient for a determination of the uncertainty of the separation angle in this simple symmetric setup. On the

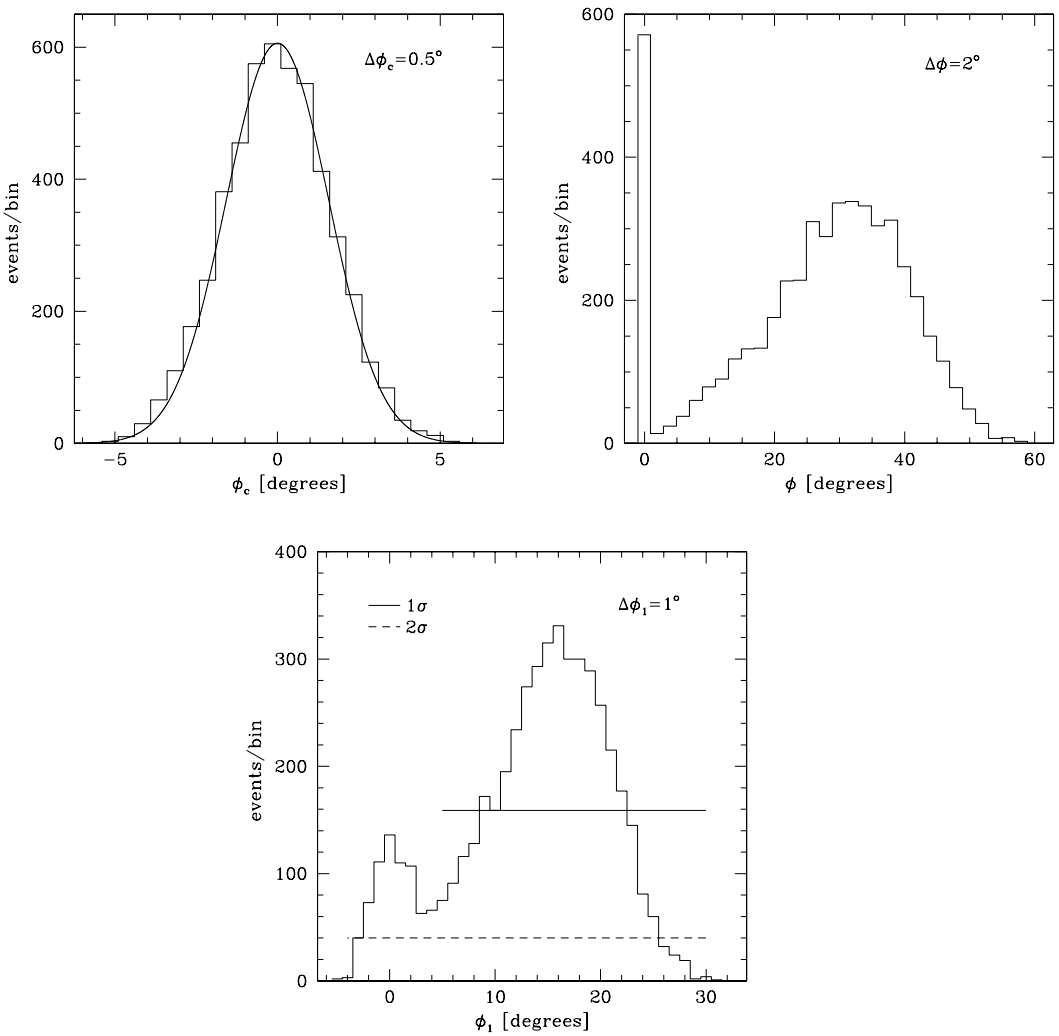

Figure 3.3: Best-fit central angles ϕ_c (*top left*), separation angles $\phi = |\phi_1 - \phi_2|$ (*top right*), and azimuthal reactor location ϕ_1 (*bottom*) for 5,000 Monte Carlo realizations of our fiducial setup with 1.6×10^5 events (one year). The different bin widths are indicated in each panel. In the top left panel we also show a Gaussian with the expected width of 1.6°. The conspicuous spike in the top right panel indicates all cases, where the two reactors have been identified as a single source. In the bottom panel, the horizontal solid line indicates the interval containing 68% of all values, the dashed line 95.4%.

other hand we could prove that our Monte Carlo delivers correct results. In the top right panel of Fig. 3.3 we show the corresponding distribution of best-fit separation angles $\phi = |\phi_1 - \phi_2|$. We defined this quantity here as a positive number because the reactors have equal strength and thus are not distinguishable. The distribution consists of a continuous component and a spike at $\phi = 0°$. This solution corresponds to those cases where the data prefer a single source as discussed in Sec. 3.2.4. According to Eq. (3.14) this confusion should arise in 10.9% of all cases, in good agreement with the size of the spike in Fig. 3.3 if we recall that the sum over all bins represents 5,000 Monte Carlo realizations. The continuous component, however, shows a peak at the true angle $\phi = 30°$.

Finally we show in the bottom panel of Fig. 3.3 the distribution of the reconstructed azimuthal reactor location ϕ_1. Since the two reactors are taken to have equal strength, they are not distinguishable so that the distribution for $-\phi_2$ is the same. The distribution is bimodal with one peak at the true location of $\phi_1 = 15°$ and another at the central angle $\phi_c = 0°$, corresponding to those cases where the two reactors cannot be distinguished from a single source. The width of this peak roughly corresponds to the width of the central-angle distribution in the top panel. This confirms our interpretation that we have a superposition of two distributions: one, where two reactors could be reconstructed and one, where the two sources appeared as a single source, as in this case $\phi_c = \phi_1 = \phi_2 = 0°$. We have also indicated where 68% (solid line) and 95% (dashed line) of all values fall around the best-fit value. Even though the distributions are not Gaussian, we refer to these regions as $1\,\sigma$, $2\,\sigma$ etc. intervals. The $1\,\sigma$ interval is approximately 12° wide, whereas the $2\,\sigma$ interval includes the secondary peak at 0°. As the number of events increases, the ϕ_1 distribution approaches a Gaussian and the peak at 0° decreases. It takes roughly five years of data to exclude this secondary peak from the $3\,\sigma$ confidence region.

In Fig. 3.4 we show the distribution of separation angles ϕ and of reactor locations ϕ_1 for 5,000 Monte Carlo realizations, each with 5 years of data ($N = 8 \times 10^5$). The spike at 0° of the separation-angle distribution has indeed decreased below 0.3%, confirming our earlier analytic estimate that with five year's data a $3\,\sigma$ separation of the Double Chooz reactors is possible. Note, however, that the peak around 0° of the ϕ_1 distribution remains in the $3\,\sigma$ region.

As a more optimistic case, we consider a hypothetical setup with a separation angle $\phi = 90°$. This case is motivated by the fact that the initial Double Chooz setup foresaw the near detector to be located much closer to the reactor cores. In this case one would also have expected about 1 Mio events in the near detector. Though we are choosing the optimistic setup for

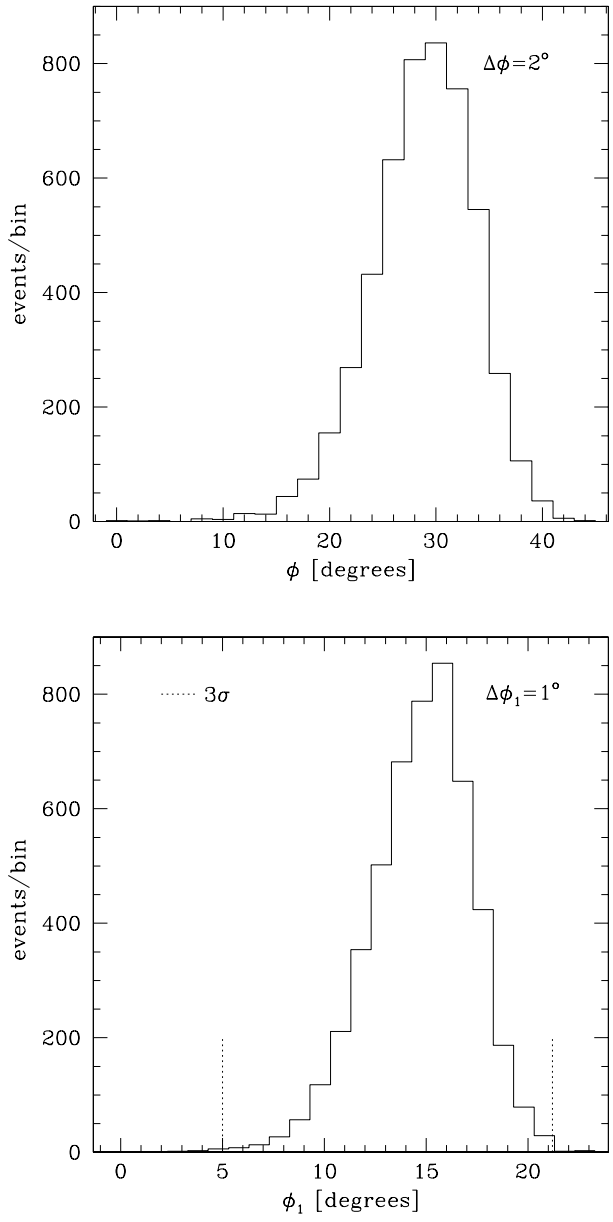

Figure 3.4: Best-fit separation angles ϕ (*top*) and reactor locations ϕ_1 (*bottom*) as in Fig. 3.3, here for $N = 8 \times 10^6$ (five years).

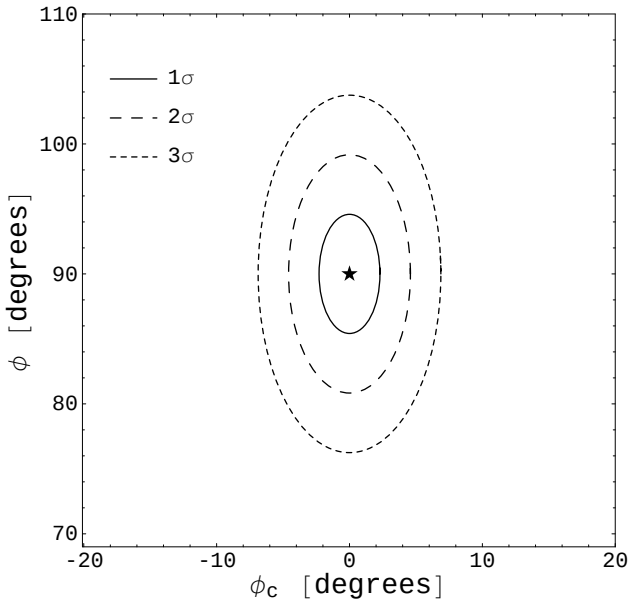

Figure 3.5: Likelihood contours of ϕ and ϕ_c for one Monte Carlo realization with $N = 1.6 \times 10^5$ events generated from a setup with separation angle $\phi = 90°$ and central angle $\phi_c = 0°$.

the angles, we will continue our analysis with $N = 1.6 \times 10^5$ events, as to show the impact on the precision that can be gained by geometry and not by statistics. The distributions of the reconstructed angles are essentially Gaussian in the relevant region around the best-fit values. With $N = 1.6 \times 10^5$, corresponding to 1 year at Double Chooz, the $1\,\sigma$ uncertainty for ϕ_1 is $\pm 3.2°$, for the central angle ϕ_c it is $\pm 2.3°$ and for the separation angle ϕ it is $\pm 4.6°$. We illustrate this case in Fig. 3.3.3 where we show the likelihood contours for ϕ and ϕ_c corresponding to 1, 2 and $3\,\sigma$ confidence regions. Note that the uncertainty of ϕ is twice that of ϕ_c and that of ϕ_c is worse than it was for a smaller separation angle.

3.3.4 Reactor directions with tilt

As a final example we include the zenith angle θ as a fit parameter. In other words, we generate Monte Carlo data sets for the full distribution function Eq. (3.4) consisting of $N = 1.6 \times 10^5$ displacement vectors. As a first case we show in Fig. 3.6 likelihood contours for ϕ_1 and θ when there is a single source and the data are analyzed with the prior assumption that indeed there is only a single source, i.e., assuming $\phi_1 = 0°$, $b_1 = 1$ and $b_2 = 0$. This figure

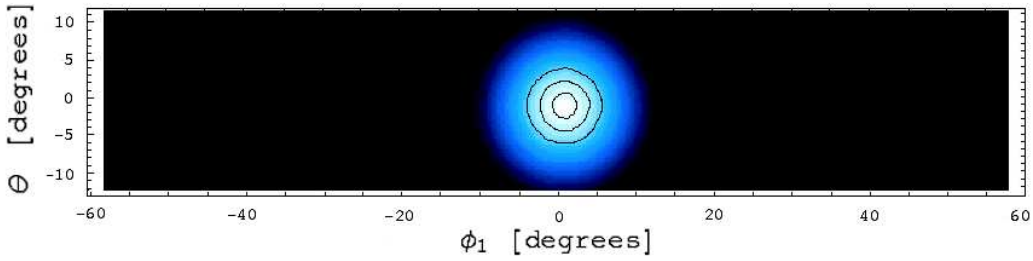

Figure 3.6: Likelihood contours of ϕ_1 and θ corresponding to 1, 2 and 3 σ confidence regions for a single reactor source. This figure is based on one Monte Carlo realization with $N = 1.6 \times 10^5$ events.

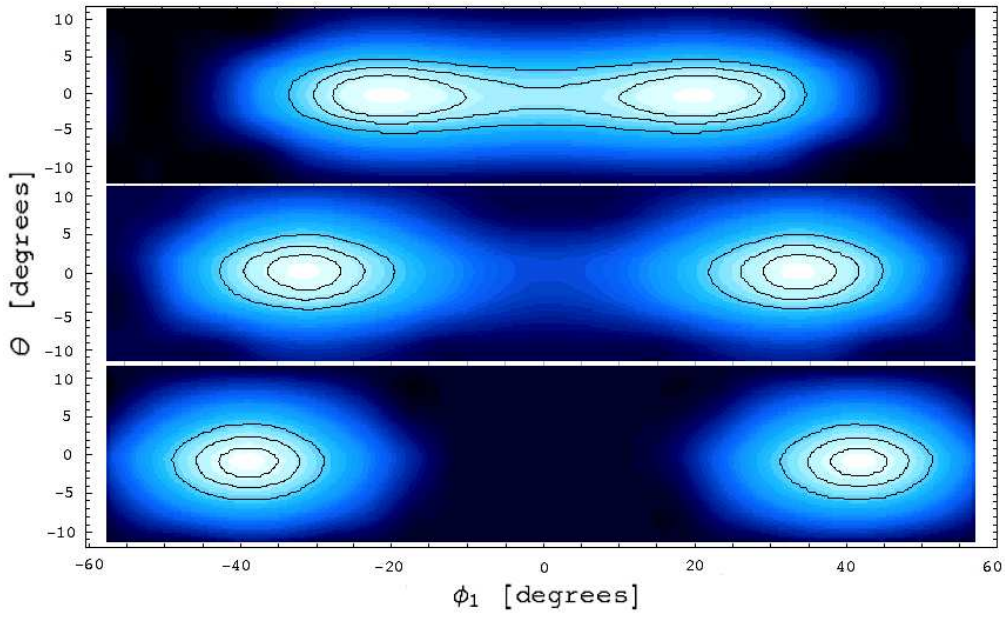

Figure 3.7: Likelihood contours projected onto the ϕ_1-θ plane, where the solid lines correspond to the 1, 2 and 3 σ confidence regions. From top to bottom the true separation angle was 30°, 70°, and 90°, respectively. Each panel shows a "typical" Monte Carlo realization consisting of $N = 1.6 \times 10^5$ events.

can be taken as a false-color neutrino image of a single reactor and illustrates the single-source imaging power of the near detector at Double Chooz. The solid lines correspond to the 1, 2 and $3\,\sigma$ contours.

Next we generate Monte Carlo realizations based on two sources with separation angles 30°, 70°, and 90°, respectively. The fit parameters of the maximum likelihood analysis are θ, ϕ_1, and ϕ_2, where both ϕ_1 and ϕ_2 can a priori vary in the entire interval from $-180°$ to $+180°$. In Fig. 3.7 we show likelihood contours for three "typical" Monte Carlo realizations projected onto the ϕ_1-θ plane. In our case of equal reactor strengths, $L(\theta, \phi_1, \phi_2) = L(\theta, \phi_2, \phi_1)$ so that the corresponding plot for ϕ_2 is identical.

The panels of Fig. 3.7 can be taken as false-color neutrino images of two reactors, although this interpretation must be used with care because we show the likely location of one of the reactors, not really the "images" of two neutrino sources.

For small separation angles, where the two "reactor images" merge, the interpretation of the shown contours as 1, 2 and $3\,\sigma$ confidence regions is only approximate. We also note that the distribution of zenith angles θ, after marginalizing over the azimuthal angles, is the same in all cases of Figs. 3.6 and 3.7 within statistical fluctuations.

3.4 Summary of chapter 3

We have extended the study of the directional sensitive measurement of the neutrino flux to reactor neutrino experiments that are currently designed to measure θ_{13}. We have investigated the "neutrino imaging power" of the Double Chooz near detector that will collect as many as 1.6×10^5 events per year. For realistic assumptions derived from the properties of the previous CHOOZ experiment, the width of the distribution of reconstructed displacement vectors is about ten times larger than the displacement itself, leading to an extremely blurred neutrino image of a reactor.

For a single source, this image can be sharpened with enough statistics so that its direction can be determined with very good precision. At Double Chooz we obtain the average neutrino direction with a $1\,\sigma$ half-cone aperture of 2.4° with one year of data.

However, with the given statistics, the images of two or more sources merge completely in the sense that the shape of the displacement-vector distribution is indistinguishable from that of a single source. Yet the average of all measured displacement vectors still contains nontrivial information on the source directions. It is very difficult to separate two sources if their angular distance ϕ is so small that $1 - \cos(\phi/2) \ll 1$. Thus for Double

Chooz we find that the setup is ineffectual for a clear separation of the reactors. After 5 years of Double Chooz, the reactors can be separated at the $3\,\sigma$ level. This estimate is based on statistical errors alone and requires a precise determination of the average neutron displacement ℓ by independent methods.

With increasing separation angle it becomes much easier to distinguish the reactors. For a setup with $\phi = 90°$, even one year's data would be enough to measure the separation angle to about $\pm 10°$ at $3\,\sigma$. The early plans for Double Chooz envisioned the near detector to be much closer to the reactors, not only providing ten-fold larger statistics, but also a much larger separation angle. In the original setup, the angular separation of the two sources would have been straightforward.

For Double Chooz, the location of the reactors is perfectly known, of course. In this case one can use the angular sensitivity to determine the two reactor strengths from the neutrino signal alone and one can determine the detector response characteristics L and ℓ from the same data. At $1\,\sigma$, the one-year integrated power of one of the reactors can be determined to $\pm 11\%$, the five-year integrated value to $\pm 4.8\%$. The total event rate over these periods is determined within $\pm 0.25\%$ and $\pm 0.11\%$, respectively.

Chapter 4

Diffuse Supernova Neutrino Background

In the following chapter we discuss a so far undetected source of neutrinos, namely diffuse supernova neutrinos. The neutrinos have accumulated since the first stars ended in supernova (SN) explosions and form now an overall cosmic background. This neutrino background can be explored with the next generation of neutrino experiments such as LENA or GLACIER [34] as well as a Gd-loaded Super-Kamiokande [37] or MEMPHYS detector [34]. As core collapse supernovae are rare, diffuse supernova neutrinos could well be the next messengers from these events. The first SN neutrinos observed originated from SN 1987A that exploded in the Large Magellanic Cloud, a satellite galaxy of our Milky Way. Thereby approximately 20 events have been measured with neutrino detectors [76, 77]. With ongoing developments in neutrino experiments presently several ten-thousand events would be expected, if a SN exploded in our galaxy. In LENA one expects roughly 10^4 $\bar{\nu}_e$, whereas in MEMPHYS 10^5 events would be expected for a SN at 10 kpc. However, for the detection of ν_x via elastic scattering one expects almost 10^4 events in LENA, an order of magnitude higher than for MEMPHYS. GLACIER could deliver a complementary detection in the neutrino sector, as 10^4 ν_e events could be registered. For a full comparison of all channels see [34]. As it is not clear when the next SN will happen, we will rather concentrate on the diffuse supernova neutrino background (DSNB) that has the advantage of being present and ready to detect.

In the following we discuss the expected DSNB spectra and the parameters that enter the calculation. The expectation to gain new information on core collapse supernovae and star formation history are high and one can often find statements in the literature that a future measurement of the DSNB could reveal considerable new information. However, the number of param-

eters that influence the DSNB spectrum is large and information on these parameters is limited. Therefore, we conduct a sensitivity forecast for a possible measurement of the relevant DSNB parameters in a liquid scintillator detector or a liquid argon detector. We discuss what can be learned about an individual SN and the star formation parameters. We focus on LENA and GLACIER, as a pure water Cherenkov detector like MEMPHYS does not seem as promising and its performance has been discussed elsewhere [34, 37]. GLACIER can in principle also detect anti-neutrinos. However, the cross section in the energy range relevant for DSNB detection is by about one order of magnitude lower than for neutrinos according to Fig. 1.7. Moreover, we analyze the properties of an analytical fit to an assumed measured DSNB spectrum and again conduct an error forecast. We include also an extensive discussion of the backgrounds for a DSNB measurement in LENA.

4.1 Diffuse supernova neutrino spectrum

The diffuse supernova neutrino spectrum at Earth that can be measured at a detector is just the red-shifted superposition of all individual SN neutrino spectra in an expanding flat universe and can be expressed as

$$\Phi(E) = \int_0^\infty \mathrm{d}z \, \frac{N_{\mathrm{SN}}[E(z+1)]R_{\mathrm{SN}}(z)}{H_0\sqrt{(z+1)^3\Omega_{\mathrm{m}}+\Omega_\Lambda}} \,. \tag{4.1}$$

Equation (4.1) is a convolution of several elements that we will discuss in more detail in the subsequent sections. The main features of the formula, however, can be easily understood. $N_{\mathrm{SN}}[E(z+1)]$ is the neutrino energy spectrum of an individual SN, where the time of explosion has been considered in the argument with a red-shift factor $(z+1)$. Note, that E is the present-day neutrino energy. Moreover, the SN rate $R_{\mathrm{SN}}(z)$ depends on the red-shift. By now it is firmly established that our universe is flat [79]. Therefore, we can consider the expansion in a flat universe with the denominator in Eq. (4.1), according to [80]. Hereby, $H_0 = 0.72\,\mathrm{km\,sec^{-1}\,Mpc^{-1}}$ is the Hubble expansion rate and $\Omega_{\mathrm{m}} = 0.3$ and $\Omega_\Lambda = 0.7$ are the matter and energy density in a flat universe [81]. In the following we discuss the elements of Eq. (4.1) in more detail.

4.1.1 Supernova neutrino spectrum at the source

For our discussion of the DSNB the shape of the SN neutrino spectrum, the mean energy of each neutrino flavor and the total binding energy of a SN are

of crucial importance. Moreover, a discussion of the oscillations inside the dying star is necessary.

Generally, the total binding energy released by a collapse of a homogeneous iron core is given as

$$E \approx \frac{3}{5}\frac{G_N M^2}{R}\,, \tag{4.2}$$

where M is the mass of the iron core and G_N is Newton's gravitational constant. Typically, one often takes $M \approx 1.44 M_\odot$, where $M_\odot$ is the solar mass ($1.99 \times 10^{33}\,\mathrm{g}$), which renders a binding energy of $E \approx 3 \times 10^{53}\,\mathrm{erg}$. The mass $M = 1.44 M_\odot$ is the Chandrasekhar limit, which is the largest mass that can be supported by the pressure of degenerate electrons against gravitational collapse [82, 83]. Electrons are absorbed by nuclei and protons in the core of the star and thereby neutrinos are released via the process

$$p + e^- \rightarrow n + \nu_e\,. \tag{4.3}$$

Due to the high density inside the dying star (up to nuclear densities of $10^{15}\,\mathrm{g\,cm^{-3}}$) neutrinos are trapped and all neutrino flavors are in equilibrium. It is expected that the total energy is approximately equally distributed on the the six neutrino and anti-neutrino species. The differences between neutral and charged current interactions in stellar matter lead to a difference in the size of the neutrino sphere for different flavors. The collapsing core is more transparent for muon and tau neutrinos and thus their last interactions occur deeper in the star than for electron neutrinos, resulting in a higher muon and tau neutrino energy. There is an additional difference between electron neutrinos and anti-neutrinos as generally more neutrons are found in the core than protons, leading to a lower ν_e energy compared to $\bar{\nu}_e$. Generally it has been found in simulations [21, 20, 19, 84, 85, 86, 87, 88, 89]

$$\begin{aligned}
\langle E_{\nu_e} \rangle &\sim 10 - 14\,\mathrm{MeV} \\
\langle E_{\bar{\nu}_e} \rangle &\sim 11 - 20\,\mathrm{MeV} \\
\langle E_{\nu_x} \rangle &\sim 15 - 27\,\mathrm{MeV} \;\text{ for }\; \nu_\mu, \nu_\tau, \bar{\nu}_\mu, \bar{\nu}_\tau\,.
\end{aligned} \tag{4.4}$$

To be more accurate on these energy values we present the results of specific groups. The Livermore group finds that the mean neutrino energies show a pronounced hierarchy $\langle E_{\nu_e} \rangle : \langle E_{\bar{\nu}_e} \rangle : \langle E_{\nu_x} \rangle = 0.8 : 1 : 1.26$ at 300 ms and $0.55 : 1 : 1.25$ at 10 s after the bounce [19]. The total energy is approximately equipartitioned on all flavors, which has been traditionally found in simulations [19, 20, 90, 91, 92]. Keil, Raffelt and Janka have conducted a different analysis with a new way of ν_x transport inside the star and they find that the

hierarchy, especially between $\bar{\nu}_e$ and ν_x is not as pronounced as the one of the Livermore group, and that the energies differ only by 10-20% [21]. Also the luminosities of the ν_x are not equal to those of ν_e and $\bar{\nu}_e$, but can be smaller by a factor of two at early times and larger at late times [21, 89, 93, 94].

The neutrino spectra of different simulations can be characterized by a small number of meaningful parameters. The parameterization that shall be used in the following was introduced by Keil *et al.* [95]. The spectrum of an individual SN is given by

$$N_{\mathrm{SN}}(E) = \frac{E_{\mathrm{tot}}}{\langle E\rangle^2\,(a+1)^{(-a-1)}\Gamma(a+1)}\left(\frac{E}{\langle E\rangle}\right)^a \exp\left[-(a+1)\frac{E}{\langle E\rangle}\right], \quad (4.5)$$

where E_{tot} is the total energy released in a certain neutrino species, $\langle E\rangle$ the average neutrino energy and a the spectral pinching [96]. Moreover, we have

$$\int_0^\infty \mathrm{d}E N_{\mathrm{SN}}(E) = \frac{E_{\mathrm{tot}}}{\langle E\rangle}\,, \quad (4.6)$$

which is just the number of neutrinos released by the SN. A value of $a = 2$ renders a spectrum equal to a thermal Maxwell-Boltzmann spectrum. If $a > 2$ the high energy tail is suppressed, which leads to a so called pinched spectrum. If $a < 2$ the high energy tail is enhanced and the peak is suppressed (anti-pinched spectrum). Generally simulations find values of a between 2 and 5 for the instantaneous spectrum [96]. For the sake of illustration we show the spectra generated with Eq. (4.5) for different values of a with $\langle E\rangle = 15$ MeV in Fig. 4.1, where the number of released neutrinos is normalized to 1.

However, due to neutrino oscillations the spectra of the respective flavors will change when the neutrinos leave the star. A detailed analysis of oscillations in the SN envelope has been conducted by Dighe and Smirnov [97]. After oscillations one obtains for the neutrino and anti-neutrino fluxes

$$\begin{aligned}\Phi_{\bar{\nu}_e} &= \bar{p}\,\phi_{\bar{\nu}_e} + (1-\bar{p})\phi_{\bar{\nu}_x}\\ \Phi_{\nu_e} &= p\,\phi_{\nu_e} + (1-p)\phi_{\nu_x},\end{aligned} \quad (4.7)$$

where $\phi_{\bar{\nu}_e}\,(\phi_{\nu_e})$ and $\phi_{\bar{\nu}_x}\,(\phi_{\nu_x})$ are the initial neutrino fluxes and $p\,(\bar{p})$ is the $\nu_e\,(\bar{\nu}_e)$ survival probability, which is generally a function of the mixing angles θ_{12} and θ_{13}. There are three main cases:

1. adiabatic normal mass hierarchy with large θ_{13}: at matter densities of $\sim 10^3\,\mathrm{g\,cm^{-3}}$ neutrinos undergo resonant conversion. As the propagation is adiabatic we have $p = 0$. For anti-neutrinos we have $\bar{p} = \cos^2\theta_{12}$.

2. adiabatic inverted mass hierarchy with large θ_{13}: propagation is adiabatic for neutrinos and anti-neutrinos with a resonant conversion occurring only for anti-neutrinos, resulting in $p = \sin^2\theta_{12}$ and $\bar{p} = 0$.

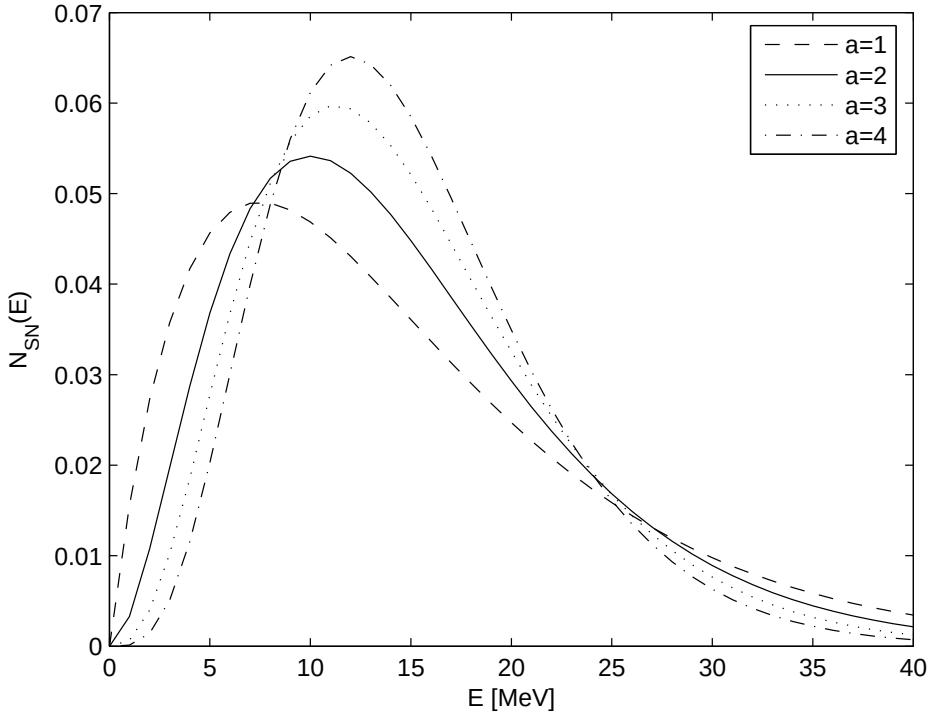

Figure 4.1: Shape of the neutrino energy spectra for different values of a. For illustration we have chosen $\langle E \rangle = 15$ MeV and normalized the spectrum to 1.

3. non adiabatic case with small θ_{13}: no resonant conversions possible with $p = \sin^2 \theta_{12}$ and $\bar{p} = \cos^2 \theta_{12}$.

We refer to small θ_{13} for values $\sin^2 \theta_{13} < 2 \times 10^{-6}$ and to large θ_{13} for values $\sin^2 \theta_{13} > 3 \times 10^{-4}$ [98]. When assuming a moderate hierarchy between the mean energies of the neutrino flavors we observe that the mean energy of the anti-neutrino spectrum is generally less influenced than the neutrino spectrum where a complete conversion of ν_x to ν_e can occur. This effect could enhance the mean energy quite significantly. However, latest findings seem to open this discussion anew, as collective oscillation phenomena play an important role, especially in case of inverted neutrino hierarchy. In these scenarios one considers non-linear effects due to neutrino-neutrino interactions for non-zero θ_{13} [99, 100]. As this is still a matter of current research, we will chose plausible values for the mean neutrino energy. We will return to this discussion in Sec. 4.3.1, when we introduce our fit method and chosen

parameters.

4.1.2 Star formation and supernova rate

Besides the neutrino spectra produced in an individual SN explosion we also need to know the rate, at which supernovae explode and its evolution with redshift. This can either be obtained with direct observations of SN explosions or by combining the observed star formation rate with the initial mass function.

There are several searches attempting to directly measure the SN rate [101, 102, 103, 104, 105, 106]. Observational problems are encountered, however, in the limiting magnitude and resolution of optical telescopes. Moreover, supernovae might appear fainter in inclined spiral galaxies or behind unknown dust-fields. Another limiting factor is the lack of statistics of an individual search. A combined analysis of all searches has been obtained e.g. by Capellaro *et al.* [107].

The alternative way of determining the SN rate via the star formation rate has the advantage of having less statistical errors. The connection between star formation rate and SN rate is obvious. The lifetime of SN progenitor stars is short compared to the time since the onset of star formation. If we assume that all stars with a mass larger than a critical mass M_{crit} end as core collapse supernovae and that each dying star is always replaced by a new born progenitor we obtain a SN rate of

$$R_{\mathrm{SN}}(z) = \frac{\int_{M_{\mathrm{crit}}}^{\infty} \mathrm{d}m\ \phi(m,z)}{\int_{M_{\mathrm{cutoff}}}^{\infty} \mathrm{d}m\ m\phi(m,z)}\, \psi_\star(z), \tag{4.8}$$

where $\phi(m,z)$ is the initial mass function, $\psi_\star(z)$ is the star formation rate at redshift z and $M_{\mathrm{crit}} \approx 8M_\odot$ is the minimal mass required for a star to end as a SN. M_{cutoff} is the cutoff for low stellar masses, which is set to about $0.5M_\odot$, the mass of brown dwarfs. The standard Salpeter initial mass function is denoted as $\phi(m,z) \propto m^{-2.25}$. We can drop the z-dependence as for low redshifts ($z < 2$) the initial mass function can be assumed as constant [108]. Additionally, in our case diffuse SN neutrinos are below detection threshold for higher redshifts. Assuming a lower cutoff $M_{\mathrm{cutoff}} = 0.5M_\odot$ and $M_{\mathrm{crit}} = 8M_\odot$ we obtain

$$R_{\mathrm{SN}}(z) = 0.0122 M_\odot^{-1} \psi_\star(z)\,. \tag{4.9}$$

A parametrization for the star formation rate $\psi_\star(z)$ and thus the SN rate has been introduced by Hogg [109] and Baldry *et al.* [110]. We use this parame-

terization and have

$$R_{\rm SN} = R_0 \begin{cases} (z+1)^\beta & \text{for } z < 1 \\ 2^{(\beta-\alpha)}(z+1)^\alpha & \text{for } 1 \leq z < z_{\rm max} \\ 0 & \text{for } z > z_{\rm max} \end{cases} , \tag{4.10}$$

where R_0 is the present day SN rate, α represents the early star formation history and β the late star formation history [111]. The most recent measurements of these parameters have been obtained by the GALEX experiment as $\alpha = 0.5 \pm 0.4$ and $\beta = 2.5 \pm 0.7$ [112]. The GALEX (GALaxy Evolution EXplorer) is an ultraviolet space telescope. For the onset of star formation, $z_{\rm max}$, several measurements exist, but as almost exclusively neutrinos from SN with $z \leq 5$ are registered in our detectors [78] we omit a further discussion of this issue and fix $z_{\rm max} = 5$, which does not change our conclusions.

For the local SN rate $R_0 = R_{\rm SN}(z = 0)$ several analysis have been conducted ranging from e.g. 0.6–3.6 $\times 10^{-4}\,{\rm yr}^{-1}{\rm Mpc}^{-3}$ [113], $0.66 \pm 0.25 \times 10^{-4}\,{\rm yr}^{-1}{\rm Mpc}^{-3}$ [107] or $0.9 \pm 0.4 \times 10^{-4}\,{\rm yr}^{-1}{\rm Mpc}^{-3}$ and $1.7 \pm 0.9 \times 10^{-4}\,{\rm yr}^{-1}{\rm Mpc}^{-3}$ as obtained by Ref. [106]. In a recent analysis Strigari *et al.* come to the conclusion that relatively high values of R_0 are favored [114]. Their upper allowed value lies at $R_0 \sim 2.6 \times 10^{-4}\,{\rm yr}^{-1}{\rm Mpc}^{-3}$.

4.2 Backgrounds in LENA

In order to determine the energy window, in which a measurement of the DSNB is possible, we have to discuss possible backgrounds to the detection. In the following we discuss the backgrounds expected in LENA, however, these considerations are valid for all liquid scintillator detectors. Moreover, some of the backgrounds are present in all experiments that attempt a DSNB detection[1].

A large fraction of the $\bar{\nu}_e$ events cannot be attributed to the DSNB because of the background events due to $\bar{\nu}_e$ generated both by air showers and nuclear power plants. These are indistinguishable from the $\bar{\nu}_e$ of the DSNB and therefore independent of the type of detector used.

[1]Our discussion is based on the analysis conducted by M. Wurm, F. von Feilitzsch, M. Göger-Neff, K. A. Hochmuth, T. Marrodán. Undagoitia, L. Oberauer and W. Potzel, Phys. Rev. D **75**, 023007 (2007). In this work the ability of LENA to distinguish between the predictions for the DSNB fluxes obtained by different simulations has been investigated by means of a Monte Carlo analysis. For this thesis we only adopt the discussion concerning the expected backgrounds.

4.2.1 Reactor $\bar{\nu}_e$

For energies below $\sim$ 10 MeV, the man-made background due to nuclear reactors sets a lower threshold for the DSNB detection. The $\bar{\nu}_e$ are generated by the β^- decay of neutron-rich fission products of ^{235}U, ^{238}U, ^{239}Pu and ^{241}Pu inside the reactor. As the reactor $\bar{\nu}_e$ flux is quadratically declining with distance, at least the closest reactors must be considered for a good estimate of the actual flux in the detector.

Above the Q-value of 1.8 MeV, the spectral shape of the reactor neutrinos is best known up to energies of $E_{\bar{\nu}_e} = 8$ MeV, both from experimental data and from theoretical calculations that have used the fission yields and β^- decay schemes of the isotopes in question. However, as the DSNB flux is several orders of magnitude lower than that of the reactor neutrinos, it is necessary to take the high-energetic tail of their spectrum (up to $E_{\bar{\nu}_e} \approx$ 13 MeV) into account when determining the lower detection threshold for DSNB observation.

Especially for energies above 8 MeV, the exact spectrum of the reactor $\bar{\nu}_e$ cannot be measured directly at a reactor because of the poor statistics. Instead, the spectrum is deduced from fission yields, β^- endpoint energies and decay schemes of the neutron-rich isotopes produced in a reactor. The experimental challenge is set by the extremely neutron-rich isotopes with high Q-values and lifetimes in the range of 10^{-2} seconds. Tengblad *et al.* [115] have indirectly determined the reactor neutrino spectrum up to an energy of 12 MeV by a measurement of the beta-decay spectra of the relevant fission products of ^{235}U, ^{238}U, ^{239}Pu. These three elements are, on average, responsible for about 92 % of the fission processes (see Tab. 4.1) and therefore of the neutrino flux generated by the reactor [116]. In contrast to ^{238}U, ^{241}Pu contributes only a small portion of the fission products emitting high energetic neutrinos. For this reason, the spectral contribution of ^{241}Pu can be neglected to a good approximation.

However, there is at least one additional element known to be produced in fission processes which has an even higher β^- endpoint energy: ^{94}Br with a Q-value of 13.3 MeV [117]. Due to its short lifetime of 70 ms and its low fission yields (as shown in Tab. 4.1) its exact β^- decay scheme is not known [118]. Thus, we are only able to give an upper limit for its contribution to the spectrum, using its fission yield, Q-value, and the information that it decays in 70 % of all cases without emitting an additional neutron [118].

Using the reactor $\bar{\nu}_e$ spectrum just described, the reactor background flux and the event rates in LENA have been calculated for a number of different locations: At present Pyhäsalmi (Finland) and Pylos (Greece) are the preferred detector sites. The Laboratoire Souterrain de Modane (LSM) at

Frejus (France) was included as an example for a middle-European detector site. The US American sites Kimballton, Henderson, and Homestake Mine were used as they have expressed interest in a LENA-like liquid-scintillator detector. Meanwhile it has been decided that the Homestake Mine will be the home Deep Underground Science and Engineering Laboratory (DUSEL). Hawaii and New Zealand were chosen as they are far away from the nuclear power plants on the northern hemisphere and are from this point of view optimal detector sites for observing the DSNB.

When calculating the $\bar{\nu}_e$ flux, in a first step the number of neutrinos emitted per second by a nuclear reactor, $R_{\bar{\nu}_e}$, can be derived as

$$R_{\bar{\nu}_e} = N_{\nu,\mathrm{fiss}} \frac{P_{\mathrm{th}}}{E_{\mathrm{fiss}}} e = (1.38 \pm 0.14)\, 10^{20} P_{\mathrm{th\,[GW]}}\, \mathrm{s}^{-1}, \tag{4.11}$$

where $N_{\nu,\mathrm{fiss}} \simeq 6$ [74] and $E_{\mathrm{fiss}} = 205.3 \pm 0.6$ MeV [119] are the average number of neutrinos and the mean energy produced per fission, respectively, $\mathrm{P_{th}}$ is the thermal power of the reactor and $e = 0.75 \pm 0.06$ [120] is the average fraction of time that a reactor is running (energy availability factor e). The thermal power P_{th} can be found in the online databases of the International Atomic Energy Agency (IAEA) [120].

In a next step, using the coordinates of each reactor and the detector site their distance d can be found. The flux without oscillations can be calculated dividing $R_{\bar{\nu}_e}$ by $4\pi d^2$.

Finally, for each distance to a particular power plant the effect of oscillations $\bar{\nu}_e \rightarrow \bar{\nu}_{\mu,\tau}$ has to be taken into account. This was achieved by convoluting the normalized spectrum $F(E)$ with the energy-dependent oscillation

Table 4.1: Contributions of the fission products of uranium and plutonium to the fission processes and therefore to the $\bar{\nu}_e$ flux emitted by a reactor (averaged over time) [116]. The last column shows the fission yields of the high-endpoint β-emitter ^{94}Br [117].

Isotope	Contribution to total fission rate	^{94}Br fission yield
^{235}U	0.59	1.66×10^{-6}
^{238}U	0.04	7.90×10^{-5}
^{239}Pu	0.285	2.71×10^{-5}
^{241}Pu	0.075	1.05×10^{-6}

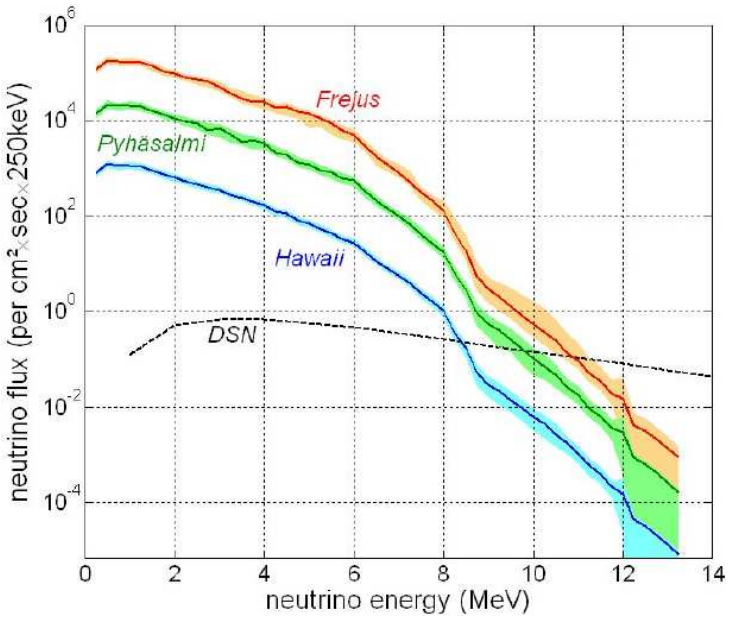

Figure 4.2: Spectra of reactor $\bar{\nu}_e$ at Frejus, Pyhäsalmi and Hawaii. Shaded regions correspond to experimental and model uncertainties. Above 12 MeV, we added an upper limit for the spectral contribution of ^{94}Br neutrinos. For comparison, an approximate DSNB spectrum according to a conservative model based on the SN spectrum given by [96] with $R_0 = 0.6 \times 10^{-4}\,\mathrm{yr}^{-1}\,\mathrm{Mpc}^{-3}$ is shown.

Table 4.2: Reactor $\bar{\nu}_e$ fluxes and event rates for LENA with for an exposure of 0.5 Mton-years at various detector locations. Uncertainties of both fluxes and event rates are $\sim 14\,\%$.

Detector Location		flux ($\mathrm{cm}^{-2}\,\mathrm{s}^{-1}$)	events (0.5 Mton-years)
Kamioka	(J)	2.1×10^6	2.5×10^5
Frejus	(F)	1.6×10^6	2.0×10^5
Kimballton	(US)	6.4×10^5	7.3×10^4
Pyhäsalmi	(FIN)	1.9×10^5	2.1×10^4
Pylos	(GR)	9.2×10^4	11.5×10^3
Homestake	(US)	7.5×10^4	8.6×10^3
Henderson	(US)	7.4×10^4	8.4×10^3
Hawaii	(US)	10.9×10^3	12.4×10^2
Wellington	(NZ)	5.4×10^3	6.2×10^2

probability and weighing it with the expected integral flux,

$$\Phi(E,d)=\frac{R_{\bar{\nu}_e}}{4\pi d^2}F(E)\left(1-\sin^2 2\theta_{12}\sin^2\frac{\pi d}{\ell(E)}\right), \tag{4.12}$$

where $\ell(E)$ is the oscillation length and θ_{12} the solar mixing angle (see also appendix A). This procedure was repeated for all reactors and the individual fluxes were summed for different detector locations. The necessary data concerning the coordinates was taken from the International Nuclear Safety Center (INSC) [121] and includes all major power plants running worldwide in the year 2005. Future changes as the launch of the Finnish nuclear plant TVO3 as well as the possible shutdown of Swedish plants have not been taken into account but will not substantially change the $\bar{\nu}_e$ fluxes. The integral $\bar{\nu}_e$ fluxes and the corresponding event rates for LENA are summarized in Tab. 4.2. The calculated flux ($\phi = 2.1 \times 10^6\,\mathrm{cm^{-2}\,s^{-1}}$) in the Kamioka mine (Japan) is comparable to the one measured by KamLAND according to Ref. [122]. In addition, Fig. 4.2 shows the energy spectra of the reactor $\bar{\nu}_e$ at Frejus, Pyhäsalmi and Hawaii, i.e. at a high, medium and low-flux site.

For an estimate of the overall uncertainties, we have taken into account possible deviations due to the fraction of annual runtime e as well as the temporal variation of the abundances of Uranium and Thorium isotopes ($\sim 5\,\%$) [116]. In addition, the most recent values and uncertainties of the oscillation parameters $\Delta m^2_{12} = 8.2^{+0.6}_{-0.5} \times 10^{-5}\,\mathrm{eV}^2$ and $\tan^2\theta_{12} = 0.40^{+0.10}_{-0.07}$ [123] have been included in the calculations. In Fig. 4.2, these overall uncertainties are indicated as shaded regions.

4.2.2 Atmospheric $\bar{\nu}_e$ background

The flux of the atmospheric $\bar{\nu}_e$ is increasing with energy in the relevant energy range and starts to surpass the DSNB signal at energies around 25 MeV.

Table 4.3: Dependence of the total atmospheric neutrino flux below 60 MeV on the detector location. The scaling factor s_{atm} compares this flux to the one at the Kamioka site.

Site	Latitude (N)	s_{atm}
Hawaii	1.5°	0.8
Kamioka, Pylos, Kimballton	36.5°, 36.6°, 37.4°	1
Henderson, Wellington	39.8°, -41.5°	1.25
Frejus, Homestake	45.1°, 44.3°	1.5
Pyhäsalmi	63.7°	2.0

However, the total flux of atmospheric $\bar{\nu}_e$ depends on the geographic (geomagnetic) latitude and therefore on the detector site [124]. The individual spectra can be calculated using Monte Carlo methods. However, for easier comparison and in accordance with publications by Ando and Sato [78, 81] we have extrapolated the model spectra calculated by Gaisser *et al.* [124] (including the corrections by Barr *et al.* [125]) to energies below 60 MeV. We have estimated the atmospheric $\bar{\nu}_e$ spectra for high geomagnetic latitudes as, for instance, for Pyhäsalmi using the 3D simulations by Liu *et al.* [126].

As the energy spectrum of the atmospheric $\bar{\nu}_e$ only mildly depends on location [124], we have left the spectrum unchanged and have only taken into account the dependence of the total flux on the detector site. Table 4.3 shows our results. The total flux of atmospheric $\bar{\nu}_e$ at a particular site can be related to the flux at the Kamioka site by a scaling factor s_{atm}.

In water Cherenkov detectors, atmospheric ν_μ and $\bar{\nu}_\mu$ provide an additional background source by creating "invisible muons" [78] with energies below the Cherenkov threshold. However, such muons do not pose a background in a liquid-scintillator detector due to its different detection mechanism.

4.2.3 Cosmogenic background

Up to now, the discussion only included background events due to additional $\bar{\nu}_e$ sources. However, muons that pass the detector or the surrounding medium (rock or water) also have to be considered. Most of the spallation products of these muons can be easily discriminated from the signal due to the signature of the inverse beta decay. Still, radionuclides like the β-n-emitter ^{9}Li [127] or fast neutrons can mimic this e^+-n coincidence. For an estimate of the rates, only events in the energy window from 10 to 25 MeV have to be considered. All our calculations were performed for LENA at Pyhäsalmi assuming a depth of 3,960 m.w.e. and a corresponding muon flux of $(1.1 \pm 0.1) \times 10^{-4}/\mathrm{m}^2\mathrm{s}$ [128].

^{9}Li in-situ production

As the β endpoint of ^{9}Li is at 13.6 MeV, it will affect the DSNB detection only in the lower energy region of the observational window. For a rough estimate of the expected event rate, one can adopt the value derived for KamLAND: 0.6 events in 0.28 kton-years exposure for $E > 9.5$ MeV [123]. Scaling the mass to 44 kton-years fiducial volume in LENA, including a reduction of the integral muon flux by a factor of ~ 9 in Pyhäsalmi [129] and considering the dependence of the production rate on the muon energy ($\propto E_\mu^{0.75}$) [130], the resulting rate is approximately 20 events per year.

However, as the muon passes through the fiducial volume, it can be clearly identified and a time as well as a volume cut can be applied. The ^{9}Li nucleus cannot travel far, as its half-life is $T_{1/2} = 0.18\,s$. Therefore, excluding a cylindrical volume of 2 m around each muon's path for 1 second ($\sim 5 \times T_{1/2}$) decreases the background sufficiently. As the fiducial volume is hit by a muon about every 5 s, one loses about $\sim 0.2\,\%$ of exposure time.

Fast Neutrons

Whereas muon tracks in the inner detector or in the muon veto can be clearly identified, muons passing the surrounding rock generate a background of fast neutrons. Usually, such a neutron will be accompanied by a number of charged particles that can be identified in the veto. However, there is a certain probability that the neutron will pass into the inner detector unnoticed. The neutron deposits its remaining kinetic energy in the scintillator and thereafter is captured by a proton, mimicking a real $\bar{\nu}_e$ event.

Using the estimates by Kudryavtsev *et al.* [129] for neutron production at 4,000 m.w.e. and assuming a mean absorption length of 0.75 m [129], one obtains a rate of about 10^5 neutrons per year entering the muon veto. However, if one assumes a more realistic energy spectrum at the boundary between rock and cavern [129], simulations performed with Geant4 [131] show that only ~ 7 neutrons per year will reach the fiducial volume and only 0.5 per year will generate a signal in the relevant energy region from 10 to 25 MeV. As mentioned before, this number will be further decreased by the detection of accompanying shower particles in the muon veto and is therefore a conservative value.

4.3 Predictions for a future DSNB detection

After the discussion of the DSNB spectra and the background to the detection in the previous section, we come now to a discussion of possible future DSNB measurements and the information content of such a measurement. Presently, the best experimental limit on the anti-neutrino component of the DSNB flux has been obtained by Super-Kamiokande as [22]

$$\Phi_{\bar{\nu}_e} \leq 1.2\,\mathrm{cm}^{-2}\,\mathrm{sec}^{-1}\ (\mathrm{E}_{\bar{\nu}_e} > 19.3\,\mathrm{MeV}). \tag{4.13}$$

Below 19.3 MeV the backgrounds in Super-Kamiokande are too high. As we have seen in Sec. 4.2, LENA can measure DSNB neutrinos down to about 10 MeV.

In the following, we are interested in the information that can be gained from a DSNB measurement. In the literature statements can be found that with a future measurement of the DSNB one could gain significant information on the parameters for star formation and SN explosions. It often seems that these claims are not well founded or rely on high event rates or an extremely precise prior knowledge of certain input parameters. Therefore, we will analyze in detail in the following section what we can learn from the DSNB spectrum with respect to SN parameters and star formation parameters, assuming realistic event rates as could be obtained in LENA or GLACIER. To that end, we perform an error forecast for a possible measurement of the DSNB spectrum of neutrinos and anti-neutrinos.

First, we introduce our model and assumptions before we come to a discussion of the statistical method used and the prospects for the determination of the DSNB parameters from a measurement of the spectrum of neutrinos and anti-neutrinos.

4.3.1 Baseline model

As discussed previously, the DSNB flux can be described with Eq. (4.1). We first define a baseline spectrum with typical values for the parameters according to our discussion in Sec. 4.1.1 and Sec. 4.1.2. For the star formation history the present best-fit values and the corresponding $1\,\sigma$ uncertainties obtained by GALEX are $\alpha = 0.5 \pm 0.4$ and $\beta = 2.5 \pm 0.7$ [112]. We therefore choose $\alpha = 0.5$ and $\beta = 2.5$ as our baseline values.

According to our discussion in Sec. 4.1.2, the local SN rate R_0 ranges between 0.4–2.6 $\times\, 10^{-4}\,\mathrm{yr}^{-1}\,\mathrm{Mpc}^{-3}$ [107], where several authors find a preference for the higher values [114, 132]. Therefore we chose $R_0 = 2.0 \times 10^{-4}\,\mathrm{yr}^{-1}\,\mathrm{Mpc}^{-3}$ for our baseline model.

According to simulations the pinching parameter a can take on values between 2 and 5 [96]. However, most values seem to be in the middle range. Thus, we assume here only a slightly pinched spectrum with $a = 3$ as our baseline value. Moreover, the simulations of [96] refer to the instantaneous spectrum. Naturally, the time-integrated spectrum should be less pinched.

As discussed in Sec. 4.1.1 the usual binding energy is 3×10^{53} erg, which is distributed among the 6 types of neutrinos and anti-neutrinos. Therefore we assume now a total energy emitted in each flavor of $E_{\mathrm{tot}} = 5 \times 10^{52}$ erg.

Considering the mean energy of neutrinos and anti-neutrinos we use the results of simulations displayed in Eq. (4.4) as a guideline. Moreover, taking into account the less pronounced hierarchies between the flavors found in Ref. [21], we choose $\langle E_{\nu_e} \rangle = 18\,\mathrm{MeV}$, where we consider a moderate oscillation of ν_x to ν_e. This choice also guarantees that we are on the conservative

side for the expected fluxes, as previously there have been analysis that assumed much higher mean ν_e energies [35]. Considering the weaker influence of oscillations on the anti-neutrino energy, we assume $\langle E_{\bar{\nu}_e} \rangle = 15\,\mathrm{MeV}$.

In Tab. 4.4 we display our adopted baseline values. Note that the parameters R_0 and E_{tot} are degenerate and cannot be determined separately. Therefore we will always consider one combined parameter $E_{\mathrm{tot}} \times R_0$ in the following.

Table 4.4: Chosen baseline values of the SN and star formation parameters and the ranges, in which the parameters are allowed to vary in our analysis.

parameter	baseline value	assumed range
α	0.5	± 0.8
β	2.5	± 1.4
R_0	$2.0 \times 10^{-4}\,\mathrm{yr}^{-1}\,\mathrm{Mpc}^{-3}$	$0.4\text{–}2.6 \times 10^{-4}\,\mathrm{yr}^{-1}\,\mathrm{Mpc}^{-3}$
E_{tot}	50×10^{51} erg	$30\text{–}100 \times 10^{51}$ erg
$\langle E \rangle_{\bar{\nu}_e}$	15 MeV	free
$\langle E \rangle_{\nu_e}$	18 MeV	free
a	3	2–5

In a LENA-type detector with 50 ktons of liquid scintillator we would expect about 50 events in 10 yrs from our baseline model, where we have used the cross section of Eq. (2.5) with 2.5×10^{33} protons. Correspondingly, in a 100 kton liquid argon experiment like GLACIER we would also expect close to 50 events in 10 yrs, where we use the cross section given in Fig. 1.7 from Ref. [35]. Note, that our baseline values for the anti-neutrino spectrum give a flux of 0.6 $\mathrm{cm}^{-2}\,\mathrm{sec}^{-1}$ above 19.3 MeV, which is half the Super-Kamiokande limit.

4.3.2 Sensitivity forecast for a future DSNB measurement

To study the sensitivity of future experiments to the DSNB spectrum we implement a procedure that has previously been used by the GLoBES team [7, 8, 133] in the context of long baseline neutrino oscillation experiments. In this procedure some input parameters are assumed to be the true values, for which now predictions for the observables in a given experiment are made without statistical fluctuations. These predictions are used as "data" and a statistical analysis of these data is performed in order to see how well the input parameters can be reconstructed. With this procedure one can assess

the performance of an "average" experiment. The interpretation of these error forecasts is subtle. According to Refs. [134, 135] a real measurement can substantially deviate from these predictions. However, also according to Ref. [135], the probability to achieve a predicted $2\,\sigma$ sensitivity is usually better than 50%.

In the following we apply this method to our problem and conduct an error forecast for a possible DSNB measurement. In our case we assume the baseline DSNB parameters as our input and the energy dependent event rates as our "data". Subsequently we conduct a χ^2 analysis of our "data" and obtain predictions and confidence intervals for possible real measurements.

For a simultaneous ν and $\bar{\nu}_e$ observation, our χ^2 function is here defined as (see also appendix A)

$$\chi^2 = \sum_{i=1}^{N_{\mathrm{bin},\nu}} \frac{[T_{\nu,i} - O_{\nu,i}]^2}{T_{\nu,i}} + \sum_{i=1}^{N_{\mathrm{bin},\bar{\nu}}} \frac{[T_{\bar{\nu},i} - O_{\bar{\nu},i}]^2}{T_{\bar{\nu},i}} + \chi^2_{\mathrm{pull}}, \tag{4.14}$$

with $N_{\mathrm{bin},\nu}$ the number of neutrino energy bins and $N_{\mathrm{bin},\bar{\nu}}$ the number of anti-neutrino energy bins. $O_{\nu,i}$ and $O_{\bar{\nu},i}$ are our observed "data", according to our baseline values of Tab. 4.4. $T_{\nu,i}$ and $T_{\bar{\nu},i}$ are the "theoretically" expected events per bin for modified parameters that are to be tested. They are calculated according to Eq. (4.1).

In Eq. (4.14) we can include the best-fit values and uncertainties of the parameters that have been obtained independently in external experiments with so called pull-terms

$$\chi^2_{\mathrm{pull}} = \sum_{i=1}^{N} \frac{(\lambda_i - \lambda_{\mathrm{best,i}})^2}{\sigma^2_{\lambda,i}}\,, \tag{4.15}$$

where λ_i represents the N different parameters of our fit, where external information is available, $\lambda_{\mathrm{best,i}}$ their best-fit values and σ_λ their $1\,\sigma$ uncertainty.

We assume that our data are divided in bins with a width of 4 MeV. We have chosen this number as a compromise, as on the one hand we want to obtain information on the shape of the spectrum and cannot choose our bins too wide and on the other hand we have to consider that we need to have a not too small number of events per bin. For our analysis method the binning is actually not of importance, as we are free of statistical fluctuations, but we choose this approach as data binning is a common approach in experimental physics. Moreover, binning would allow the introduction of experiment specific systematical uncertainties such as energy resolution or unknown backgrounds. In our analysis we do not consider this, as the energy resolutions of LENA and GLACIER are very good and are a subdominant

contribution to the overall statistical errors. At 10 MeV LENA has an energy resolution of about 3%, which improves with rising energy [73]. The energy resolution of GLACIER is expected to be even better [73]. For a discussion of possible backgrounds to the DSNB measurement we refer to Sec. 4.2.

Of course, when minimizing our χ^2 function, Eq. (4.14), we always obtain exactly zero at the input parameters. In order to calculate a confidence interval for a specific parameter, one has to set Eq. (4.14) equal to the tabulated value corresponding to the desired confidence interval and minimize the resulting function with respect to all other parameters, which leaves us with only one degree of freedom. For example, according to the χ^2 table (see appendix A) we have $\chi^2 = 3.84$ at 95% c.l.

Our pull terms encompass the two star formation parameters α and β and their quoted $1\,\sigma$ uncertainties. As we do not have independent measurements with a given uncertainty on all parameters, we take into account theoretical considerations, as well as upper and lower plausible limits on parameters, which we have introduced in the previous sections and which we show in Tab. 4.4. $\langle E \rangle_{\bar{\nu}_e}$ and $\langle E \rangle_{\nu_e}$ are allowed to vary freely.

Concerning the total energy $E_{\rm tot}$ released in a specific neutrino flavor precise predictions for the binding energy are presently not possible due to the unknown equation of state and the dependence on the progenitor mass. For example 84 $\times 10^{51}$ erg have been obtained as a best-fit in a statistical analysis of the SN 1987A data by Refs. [136, 137]. Therefore, we adopt a rather generous range between 30–100$\times 10^{51}$ erg for an individual flavor. That means that the combined parameter $E_{\rm tot} \times R_0$ can vary in the range of 0.12–2.6 in units of the baseline values (see Tab. 4.4).

Possible backgrounds for the measurement of the anti-neutrino spectrum are reactor neutrinos, which set a lower limit to the detection window of 8–10 MeV depending on the detector site, as reactor neutrino energies extend to about 10 MeV. Above 26–30 MeV one expects significant influence from atmospheric neutrinos as discussed in Sec. 4.2. For neutrinos the lower energy limit is set by a background of solar neutrinos at about 18 MeV [35]. The authors of Ref. [35] find that above 40 MeV again the influence of atmospheric neutrinos is to be expected. However, in their work, they have chosen a mean neutrino energy that is higher than in this thesis, which naturally raises their expected neutrino flux and increases their energy window. Nevertheless, we choose a maximal detectable DSNB energy of 38 MeV. Though the uncertainty of the atmospheric neutrino flux is about 30% [35], this energy cut is likely on the optimistic side, at least for our baseline model. The reason for this assumption is that we want to invesigate if the extension to higher energies delivers more information about the shape and mean energy of the DSNB spectrum.

In summary, we choose a conservative energy range for our anti-neutrino events between 10 and 26 MeV and for the neutrino events between 18 and 38 MeV. Within these energy ranges we want to analyze three different cases, namely only anti-neutrino events, only neutrino events and a combined analysis of a measurement of both neutrinos and anti-neutrinos.

Note that in the following analysis we will not restrict ourselves to the setup and detector volume of a specific experiment. We will rather normalize each result to a specific event number, in our case chosen to be 50, 100 and 500 within our chosen energy windows. For our baseline values, this would correspond to approximately 10, 20 and 100 yrs of measuring time in both LENA and GLACIER.

After this general discussion of the analysis method and our model we come now to our results. Because of the pull-terms for α and β, these parameters are naturally constrained and indeed we find that we cannot improve on the GALEX results with our analysis. Therefore these parameters will have to be determined to a better precision with further experiments like the GALEX search. Our simulation confirms that we cannot gain constraints on a. We find that the minimal χ^2 for a is always < 1 even with 500 events. Concludingly, we omit a further discussion of a.

Because of the degeneracy of the parameters $E_{\rm tot}$ and R_0 it is of course impossible to gather any information on the total energy output of a SN. However, we do find some constraints on the combined parameter set. Analyzing the anti-neutrino spectrum with 100 events we find a minimal value of $E_{\rm tot} \times R_0 = 0.5$ and a maximal value of $E_{\rm tot} \times R_0 = 2.2$ in units of the baseline value at 95% c.l., which does constrain the input parameters slightly. Repeating the analysis for 100 neutrino events we find a lower limit of $E_{\rm tot} \times R_0 = 0.4$ in units of the baseline value (95% c.l.). An upper limit cannot be obtained in this case. With 500 anti-neutrino events we obtain a lower limit of 0.6 an upper limit of 1.8 in units of the baseline values. Naively, one would expect that the combined parameter set $E_{\rm tot} \times R_0$ is directly linked to the event rate and one should be able to obtain a better limit. However, we have noticed in our simulations that the influence of the β-parameter is equally important for the total flux and that even slight changes in β within its $2\,\sigma$ range can compensate changes of $E_{\rm tot} \times R_0$. Of course, as we have many parameters, correlations are to be expected.

In the following we concentrate on the error forecasts for the mean energy of neutrinos and anti-neutrinos. We display our results in Tab. 4.5. Shown are the expected upper and lower limits for $\langle E \rangle$ in MeV at 95% c.l. for 50, 100 and 500 assumed detected events. For 50 events we obtain errors of approximately $+50\%$ and -30% at 95% c.l. for both neutrino and anti-neutrino detector. This asymmetry is due to the choice of our baseline value for $E_{\rm tot} \times R_0$, which

Table 4.5: Upper and lower limits for the mean neutrino energy at emission in MeV at 95% c.l. Shown are the results for an analysis of only neutrinos, only anti-neutrinos and a combined analysis of both species. The event numbers are 50, 100 and 500 for each neutrino species. The "best-fit" mean neutrino energies are $\langle E \rangle_{\bar{\nu}_e} = 15$ MeV and $\langle E \rangle_{\nu_e} = 18$ MeV.

number	$\bar{\nu}_e$		ν_e		$\bar{\nu}_e + \nu_e$			
of	$\langle E \rangle_{\bar{\nu}_e}$		$\langle E \rangle_{\nu_e}$		$\langle E \rangle_{\bar{\nu}_e}$		$\langle E \rangle_{\nu_e}$	
events	min	max	min	max	min	max	min	max
50	10	23	13	27	11	23	14	25
100	11	21	13	26	12	21	15	24
500	12	19	14	23	13	18	15	21

is closer to the lower limit of the combined parameter set. This means that in the determination of the 95% significance level of the mean energy the allowed ranges of the other parameters are fully exhausted. For 100 events we obtain almost the same results, however, we get slightly better results for the upper boundary and in the case of anti-neutrinos also for the lower boundary. Only for 500 events we have errors of about +30% and −20% at 95% c.l. We emphasize that due to numerical exit conditions and round-off effects we expect an additional general uncertainty of the results of 1–2 MeV. Generally, our results are within the Super-Kamiokande allowed limit above 19.3 MeV.

For a combined analysis of neutrino and anti-neutrino events we also do not see a significant improvement within our expected numerical errors. There is a slight tendency for improvement, which could be attributed to the overlapping of two energy bins of neutrinos and anti-neutrinos. We find for example with 50 events of each neutrino species errors of +50% and −20% for anti-neutrinos and +40% and −20% for neutrinos (at 95% c.l.). However, we conclude that a combined analysis is not of considerable advantage for a measurement of the mean neutrino energy. Of course, if there was an established connection between the energy ratio of neutrinos and anti-neutrinos (e.g. via observation of a close galactic supernova and the determination of the mean neutrino and anti-neutrino energies), a combined analysis would be of advantage, in that the total number of registered events would be doubled and neutrino and anti-neutrino energies would not have to be treated as independent parameters any more.

As a cross-check we fix now $a = 3$ and do not allow this parameter to

vary. This is also motivated by the consideration that the time-integrated neutrino spectrum is less pinched than the instantaneous spectrum and thus low values of a could be more likely. The results of this analysis are displayed in Tab. 4.6. Generally we obtain sensitivities that are better by roughly 2–3 MeV. Hereby the upper and lower limit of the combined parameter $E_{\mathrm{tot}} \times R_0$ in Tab. 4.4 is not reached, which would be one of the causes of asymmetric confidence intervals as noted previously for free a. This confirms also our previous statement that a cannot be determined, i.e. the χ^2 function for a is very flat and does not have a pronounced minimum. Of course in this case we also obtain better limits for $E_{\mathrm{tot}} \times R_0$. Thus for 100 anti-neutrino events we obtain a lower limit of $E_{\mathrm{tot}} \times R_0 = 0.6$ and an upper limit of 1.8 in units of the baseline values at 95% c.l. To give a rough empirical tendency one can say that with fixed a 100 events are enough to obtain the same intervals as for 500 events, when a is allowed to vary between 2 and 5.

Table 4.6: Same as Tab. 4.5 but with the spectral supernova pinching fixed to $a = 3$. The confidence intervals improve by about 2–3 MeV.

	$\bar{\nu}_e$		ν_e		$\bar{\nu}_e + \nu_e$			
	$\langle E \rangle_{\bar{\nu}_e}$		$\langle E \rangle_{\nu_e}$		$\langle E \rangle_{\bar{\nu}_e}$		$\langle E \rangle_{\nu_e}$	
events	min	max	min	max	min	max	min	max
50	12	21	15	25	12	20	16	22
100	13	19	15	22	13	18	16	21
500	14	17	17	20	14	17	17	19

Let us assume for now that a supernova has occurred in our galaxy and that the total energy, mean neutrino energy and spectral pinching have been measured precisely and take on the values of our chosen baseline. This of course requires also the assumption that all SN are governed by the same mechanism and render the same neutrino spectrum. Now we can analyze the DSNB spectrum in the same way as before, but with only three unknown star formation parameters α, β and R_0. For this analysis we also drop the pull terms on α and β as we investigate, if we can get new information from the DSNB without additional measurements. However, we find that with 100 anti-neutrino events the 95% c.l. results for α and β are worse than even the $3\,\sigma$ limits obtained by GALEX. Moreover, we find that R_0 ranges between $(0.5\text{–}4.8) \times 10^{-4}\,\mathrm{yr}^{-1}\,\mathrm{Mpc}^{-3}$ at 95% c.l.. This leads us to the conclusion that the star formation parameters cannot be constrained significantly by the DSNB even with known SN parameters.

In summary we see that the mean neutrino energy at emission can be constrained without assuming precise information on the parameters. However, these constraints are not conclusive for a reasonable event number of 50–100. Moreover, the other SN parameters E_{tot} and a cannot be constrained. Additionally, as we have already discussed E_{tot} and R_0 are degenerate so one parameter can only be determined with a precise information on the other and also the combined set remains very uncertain.

Therefore we conclude that a reduction of the number of parameters is reasonable, as most of the parameters remain undetermined. We analyze in the following our assumed baseline "data" set with a different fit equation that has only three parameters, where we follow the approach in Ref. [138].

4.3.3 Analytical fit to the DSNB spectrum

As we have discussed in the previous section, the only meaningful quantity that can be determined from the DSNB spectra is the mean energy of the SN neutrino spectrum. As the DSNB flux is just the red-shifted superposition of the energy spectra of numerous supernovae, it makes sense to try to fit the presently measurable DSNB spectrum with a spectrum similar to the one of an individual SN according to Eq. (4.5) as

$$\Phi(E) = \frac{\mathcal{F}}{\mathcal{E}(\mathcal{A}+1)^{(-\mathcal{A}-1)}\Gamma(\mathcal{A}+1)} \left(\frac{E}{\mathcal{E}}\right)^{\mathcal{A}} \exp\left[-(\mathcal{A}+1)\frac{E}{\mathcal{E}}\right] \tag{4.16}$$

where $\mathcal{F}$ is the total neutrino flux at the detector location, $\mathcal{E}$ the mean energy and $\mathcal{A}$ the spectral pinching [96]. The spectrum returns the mean DSNB neutrino energy at the detector location. The fit function, Eq. (4.16), describes the actual spectrum, Eq. (4.5), very well between 8 and 40 MeV. In contrast to the analysis in Ref. [138] we express the fit parameters by the input parameters of star formation and supernovae and conduct an error forecast along the lines of our analysis in the previous section. We compare the results obtained with the analytical fit with the results of our error forecast in the previous section.

We perform a χ^2 analysis and fit Eq. (4.16) to the "data" obtained with our baseline DSNB spectrum for anti-neutrinos according to Tab. 4.4. For simplification we only consider the anti-neutrino spectrum between 10 and 26 MeV and drop the discussion of the neutrino spectrum. Moreover, we invoke the anti-neutrino cross-section according to Eq. (2.5).

First let us discuss qualitatively with the help of Eq. (4.5), how $\mathcal{A}$, $\mathcal{F}$ and $\mathcal{E}$ are influenced, when one of the DSNB parameters is varied, whereas the others are held at a fixed value. Note that for the rest of this section we

drop the $\bar{\nu}_e$ index, as we only deal with anti-neutrinos. It can be seen that an increasing early and late star formation rate α and β increases $\mathcal{F}$, but lowers $\mathcal{E}$, as we have now a higher contribution of red-shifted neutrinos. However, we expect the changes in $\mathcal{F}$ to be stronger for varied β, as the late star formation history has a stronger influence in the power law describing the $R_{\rm SN}$ in Eq. (4.10). The degenerate parameters $E_{\rm tot} \times R_0$ should not influence $\mathcal{E}$ or $\mathcal{A}$ much, as this gives just an overall flux normalization. Therefore, we expect $\mathcal{F}$ to linearly increase with increasing $E_{\rm tot} \times R_0$. An increasing spectral pinching a should increase $\mathcal{A}$ linearly. Increasing the mean neutrino energy $\langle E \rangle$ should lower $\mathcal{F}$, as for equal total energy less neutrinos are released. Naturally, $\mathcal{E}$ should rise linearly with $\langle E \rangle$, whereas the influence on $\mathcal{A}$ should be weak. Indeed, we find that these qualitative considerations hold in our χ^2 analysis.

For the fit of Eq. (4.16) to our baseline DSNB spectrum, we choose a binwidth of only 0.5 MeV, as we want to investigate how well this fit reproduces our input spectrum. However, as noted above, the binwidth is not the crucial point of the analysis. We conduct the fit with 100 anti-neutrino events. The best-fit values and corresponding upper and lower limits are $\mathcal{F} = 29^{+34}_{-16}\,\mathrm{cm}^{-2}\,\mathrm{sec}^{-1}$, $\mathcal{E} = 5^{+3}_{-1}$MeV and $\mathcal{A} = 0.25^{+0.75}_{-0.25}$ at 95% c.l. Also in this analysis the mean energy $\mathcal{E}$ seems to be the only quantity to be determined well confirming our results from the previous section. The spectral pinching and the flux show considerable uncertainties. This is due to correlation effects of the DSNB parameters and we will look into this in more detail in the following.

We illustrate the dependence of $\mathcal{F}$ on α, β, $\langle E \rangle$ and $E_{\rm tot} \times R_0$ in Fig. 4.3 and the dependence of $\mathcal{E}$ on these parameters in Fig. 4.4. Shown are the best-fit values of $\mathcal{F}$ and $\mathcal{E}$ obtained by a χ^2 fit. Note that for the sake of illustration we have held the parameters that are not shown at their baseline values. We do not show the dependence of $\mathcal{A}$ on the parameters, as the strongest influence of $\mathcal{A}$ is, as expected, on a. The dependence on α, β, $\langle E \rangle$ and $E_{\rm tot} \times R_0$ is only weak. We find that $\mathcal{A}$ depends linearly on a according to

$$\mathcal{A} \approx 0.31a - 0.42. \tag{4.17}$$

We conclude again that $\mathcal{A}$ is the least promising parameter to constrain and we omit it in the following. We rather concentrate on $\mathcal{F}$ and $\mathcal{E}$. Both $\mathcal{E}$ and $\mathcal{F}$ depend only weakly on a as confirmed by our simulations. Therefore we also neglect a further discussion of this parameter.

Let us first turn to a discussion of $\mathcal{F}$. We see from Fig. 4.3 that $\mathcal{F}$ is strongly dependent on β and $E_{\rm tot} \times R_0$, and more weakly on α and $\langle E \rangle$. This means that an increase in $E_{\rm tot} \times R_0$ can be compensated by a decrease in β

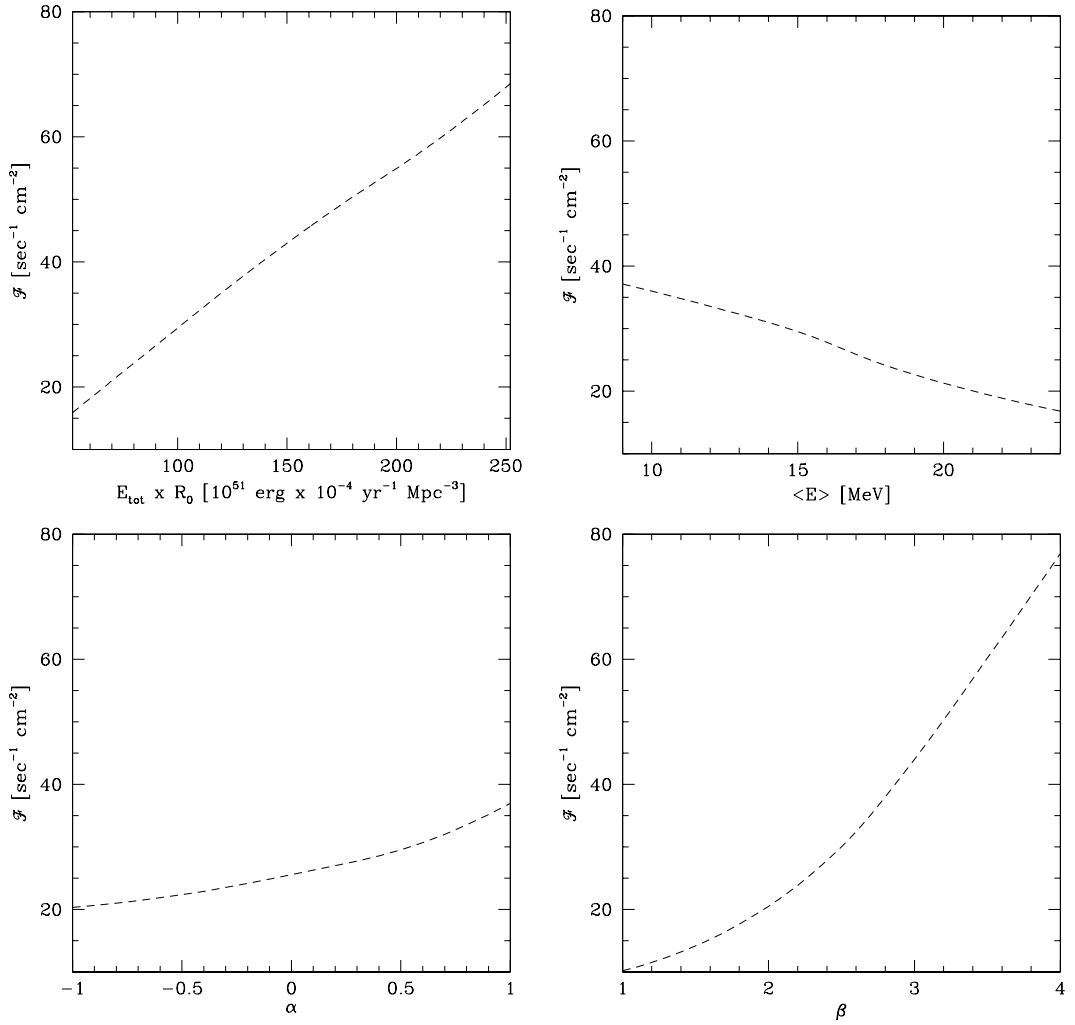

Figure 4.3: Dependence of $\mathcal{F}$ on the parameters α, β, $\langle E \rangle$ and $E_{\rm tot} \times R_0$. The parameters that are not shown are held at their baseline values. $\mathcal{F}$ is influenced equally strong by $E_{\rm tot} \times R_0$ and β. The dependence on α and $\langle E \rangle$ is much weaker and anti-correlated.

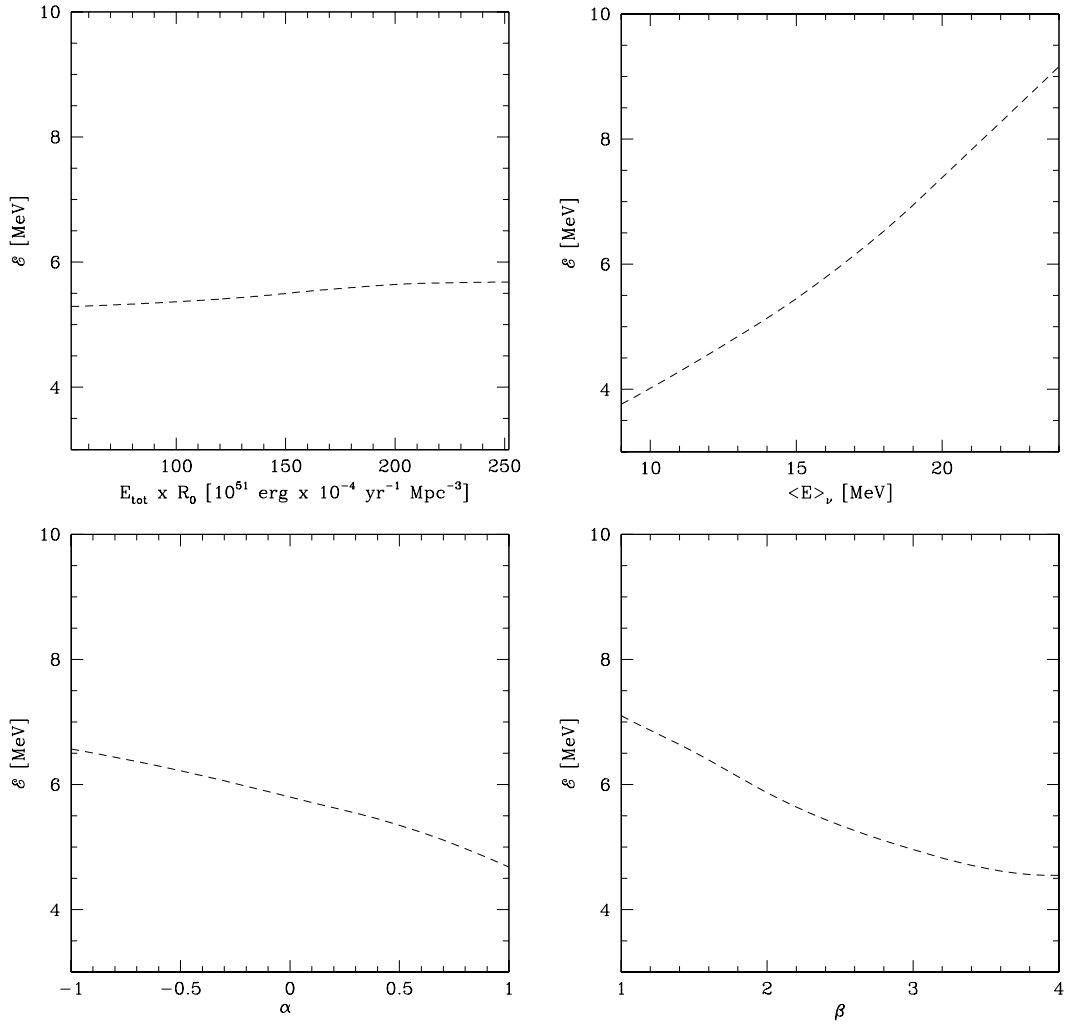

Figure 4.4: Same as Fig. 4.3 but for $\mathcal{E}$. $\mathcal{E}$ depends strongest and linearly on $\langle E \rangle$. The dependence on α and β is weak and $E \times R_0$ does not have any influence.

or an increase in $\langle E \rangle$. An approximative quantitative behavior of $\mathcal{F}$ can be expressed by

$$\begin{aligned}
\frac{\mathcal{F}}{\mathrm{cm}^2\,\mathrm{sec}} &\approx 0.26\,\frac{(E_{\mathrm{tot}} \times R_0)}{10^{51}\mathrm{erg}\cdot 10^{-4}\,\mathrm{yr}^{-1}\,\mathrm{Mpc}} \\
\frac{\mathcal{F}}{\mathrm{cm}^2\,\mathrm{sec}} &\approx \beta(6\beta - 7.5) \\
\frac{\mathcal{F}}{\mathrm{cm}^2\,\mathrm{sec}} &\approx 1.4\,\frac{\langle E \rangle}{\mathrm{MeV}} \\
\frac{\mathcal{F}}{\mathrm{cm}^2\,\mathrm{sec}} &\approx \alpha(3.1\alpha + 7.8)\,. \qquad (4.18)
\end{aligned}$$

We thus conclude that a determination of one of the parameters by a measurement of $\mathcal{F}$ is not possible, as there is no clear dominance of one of the parameters in the quantity $\mathcal{F}$.

Turning to the $\mathcal{E}$ parameter we see that $\mathcal{E}$ is basically independent of $E_{\mathrm{tot}} \times R_0$ and only weakly dependent on α and β. The strongest almost linear dependence is on $\langle E \rangle$. A quantitative behavior can be expressed by

$$\begin{aligned}
\frac{\mathcal{E}}{\mathrm{MeV}} &\approx \alpha(-0.18\alpha - 0.91) \\
\frac{\mathcal{E}}{\mathrm{MeV}} &\approx \beta(0.21\beta - 1.9) \\
\frac{\mathcal{E}}{\mathrm{MeV}} &\approx 0.36\,\frac{\langle E \rangle}{\mathrm{MeV}}\,. \qquad (4.19)
\end{aligned}$$

The behavior of $\mathcal{E}$ is still governed by β and $\langle E \rangle$, but we see that the contribution from $\langle E \rangle$ dominates. Thus from a measurement of $\mathcal{E}$ information on the mean neutrino energy $\langle E \rangle$ of a SN explosion can be obtained. Considering the best-fit and the 95% c.l. limit quoted above for our baseline case, $\mathcal{E} = 5^{+3}_{-1}\,\mathrm{MeV}$, we can get an approximate 95% c.l. limit on the mean energy when applying Eq. (4.19) as $\langle E \rangle = 15^{+8}_{-3}$ MeV, which is rather well matched with our result from the previous section of $\langle E \rangle = 15^{+6}_{-4}$ MeV within numerical uncertainties.

4.4 Summary of chapter 4

We have discussed diffuse SN neutrinos and conducted an error forecast for a possible future measurement with future experiments like LENA or GLACIER. To that end we have defined a set of baseline parameters, which delivered event rates that we defined as "data". This data was analyzed with a χ^2 analysis on the basis of a model with modified parameters allowing us to

determine confidence regions for those parameters. The interpretation of the results is subtle as our data is per definition free of statistical fluctuations. However, with this method one can obtain an estimate for the sensitivity of a future experimental project.

We find that the only parameter that can be extracted to a reasonable precision is the mean neutrino energy of an individual SN. Information on parameters, such as the star formation history or the spectral pinching of the SN neutrino energy spectrum, can not be obtained. Additionally, the information on the local SN rate and the total energy output of supernovae is limited. Though it seems likely that the DSNB is within close reach of detection, we conclude that with reasonable event numbers of 50–100 events in 10 years for LENA or GLACIER no information on the star formation parameters and the parameters of an individual supernova can be gained. We find that the mean neutrino energy can be determined with 50 events to within a $2\,\sigma$ uncertainty of $+50\%$ and -30% or $\langle E \rangle = 15^{+8}_{-5}\,\mathrm{MeV}$ for anti-neutrinos. With a hypothetical event number of 500 events we expect a sensitivity to $+30\%$ and -20% at 95% c.l., which for our assumed values means $\langle E \rangle = 15^{+4}_{-3}\,\mathrm{MeV}$ for anti-neutrinos. We have checked that not even with a precise information on the SN parameters additional strong constraints on the star formation parameters can be set. Moreover, we have conducted a combined analysis of neutrino and anti-neutrino data in order to cover a larger energy range. However, we conclude that this does not deliver significant new information.

However, based on the assumption that the time-integrated spectrum of a supernova is less pinched and similar to a thermal Boltzmann spectrum, we have held the pinching parameter at $a = 3$, which improves our limits by about 2–3 MeV.

As a consequence of the limited information that can be obtained on most of the parameters, we have conducted an analytical fit to to the local DSNB spectrum that can be measured in an anti-neutrino detector. As a fit function we have chosen a spectrum similar to the one of an individual SN, as the measured spectrum is just the red-shifted sum over many supernovae, which reduces our parameter set to three. Here again we find that the main information can be gained for the mean neutrino energy of the spectrum at the detector. We have quantified the influence of the DSNB parameters on our three fit parameters. The mean energy of the fit is linearly dependent on the mean neutrino energy of a SN and almost independent on the other DSNB parameters. We find that our best-fit result and the 95% c.l. limits for the mean neutrino energy correspond very well to the results obtained for our error forecast with the full parameter set.

Generally it can be said that a measurement of the DSNB is expected with the next generation of neutrino detectors. Such a measurement would

be a major discovery able to confirm our beliefs about supernovae and star formation. However, we expect that no new information can be gained on star formation parameters. However, the determination of the mean energy even at its $2\,\sigma$ confidence level would be helpful to rule out extreme models for supernovae.

Chapter 5

Conclusions

In this thesis we have studied neutrinos from diverse sources, namely geoneutrinos, reactor neutrinos and diffuse supernova neutrinos and the possibilities for a detection in future liquid scintillator detectors. For the first time, we have studied in detail novel applications for the directional sensitive measurement of neutrinos and have applied for the first time methods, previously only used in the context of neutrino oscillation experiments, to analyze the performance of future detectors in detecting diffuse neutrinos.

Concerning the geoneutrino detection the proposed LENA experiment with a mass of 50 kton of liquid scintillator would provide a high statistics measurement of the geoneutrino flux. On an oceanic detector site such as Hawaii about 300 events are to be expected per year, whereas on a continental site such as the Pyhäsalmi mine in Finland the reference rate would be about 1,000 per year.

As information on the Earth's interior can only be obtained in an indirect way and via model dependent conclusions, we set out to prove several geophysical models with LENA.

We have investigated the detection potential of LENA for a hypothetical georeactor. We find that LENA could be able to identify a 2 TW georeactor at a statistical level of $3\,\sigma$ after only one year of measurement.

As the distribution of radioactive isotopes in the Earth is unknown and as there are several models suggesting a large radioisotope content in the core, we have devoted the main part of our analysis to the directional sensitive measurements of neutrinos from strong geoneutrino sources in the core and in the mantle. The forward displacement of the neutron in the inverse beta decay reaction that is the main anti-neutrino detection channel could be used to get information about the neutrino's initial direction. We discussed the directional measurement for an unloaded PXE-based scintillator and a Gd-loaded scintillator, the two main concepts that are presently under discussion

for future experiments. Generally, we find that the Gd-loaded scintillator delivered better results, as more energy is released on a larger number of photons. While we obtain impressive single source resolution, we find that diffuse sources can hardly be resolved. Thereby, we have relied on conservative estimates of the light yields and generally assumed a value of 120 pe/MeV. Presently it seems as if light yields of 250 pe/MeV could be easily realized in LENA. On the basis of only the directional information an exposure of about 500 kton-year for an unloaded and 250 kton-year for a Gd-loaded scintillator would be required for a $1\,\sigma$ detection of the most extreme geophysical model with a maximum heat contribution from the core of 20 TW, accounting for half of the total heat output.

Moreover, we find that placing the detector on an oceanic site is not advantageous. Though one does not have the crustal backgrounds to a measurement of core and mantle, the event rates are significantly reduced and the differences between models with and without a strong source in the core are not as distinct as on a continental site. This is an important result in this context, as there are several plans for developing submarine-like detectors, which increases costs and environmental risks. Nevertheless, the fact remains that a detector on an oceanic site would deliver important results concerning the total fluxes and the elemental ratios of the radioisotopes complementary to a continental site experiment.

As there are several ongoing plans to build large-volume liquid scintillator detectors, it might well be the case that more than one 50 kton detector will be installed. Therefore only slight improvements in experimental detection methods could already lead to immediate applications of the techniques for directional measurement. Though we have omitted to explicitly include backgrounds, which should be considered in a realistic analysis, we have mostly made conservative assumptions on the detector performance. Thus, we have only considered events in the center of the detector. Therefore, in future works the exact location of the events should be included, which increases the light yield for events further away from the center. Moreover, for Gd-loaded scintillators we based our assumptions on the precision of the detection of the neutron capture point on the measurements of the CHOOZ experiment. CHOOZ, however, did not use the time information in reconstructing the events, which should lower the precision of the detection. As the precision of the neutron detection introduces the main uncertainty in the directional measurement, a usage of the time information in LENA could improve the situation further.

In summary, large-volume scintillator detectors of the next generation will be extremely useful to study the interior of the Earth in the “light of neutrinos”. The interest of neutrino physicists in geological matters has trig-

gered cooperation with geologists and a first major meeting bringing together experts of both areas has taken place on Hawaii in December 2005, where I also had the chance of presenting our results[1]. The activities in this field are ongoing and the community is eagerly awaiting the flux measurements of Borexino.

We have extended the study of the directional sensitive measurement of the anti-neutrino flux to reactor neutrino experiments that are currently designed to measure θ_{13} and have investigated for the first time the "neutrino imaging power" of the Double Chooz near detector that will register about 1.6×10^5 events per year. The Double Chooz experiment will be the first of this type and can therefore adequately prove the principles of our method.

For our assumptions on the near detector performance we have relied on the CHOOZ measurements. CHOOZ was able to locate a single core with a $1\,\sigma$ half-cone aperture of 18° with only 2,500 events. Considering only a single source the direction can be determined to a high precision with the Double Chooz near detector. We obtain an average neutrino direction with a $1\,\sigma$ half-cone aperture of 2.4° with one year of data.

The two reactor setup is far more challenging, as for small separation angles the sources can not be resolved. Thus, for Double Chooz with a 30° separation angle we find that the setup is ineffectual for a clear separation of the reactors. The reactors can be separated at the $3\,\sigma$ level after 5 years of measurement.

With increasing separation angle it becomes much easier to distinguish the reactors. For a setup with $\phi = 90°$, even 1.6×10^5 events would be enough to measure the separation angle to about $\pm 10°$ at $3\,\sigma$. Such a setup was intended for the Double Chooz near detector in early plans, which would have provided also about 10^6 events per year. Due to the larger separation angle a distinction of the two sources would have been straightforward.

As a future work and work in progress in collaboration with J. Kopp and M. Lindner, we plan to use the directional sensitive measurement of neutrinos to conduct a precision monitoring of a reactor core. To that end we envision several 1 m^3 scale detectors that are placed as close to the core as possible, considering the core's intrinsic neutron flux and the heat production. As these detectors are small, they could be easily designed to gain light yields larger than 800 pe/MeV. With this setup we intend to measure burn-out effects of the fuel rods and to precision monitor the neutrino flux and spectrum.

It has been recently made public[2] that a US group has actual plans to

[1]The proceedings of this conference are published in a special edition of Earth, Moon, Planets.

[2]AIP Physics News on Feb. 4th 2008; http://www.aip.org/png/2008/295.htm

install a 1 m^3 detector at a reactor core and use the directional information encoded in the neutrino flux. Thus the interest in the application of neutrino direction measurement has spread to a greater public.

As for the Double Chooz setup a precision monitoring of the cores is not possible, we can use the angular sensitivity to determine the two individual reactor strengths from the neutrino signal alone. The one-year integrated power of one of the reactors can be determined to $\pm 11\%$ at $1\,\sigma$, the five-year integrated value to $\pm 4.8\%$. For the more favorable setup with a separation angle of $\phi = 90^\circ$ and 10^6 events one obtains a monthly precision of 5.4%. This is worse than the expected 1.5% precision of conventional methods that operate continously and measure the neutron flux in the reactor. Nevertheless, our method can provide an independent measurement of the individual reactor strength.

Finally, we have discussed diffuse supernova neutrinos and conducted an error forecast for a possible future measurement with proposed experiments such as LENA or GLACIER. To that end we have defined a set of baseline parameters, which delivered event rates that we defined as "data". This data was analyzed with a χ^2 analysis, where we included available prior information on parameters from external experiments. The interpretation of the results is subtle as our data is per definition free of statistical fluctuations. However, with this method one can estimate the prospects of the performance of future experiments well and we have to our knowledge for the first time applied this technique outside its applications in forecasting the performance of neutrino oscillation experiments.

According to our extensive study of possible backgrounds to the DSNB detection in LENA, the main background below 10 MeV is due to anti-neutrinos from nuclear reactors. For LENA we have an energy window between 10 and 25 MeV, where we almost have a background free detection.

We generally have assumed realistic event numbers of 50–100 in 10 years in the relevant energy region. The parameters that enter the determination of the DSNB spectrum are the early and late star formation history and the local supernova rate as well as the total energy output, the mean neutrino energy and the spectral pinching of an individual supernova. We find that the only DSNB parameter that can be determined to a reasonable precision is the mean neutrino energy of supernovae, assuming that all supernovae are similar. For example, we find that the mean neutrino energy can be determined with 100 events to within a $2\,\sigma$ uncertainty as $\langle E \rangle = 15^{+6}_{-4}\,\mathrm{MeV}$ for anti-neutrinos. For 500 events we already expect $\langle E \rangle = 15^{+4}_{-3}\,\mathrm{MeV}$. Thus, a measurement of this parameter in future liquid scintillator detectors can be used to exclude extreme models in supernova physics.

As the energy window of the neutrino component could extend to higher

energies than in case of anti-neutrinos, we have conducted a combined analysis of neutrino and anti-neutrino events to investigate, if a larger spectral information could improve the situation significantly. However, we find that this is not the case even with optimistic assumption on the neutrino energy window. Nevertheless, an additional detection of the neutrino component would open up the possibility to draw conclusions on muon and tau neutrinos. Moreover, the situation changes, if there was a established and fixed ratio between the neutrino and anti-neutrino mean energies. However, simulations are contradictory on this issue and the results are subject to the magnitude of the neutrino mixing angles.

Furthermore, our results could be improved upon if the external measurements of the star formation parameters became more precise. We have also analyzed a situation, where the supernova parameters are perfectly known, e.g. via a detection of a galactic supernova. We find that no additional information can be gained on the star formation parameters.

As generally the parameter space entering the DSNB spectrum is large and obtaining information on a single parameter is often not possible, we conducted an analytic fit to the energy spectrum. The fit function has only three parameters and characterizes the spectrum that can be measured at the detector. We have chosen our fit function to have the shape of the neutrino energy spectrum of an individual supernova, as the DSNB is just the redshifted superposition of all past energy spectra of supernova events. The parameters entering the fit function, of course, have a different meaning than for a supernova spectrum, as here we have the mean diffuse neutrino energy and the flux at the detector as well as the spectral shape of DSNB.

We have investigated the behavior of the fit function and the relation of the fit parameters to the DSNB parameters, which we have expressed in analytic formulas. We again find that the mean neutrino energy at the detector, which we are able to translate to the mean energy at the source, is the only parameter that can be extracted to a good precision. Indeed, the results obtained with the analytic fit agree well with the results obtained with the full parameter set. For example, we find for the mean diffuse neutrino energy at the detector $\mathcal{E} = 5^{+3}_{-1}$ MeV for 100 events. With help of our analytic relations of the fit parameters to the DSNB parameters, we can translate this to $\langle E \rangle = 15^{+8}_{-3}$ MeV for the mean neutrino energy of an individual supernova.

Thus, we conclude that both our full analysis of the DSNB parameter set as well as the analysis with our fit function delivers comparable results. A measurement of the DSNB flux would be an exciting new detection and the LENA detector is suitable for this task in the energy window of about 10–26 MeV. An additional measurement of the mean neutrino energy can give important information for individual supernova events.

As a further step for the analysis of the diffuse neutrinos the inclusion of the background would be required. As there could be an uncertainty in the atmospheric neutrino flux as large as 30%, the energy window of the DSNB detection could be widened. Moreover, the energy window depends on the location of the detector. A LENA detector on Hawaii could start detecting the DSNB at about 8.5 MeV, due to the reduced reactor neutrino flux.

Furthermore, there is the possibility to not only detect anti-neutrinos with LENA, but also to detect neutrinos via capture on carbon. The event rates for this process are not very high, but it could serve to improve existing directly measured upper limits on the neutrino component by up to three orders of magnitude. A detailed analysis is planned in collaboration with A. Mirizzi.

In summary, it can be said that the future of neutrino physics holds exciting detections in store. Especially with large volume detectors it will become possible to increase statistics and draw information on diverse neutrino sources. We hope that in this new phase of neutrino physics the developments of this thesis will be put to a test and clear the way for new applications and measurements. We have gained the insight that thinking in new ways and investigating transdisciplinary areas can open up new possibilities that will keep the field alive for years to come.

Appendix A

Statistical methods

Throughout this thesis a number of statistical methods have been used. These methods shall be briefly introduced and summarized in the following. The most general distinction between statistical methods is whether they belong to frequentist or Bayesian statistics. In frequentist statistics one reports objectively the outcome of a result. In Bayesian statistics prior beliefs are incorporated. We exclusively deal with frequentist statistics in this work, and more precisely with the maximum likelihood method and the χ^2 analysis. The arguments closely follow the Particle Data Group review [139].

A.1 Maximum likelihood analysis

The maximum likelihood method is the most efficient method to obtain the best-fit parameter values of a given data set, as the data is used unbinned and thus no information is lost. However, this method requires the knowledge of the particle distribution function of the system. The maximum likelihood estimators, meaning the best-fit points of the parameters, are approximately unbiased for large data samples. For the maximum likelihood analysis we need to know the probability distribution function $f(x, \theta)$ of the system in order to construct the likelihood function

$$L(\theta) = \prod_{i=1}^{N} f(x_i, \theta). \tag{A.1}$$

Here x_i, $i = 1, \ldots, N$, is a set of independently measured quantities, whereas $\theta = (\theta_1, \ldots, \theta_n)$ is a set of n unknown parameters that we want to determine from the measurements. Thus the likelihood function $L(\theta)$ is the joint probability distribution function of the system and is a function of the parameters θ but evaluated with all data points.

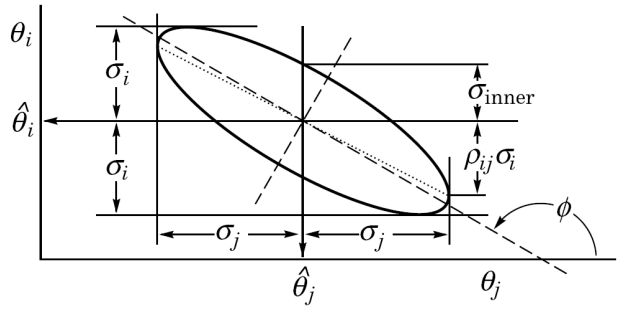

Figure A.1: Standard error ellipse. In this case the correlation is negative. Graphic taken from [139].

Usually not the likelihood function but the log-likelihood is maximized, as it is computationally easier to handle. The functions are maximized by the same values θ, as taking the log of a function is a continuous and monotonic operation. Thus one can find the maximum likelihood estimators by solving

$$\frac{\partial \ln L}{\partial \theta_j} = 0, \;\; j = 1, \ldots, n. \tag{A.2}$$

A way to determine the correlation of the parameters θ_i is the determination of the off-diagonal elements of the covariance matrix

$$V_{ij} = \langle (\theta_i - \mu_i)(\theta_j - \mu_j) \rangle \,, \tag{A.3}$$

where μ_i, μ_j are the means of θ_i and θ_j. In case of the maximum likelihood the elements of the inverse covariance matrix can also be determined as

$$(V^{-1})_{ij} = \frac{\partial^2 \ln L}{\partial \theta_i \partial \theta_j}. \tag{A.4}$$

Note that this can lead to an underestimation of the variances for finite samples. The correlation between parameters is defined as

$$\rho_{ij} = \frac{V_{ij}}{\sigma_i \sigma_j}, \tag{A.5}$$

where σ_i and σ_j are the standard deviations of θ_i and θ_j. Naturally the quantity ρ_{ij} takes on values between -1 and $+1$, thus a parameter correlates perfectly with itself, as $\rho_{ii} = 1$. There is no correlation between two parameters for $\rho_{ij} = 0$.

For large samples L takes on a Gaussian form and one can estimate the s-sigma standard deviation, being a contour line defined by the parameter values θ' by subtracting

$$\ln L(\theta') = \ln L_{\max} - \frac{s^2}{2}, \tag{A.6}$$

where $\ln L_{\max}$ is taken at the best-fit points of the parameters. For two parameters θ_i and θ_j, the tangents (parallel to the coordinate system axes) define σ_i and σ_j. The tilt angle of the major axis is given as

$$\tan 2\phi = \frac{-2\rho_{ij}\,\sigma_i\sigma_j}{\sigma_i^2 - \sigma_j^2}, \tag{A.7}$$

where ρ_{ij} is again the correlation coefficient. Thus parameters are uncorrelated, when the axes of the ellipse are parallel to the coordinate axes. The connection is displayed in Fig. A.1.

A.2 χ^2 analysis

The method of least squares or χ^2 analysis is analogous to the maximum likelihood method, if one has a set of independent measurements with observation O_i, that are Gaussian distributed around the mean μ_i with variance σ_i^2. In this case the set of parameters $\hat{\theta}$ that maximizes the Likelihood is the same that minimizes χ^2 and we have

$$\chi^2(\hat{\theta}) = -2\ln\hat{\theta} + \text{constant} = \sum_{i=1}^{N} \frac{(O_i - T_i)^2}{T_i}, \tag{A.8}$$

assuming that we have binned data and that we expect theoretically a certain number of events T_i in bin i. The method of least squares can be used to perform a goodness of fit test. After the measurement has taken place we find a number O_i of events in bin i. We treat the O_i's as independently distributed random variables. We can test our theoretical hypothesis now by calculating the χ^2 function. The values of this χ^2 are tabulated and give, dependent on the number of degrees of freedom (the number of independently distributed variables) the significance level for this hypothesis, meaning the probability that the hypothesis is true.

A more sophisticated χ^2 analysis includes prior information on parameters or detector performance, where systematic errors can be included. This can be done with the pull method, when adding so called pull terms χ_{pull} to the general χ^2. Implementing additional measurements and constraints on

parameters can be done in this way, if our expected event rate is dependent on multiple parameters. Assuming that some of our parameters are measured independently with best fit μ_i and one sigma uncertainty σ_{λ_i} we can write

$$\chi^2 = \sum_{i=1}^{N} \frac{(O_i - T_i(\lambda))^2}{T_i(\lambda)} + \sum_{j=1}^{k} \frac{(\lambda_j - \mu_j)^2}{\sigma_{\lambda_j}^2}, \tag{A.9}$$

where k is the number of parameters one has external information on. This function is then minimized over the parameters λ.

In the assumed application of the χ^2 method one has a data sample and tries to fit parameters to this data. However, to study the sensitivity of future experiments we introduce a procedure, which was to our knowledge first used by [7, 8, 133] in the context of long-baseline oscillation experiments. Here some input parameters are assumed to be the true values, for which now predictions for the observables in a given experiment are made without statistical fluctuations. These predictions are used as "data" and a statistical analysis of these data is performed in order to see how well the input parameters can be reconstructed. With this procedure one can estimate the performance of an "average" experiment.

The interpretation of these error forecasts is subtle. According to Refs. [134, 135] a real measurement can substantially deviate from these predictions. However, also according to Ref. [135], the probability to detect a predicted $2\,\sigma$ sensitivity is usually better than 50%, but also substantial deviations can occur. In order to obtain the desired confidence interval of a specific parameter one has to minimize the χ^2 function of the setup with respect to all other parameters, which leaves us with only one degree of freedom.

df	0.995	0.99	0.975	0.95	0.90	0.10	0.05	0.025	0.01	0.005
1	---	---	0.001	0.004	0.016	2.706	3.841	5.024	6.635	7.879
2	0.010	0.020	0.051	0.103	0.211	4.605	5.991	7.378	9.210	10.597
3	0.072	0.115	0.216	0.352	0.584	6.251	7.815	9.348	11.345	12.838
4	0.207	0.297	0.484	0.711	1.064	7.779	9.488	11.143	13.277	14.860
5	0.412	0.554	0.831	1.145	1.610	9.236	11.070	12.833	15.086	16.750
6	0.676	0.872	1.237	1.635	2.204	10.645	12.592	14.449	16.812	18.548
7	0.989	1.239	1.690	2.167	2.833	12.017	14.067	16.013	18.475	20.278
8	1.344	1.646	2.180	2.733	3.490	13.362	15.507	17.535	20.090	21.955
9	1.735	2.088	2.700	3.325	4.168	14.684	16.919	19.023	21.666	23.589
10	2.156	2.558	3.247	3.940	4.865	15.987	18.307	20.483	23.209	25.188
11	2.603	3.053	3.816	4.575	5.578	17.275	19.675	21.920	24.725	26.757
12	3.074	3.571	4.404	5.226	6.304	18.549	21.026	23.337	26.217	28.300
13	3.565	4.107	5.009	5.892	7.042	19.812	22.362	24.736	27.688	29.819
14	4.075	4.660	5.629	6.571	7.790	21.064	23.685	26.119	29.141	31.319
15	4.601	5.229	6.262	7.261	8.547	22.307	24.996	27.488	30.578	32.801
16	5.142	5.812	6.908	7.962	9.312	23.542	26.296	28.845	32.000	34.267
17	5.697	6.408	7.564	8.672	10.085	24.769	27.587	30.191	33.409	35.718
18	6.265	7.015	8.231	9.390	10.865	25.989	28.869	31.526	34.805	37.156
19	6.844	7.633	8.907	10.117	11.651	27.204	30.144	32.852	36.191	38.582
20	7.434	8.260	9.591	10.851	12.443	28.412	31.410	34.170	37.566	39.997
21	8.034	8.897	10.283	11.591	13.240	29.615	32.671	35.479	38.932	41.401
22	8.643	9.542	10.982	12.338	14.041	30.813	33.924	36.781	40.289	42.796
23	9.260	10.196	11.689	13.091	14.848	32.007	35.172	38.076	41.638	44.181
24	9.886	10.856	12.401	13.848	15.659	33.196	36.415	39.364	42.980	45.559
25	10.520	11.524	13.120	14.611	16.473	34.382	37.652	40.646	44.314	46.928
26	11.160	12.198	13.844	15.379	17.292	35.563	38.885	41.923	45.642	48.290
27	11.808	12.879	14.573	16.151	18.114	36.741	40.113	43.195	46.963	49.645
28	12.461	13.565	15.308	16.928	18.939	37.916	41.337	44.461	48.278	50.993
29	13.121	14.256	16.047	17.708	19.768	39.087	42.557	45.722	49.588	52.336
30	13.787	14.953	16.791	18.493	20.599	40.256	43.773	46.979	50.892	53.672
40	20.707	22.164	24.433	26.509	29.051	51.805	55.758	59.342	63.691	66.766
50	27.991	29.707	32.357	34.764	37.689	63.167	67.505	71.420	76.154	79.490
60	35.534	37.485	40.482	43.188	46.459	74.397	79.082	83.298	88.379	91.952
70	43.275	45.442	48.758	51.739	55.329	85.527	90.531	95.023	100.425	104.215
80	51.172	53.540	57.153	60.391	64.278	96.578	101.879	106.629	112.329	116.321
90	59.196	61.754	65.647	69.126	73.291	107.565	113.145	118.136	124.116	128.299
100	67.328	70.065	74.222	77.929	82.358	118.498	124.342	129.561	135.807	140.169

Figure A.2: Tabulated values of χ^2 for different degrees of freedom. The values on top of each column denote the probability that a hypothesis is not true. Table from [140].

Appendix B

Neutrino oscillations

There are several intrinsic properties of the neutrino that are a matter of intensive research. There is the question, whether the neutrino is Majorana- (neutrino and anti-neutrino are identical) or Dirac-like (neutrino and anti-neutrino are different particles) [141]. Moreover, the absolute mass of the particle is unknown, which is searched for by energy endpoint measurements of the electrons released in tritium decays or in neutrinoless double beta-decay experiments, if the neutrino is Majorana-like. It is known that the number of active light neutrinos is three, yet there is still the question, if there could be sterile neutrinos. However, all these properties do not play any role in studying neutrino sources, as we do in this thesis. Therefore, we omit a further discussion.

Another important aspect of the intrinsic neutrino properties are neutrino oscillations. In this thesis, we do not study neutrino oscillations in detail, but use results obtained by several experiments. Indeed, the exact values of the oscillation parameters play a subdominant role, when studying both terrestrial neutrinos and reactor neutrinos as well as diffuse supernova neutrinos. Nevertheless, we will shortly discuss the principles of neutrino oscillations and display some equations to calculate the oscillation probabilities.

Quantum mechanically, each neutrino state can be described as a superposition of states defined in a certain basis. In neutrino oscillations one generally uses two bases, the mass eigenstate basis with the elements ν_1, ν_2, ν_3 and the flavor eigenstate basis with ν_e, ν_μ, ν_τ. The flavor eigenstates are also the eigenstates of the weak interaction and are not identical to the mass states. Therefore, we can introduce a unitary 3×3 matrix U that describes the transition between the two bases. The transition can be written in the form $U = U_{23} \cdot U_{13} \cdot U_{12}$, where U_{12} describes the rotation between the ν_1, ν_2-sector and the ν_e, ν_μ-sector, and so on. Thus the transition corresponds to three subsequent rotations with phase angles θ_{12}, θ_{23} and θ_{13}. Additionally,

one can account for possible CP violation a Dirac phase δ. All together, we have for the transformation matrix

$$U = \begin{pmatrix} c_{12}c_{13} & s_{12}c_{13} & s_{13}\,e^{-i\delta} \\ -s_{12}c_{23} - c_{12}s_{23}s_{13}e^{i\delta} & c_{12}c_{23} - s_{12}s_{23}s_{13}e^{i\delta} & s_{23}c_{13} \\ s_{12}s_{23} - c_{12}c_{23}s_{13}e^{i\delta} & -c_{12}s_{23} - s_{12}c_{23}s_{13}e^{i\delta} & c_{23}c_{13} \end{pmatrix}, \quad \text{(B.1)}$$

where we have used the usual notations $c_{ij} = \cos\theta_{ij}$, $s_{ij} = \sin\theta_{ij}$ [142, 143, 144]. In case of Majorana neutrinos we have two additional phases that can be included with the matrix $\mathrm{diag}(1, \exp i\alpha, \exp i\beta)$.

The neutrino flavor eigenstates are related to the mass eigenstates by

$$|\nu\rangle_\alpha = \sum_i U^*_{\alpha i} \, |\nu\rangle_i \, . \quad \text{(B.2)}$$

The time-evolution of the mass eigenstates can be described with the usual Schrödinger equation[1]

$$i\frac{d}{dt}\,|\nu\rangle_i = \hat{H}\,|\nu\rangle_i = m_i\,|\nu\rangle_i \quad \text{(B.3)}$$

and

$$|\nu(t)\rangle_i = e^{-i\hat{H}t}\,|\nu(0)\rangle_i = e^{-im_it}\,|\nu(0)\rangle_i \, . \quad \text{(B.4)}$$

We only consider relativistic neutrinos, where $E_\nu \gg m_\nu$ and the propagation distance $x \approx t$. Hence we can express

$$m_i t = E_i t - p_i x = E_i t - x\sqrt{E_i^2 - m_i^2} \sim \frac{m_i^2 x}{2E} = \frac{m_i^2 L}{2E} \, , \quad \text{(B.5)}$$

where the baseline L is the distance between neutrino generation and detection. Combining Eq. (B.5) with Eq. (B.2) and Eq. (B.4) we can calculate the probability $P_{\alpha\to\beta}$ for a flavor transition after time t from the square of the amplitude in the following way

$$\begin{aligned} P_{\alpha\to\beta} = |\,\langle\nu_\beta|\nu(t)\rangle\,|^2 &= \left|\sum_k U_{\alpha k} e^{-i\frac{m_k^2}{2E}L}\,\langle\nu_\beta|\nu_k\rangle\right|^2 \\ &= \left|\sum_{k,j} U^*_{\beta j} U_{\alpha k} e^{-i\frac{m_k^2}{2E}L}\,\langle\nu_j|\nu_k\rangle^2\right|^2 \\ &= \left|\sum_k U^*_{\beta k} U_{\alpha k} e^{-i\frac{m_k^2}{2E}L}\right|^2 \\ &= \sum_{k,j} U_{\alpha k} U^*_{\beta k} U^*_{\alpha j} U_{\beta j} e^{-i\frac{\Delta m^2_{kj}}{2E}L} \end{aligned} \quad \text{(B.6)}$$

[1]Note that we use natural units, $\hbar = c = 1$.

with $\Delta m^2_{kj} = m^2_k - m^2_j$. One can calculate the oscillation probabilities that occur in measurements of reactor, solar and atmospheric neutrinos as

$$\begin{aligned} P_{e\to e} &\approx 1 - \sin^2 2\theta_{13} \sin^2 \tfrac{\Delta m^2_{32} L}{4E} && \text{(reactor)} \\ P_{\mu\to\mu} &\approx 1 - 4\cos^2\theta_{13}\sin^2\theta_{23}(1-\cos^2\theta_{13})\sin^2 \tfrac{\Delta m^2_{32} L}{4E} && \text{(atmospheric)} \\ P_{e\to e} &\approx c^4_{13}(1 - \sin^2 2\theta_{12}\sin^2 \tfrac{\Delta m^2_{21} L}{4E}) + s^4_{13} && \text{(solar).} \end{aligned} \tag{B.7}$$

Hereby we have neglected the subdominant contributions to the oscillation probabilities. Precisely, we have neglected CP violation and the contribution from $\sin^2 \frac{\Delta m^2_{12} L}{4E} \approx 0$ for reactor and atmospheric neutrinos, as we have here only short baselines (~ 1 km) and low energies (< 10 MeV) and can assume that the neutrinos with mass eigenstate ν_1 and ν_2 are quasi-degenerate. For solar neutrinos we can average $\sin^2 \frac{\Delta m^2_{23} L}{4E} \approx 0.5$, because of the long baseline.

The current best-fit values of the mixing angles and the solar and atmospheric mass squared differences, $\Delta m^2_\odot = \mathrm{m}^2_2 - \mathrm{m}^2_1$ and $\Delta m^2_\mathrm{A} = \mathrm{m}^2_3 - \mathrm{m}^2_1$, and their 1, 2 and $3\,\sigma$ ranges are according to Refs. [145, 146]:

$$\begin{aligned} \Delta m^2_\odot &= \left(7.9^{+0.3,\,0.6,\,1.0}_{-0.3,\,0.6,\,0.8}\right) \times 10^{-5}\ \mathrm{eV}^2\ , \\ \sin^2\theta_{12} &= 0.31^{+0.02,\,0.06,\,0.09}_{-0.03,\,0.05,\,0.07}\ , \\ \Delta m^2_\mathrm{A} &= \left(2.2^{+0.37,\,0.7,\,1.1}_{-0.27,\,0.5,\,0.8}\right) \times 10^{-3}\ \mathrm{eV}^2\ , \\ \sin^2\theta_{23} &= 0.50^{+0.06,\,0.14,\,0.18}_{-0.05,\,0.12,\,0.16}\ , \\ \sin^2\theta_{13} &< 0.012\ (0.028,\ 0.046)\ . \end{aligned} \tag{B.8}$$

The present best-fit value for $\sin^2\theta_{13}$ is 0 and there is no information on any of the phases. CP violating effects ($\delta \neq 0$) require all mixing angles to be non-zero.

Acknowledgments

Zum Schluss möchte ich einigen Leuten danken ohne die meine Dissertation heute so nicht aussehen würde. Zum einen möchte ich Lothar Oberauer für das Beantworten verschiedenster Fragen und für die wunderbare Zusammenarbeit danken. Mein besonderer Dank gilt auch Manfred Lindner für die ausgezeichnete Zusammenarbeit. Ausserdem möchte ich Georg Raffelt für die Betreuung am MPI danken. Meine hervorragenden Korrekturleser dürfen natürlich nicht unerwähnt bleiben: Vielen Dank an Martin Hofmann, Joachim Kopp und Michael Wurm. Desweiteren will ich mich noch bei einigen Leuten bedanken, die mich in den vergangenen fast 3 Jahren begleitet haben.

- Das ganze E15-Team und alle, die in dessen Dunstkreis stehen für die super Stimmung.
- Wurmi, Martin, Nils, Jürgen für Rollenspiele, Schafkopfen, Munchkin etc.
- Joachim für die guten Diskussionen und vor allem die vielen Bergtouren
- Martin für den Schlusssatz "da steh ich nun ich armer Tor..." :-) Danke, dass Du ein Walter warst!
- Allen meinen Freunden für die Zerstreuung ausserhalb der Doktorarbeit
- Meine Dankbarkeit und Liebe für Dich, Chrissi, lässt sich nicht in Worte fassen. Deine Unterstützung und Deine Geduld waren gerade in der Endphase furchtbar nötig. Sorry auch für das "Leid", dass ich manches andere vergessen hatte :-).
- Meinen Eltern, Karl und Angela, ohne die es nicht möglich gewesen wäre diese 2 Buchstaben vor dem Namen zu bekommen. Das hättet Ihr wohl vor 27 Jahren auch nicht gedacht :-) Aber auch, wenn ich weit weg war habt ihr mich immer unterstützt und seid mir in allen guten und schlechten Phasen beigestanden.

- Und so schliesse ich nun-nein, nicht mit "...und bin so klug als wie zuvor" :-) - sondern mit:
  "All that is gold does not glitter,
  Not all those who wander are lost;
  The old that is strong does not wither,
  Deep roots are not reached by the frost."

Bibliography

[1] B. T. Cleveland *et al.*, "Measurement of the solar electron neutrino flux with the Homestake chlorine detector," Astrophys. J. **496**, 505 (1998).

[2] J. N. Bahcall, M. H. Pinsonneault and S. Basu, "Solar models: Current epoch and time dependences, neutrinos, and helioseismological properties," Astrophys. J. **555**, 990 (2001) [arXiv:astro-ph/0010346].

[3] Y. Ashie *et al.* [Super-Kamiokande Collaboration], "Evidence for an oscillatory signature in atmospheric neutrino oscillation," Phys. Rev. Lett. **93**, 101801 (2004) [arXiv:hep-ex/0404034].

[4] B. Aharmim *et al.* [SNO Collaboration], "Electron energy spectra, fluxes, and day-night asymmetries of B-8 solar neutrinos from the 391-day salt phase SNO data set," Phys. Rev. C **72**, 055502 (2005) [arXiv:nucl-ex/0502021].

[5] T. Araki *et al.* [KamLAND Collaboration], "Measurement of neutrino oscillation with KamLAND: Evidence of spectral distortion," Phys. Rev. Lett. **94** (2005) 081801 [hep-ex/0406035].

[6] F. Ardellier *et al.* (Double Chooz Collaboration), "Double Chooz: A search for the neutrino mixing angle θ_{13}," hep-ex/0606025v4 (26 October 2006).

[7] P. Huber, M. Lindner and W. Winter, "Simulation of long-baseline neutrino oscillation experiments with GLoBES," Comput. Phys. Commun. **167**, 195 (2005) [arXiv:hep-ph/0407333].

[8] P. Huber, M. Lindner and W. Winter, "Superbeams versus neutrino factories," Nucl. Phys. B **645**, 3 (2002) [arXiv:hep-ph/0204352].

[9] A. Osipowicz *et al.* [KATRIN Collaboration], "KATRIN: A next generation tritium beta decay experiment with sub-eV sensitivity for the electron neutrino mass," arXiv:hep-ex/0109033.

[10] H. V. Klapdor-Kleingrothaus, A. Dietz, H. L. Harney and I. V. Krivosheina, "Evidence for neutrinoless double beta decay," Mod. Phys. Lett. A **16**, 2409 (2001) [arXiv:hep-ph/0201231].

[11] A. M. Bakalyarov *et al.*, "GERDA, Progress Report to the LNGS SC," October 2007, Version 1.0, available at: http://www.mpi-hd.mpg.de/ge76/

[12] T. Bloxham *et al.* [COBRA collaboration], "First results on double beta decay modes of Cd, Te and Zn isotopes with the COBRA experiment," Phys. Rev. C **76**, 025501 (2007) [arXiv:0707.2756 [nucl-ex]].

[13] W. Buchmuller, P. Di Bari and M. Plumacher, "Leptogenesis for pedestrians," Annals Phys. **315**, 305 (2005) [arXiv:hep-ph/0401240].

[14] J. Ahrens *et al.* [IceCube Collaboration], "Sensitivity of the IceCube detector to astrophysical sources of high energy muon neutrinos," Astropart. Phys. **20**, 507 (2004) [arXiv:astro-ph/0305196].

[15] Borexino Collaboration, "First real time detection of Be7 solar neutrinos by Borexino," Phys. Lett. B **658**, 101 (2008) [arXiv:0708.2251 [astro-ph]].

[16] B. D. Fields and K. A. Hochmuth, "Imaging the earth's interior: The angular distribution of terrestrial neutrinos," Earth Moon Planets **99**, 155 (2006) [arXiv:hep-ph/0406001].

[17] T. Araki *et al.*, "Experimental investigation of geologically produced antineutrinos with KamLAND," Nature **436** (2005) 499.

[18] M. Apollonio *et al.* [CHOOZ Collaboration], "Determination of neutrino incoming direction in the CHOOZ experiment and its application to supernova explosion location by scintillator detectors," Phys. Rev. D **61** (2000) 012001 [hep-ex/9906011].

[19] T. Totani, K. Sato, H. E. Dalhed and J. R. Wilson, "Future detection of supernova neutrino burst and explosion mechanism," Astrophys. J. **496**, 216 (1998) [arXiv:astro-ph/9710203].

[20] T. A. Thompson, A. Burrows and P. A. Pinto, "Shock breakout in core-collapse supernovae and its neutrino signature," Astrophys. J. **592**, 434 (2003) [arXiv:astro-ph/0211194].

[21] M. T. Keil, G. G. Raffelt and H. T. Janka, "Monte Carlo study of supernova neutrino spectra formation," Astrophys. J. **590**, 971 (2003) [arXiv:astro-ph/0208035].

[22] M. Malek *et al.* [Super-Kamiokande Collaboration], "Search for supernova relic neutrinos at Super-Kamiokande," Phys. Rev. Lett. **90**, 061101 (2003) [arXiv:hep-ex/0209028].

[23] M. Wurm, F. von Feilitzsch, M. Göger-Neff, K. A. Hochmuth, T. Marrodán Undagoitia, L. Oberauer and W. Potzel, "Detection potential for the diffuse supernova neutrino background in the large liquid-scintillator detector LENA," Phys. Rev. D **75**, 023007 (2007) [arXiv:astro-ph/0701305].

[24] T. Marrodán Undagoitia, F. von Feilitzsch, M. Göger-Neff, K. A. Hochmuth, L. Oberauer, W. Potzel and M. Wurm, "Low energy neutrino astronomy with the large liquid scintillation detector LENA," Prog. Part. Nucl. Phys. **57**, 283 (2006) [J. Phys. Conf. Ser. **39**, 278 (2006)] [arXiv:hep-ph/0605229].

[25] H. O. Back *et al.* [Borexino Collaboration], "Phenylxylylethane (PXE): A high-density, high-flashpoint organic liquid scintillator for applications in low-energy particle and astrophysics experiments," arXiv:physics/0408032.

[26] M. Wurm, "Untersuchungen zu den optischen Eigenschaften eines Flüssigszintillators und zum Nachweis von Supernovae Relic Neutrinos mit LENA", Diploma thesis, TU München, Germany (2005).

[27] L. Oberauer, private communications

[28] J. Hejwowski and A. Szymanski, "Lithium loaded liquid scintillator," Review of Scientific Instruments **32** (1961) 1057–1058.

[29] F. Ardellier *et al.*, "Letter of intent for double-CHOOZ: A search for the mixing angle theta(13)," hep-ex/0405032.

[30] T. Marrodán Undagoitia, F. v. Feilitzsch, M. Göger-Neff, C. Grieb, K. A. Hochmuth, L. Oberauer, W. Potzel, M. Wurm, "Search for the proton decay $p \to K^+\bar{\nu}$ in the large liquid scintillator low energy neutrino astronomy detector LENA," Phys. Rev. D **72** (2005) 075014 [hep-ph/0511230].

[31] P. Huber, M. Lindner, M. Rolinec and W. Winter, "Physics and optimization of beta-beams: From low to very high gamma," Phys. Rev. D **73**, 053002 (2006) [arXiv:hep-ph/0506237].

[32] A. A. Aguilar-Arevalo *et al.* [The MiniBooNE Collaboration], "A Search for electron neutrino appearance at the $\Delta m^2 \sim 1\mathrm{eV}^2$ scale," Phys. Rev. Lett. **98**, 231801 (2007) [arXiv:0704.1500 [hep-ex]].

[33] C. Athanassopoulos *et al.* [LSND Collaboration], "Candidate events in a search for anti-muon-neutrino → anti-electron-neutrino oscillations," Phys. Rev. Lett. **75**, 2650 (1995) [arXiv:nucl-ex/9504002].

[34] D. Autiero *et al.*, "Large underground, liquid based detectors for astroparticle physics in Europe: scientific case and prospects," JCAP **0711**, 011 (2007) [arXiv:0705.0116 [hep-ph]].

[35] A. G. Cocco, A. Ereditato, G. Fiorillo, G. Mangano and V. Pettorino, "Supernova relic neutrinos in liquid argon detectors," JCAP **0412**, 002 (2004) [arXiv:hep-ph/0408031].

[36] W. E. Ormand, P. M. Pizzochero, P. F. Bortignon and R. A. Broglia, "Neutrino Capture Cross-Sections For Ar-40 And Beta Decay Of Ti-40," Phys. Lett. B **345**, 343 (1995) [arXiv:nucl-th/9405007].

[37] J. F. Beacom and M. R. Vagins, "GADZOOKS! Antineutrino spectroscopy with large water Cherenkov detectors," Phys. Rev. Lett. **93**, 171101 (2004) [arXiv:hep-ph/0309300].

[38] http://mahi.ucsd.edu/Gabi/sediment.html

[39] http://www.solarviews.com/eng/earthint.htm

[40] http://www.wissenschaft-online.de/abo/lexikon/geo/4244

[41] http://www.seismo.unr.edu/ftp/pub/louie/class/100/interior.html

[42] http://erde.adlexikon.de/Erde.shtml

[43] A. M. Dziewonski and D. L. Anderson, "Preliminary Reference Earth Model," Phys. Earth Planet. Interiors **25** (1981) 297. For a tabulation see `http://solid_Earth.ou.edu/prem.html`

[44] http://www.meteorite.fr/en/classification/carbonaceous.htm

[45] W. F. McDonough and S.-S. Sun, "The composition of the Earth," Chem. Geol. **120** (1995) 223.

[46] http://atom.kaeri.re.kr/

[47] A. M. Hofmeister, R. E. Criss, "Earth's heat flux revised and linked to chemistry," Tectonophysics, **409**, iss. 1-4, 2005, p. 193-198

[48] C. Stein, in Global Earth Physics: A Handbook of Physical Constants, AGU Reference Shelf 1, ed. T.J. Ahrens (American Geophysical Union, Washington, 1995), 144.

[49] D. McKenzie, F. Richter, "Parameterized thermal convection in a layered region and the thermal history of the earth." J. Geophys. Res. , Vol. 86, p. 11667 - 11680(1981)

[50] W. R. Van Schmus, "Natural Radioactivity of the Crust and Mantle", Global Earth Physics: A Handbook of Physical Constants, AGU Reference Shelf 1, ed. T.J. Ahrens (American Geophysical Union, Washington, 1995), 283.

[51] http://earthref.org/

[52] S. Labrosse, J. -P. Poirier, J. -P. Le Mouël, "The age of the inner core", Earth Planet. Sci. Lett. **190** (2001) 111-123

[53] J. Wasserburg, J. Gordon, F. MacDonald, F. Hoyle, W. A. Fowler, "Relative Contributions of Uranium, Thorium, and Potassium to Heat Production in the Earth," Science **143**, pp.465 (1964)

[54] M. Humayun and R. N. Clayton, "Potassium isotope cosmochemistry: Genetic implications of volatile element depletion," Geochim. Cosmochim. Acta, 59(10), 2131 2148, 1995.

[55] H. T. Hall and V. R. Murthy, "The early chemical history of the Earth: Some critical elemental fractionations," Earth Planet. Sci. Lett. , **11**, 239, 244 (1971)

[56] J. S. Lewis, "Consequences of the presence of sulfur in the core of the Earth," Earth Planet. Sci. Lett. , **11**, 130, 134 (1971)

[57] C. K. Gessmann, B. J. Wood, "Potassium in Earth's Core?," Earth Planet. Sci. Lett, **200**, p.63-78 (2002)

[58] V. Rama Murthy, W. van Westrenen, Y. Fei, "Experimental evidence that potassium is a substantial radioactive heat source in planetary cores," Nature **423** (2003)

[59] M. S. T. Bukowinski, "The effect of pressure on the physics and chemistry of potassium," Geophys. Res. Lett. , **3**, 491, 503 (1976)

[60] K. K. M. Lee, R. Jeanloz, "High-pressure alloying of potassium and iron: Radioactivity in the Earth'score?," Geophys. Res. Lett, **30** (2003)

[61] J. M. Herndon, J.Geomagn. Geoelectr. 45 (1993) 423

[62] W. Seifritz, "Some comments on Herndon's nuclear georeactor," Kerntechnik 68 (2003) 4, p.193-196

[63] D. F. Hollenbach and J. M. Herndon, "Deep-Earth Reactor: Nuclear Fission, He, and the Geomagnetic Field," PNAS, USA, Vol. 98, issue 20, pp. 11 055-11 090 (2001)

[64] J. M. Herndon, "Nuclear Georeactor Origin of Oceanic Basalt He3/He4, Evidence, and Implications," PNAS, March 18 (2003), Vol. 100, No. 6, pp. 30473050

[65] K. T. Wheeler, D. Walker, Y. Fei, W. G. Minarik, W. F. McDonough, "Experimental partitioning of uranium between liquid iron sulfide and liquid silicate: Implications for radioactivity in the Earths core," Geochimica et Cosmochimica Acta, **70**, iss. 6, 2006, p. 1537

[66] N. Schmitz, "Neutrinophysik", Teubner Studienbcher 1997

[67] P. Vogel and J. F. Beacom, "Angular distribution of neutron inverse beta decay, $\bar{\nu}_e + p \to e^+ + n$," Phys. Rev. D **60** (1999) 053003 [hep-ph/9903554].

[68] L. Oberauer, C. Grieb, F. von Feilitzsch and I. Manno, "Light concentrators for Borexino and CTF," Nucl. Instrum. Meth. A **530**, 453 (2004) [arXiv:physics/0310076].

[69] G. Alimonti *et al.*, "A large-scale low-background liquid scintillation detector: The counting test facility at Gran Sasso," Nucl. Instrum. Meth. A **406**, 411 (1998).

[70] M. Apollonio *et al.*, "Search for neutrino oscillations on a long base-line at the CHOOZ nuclear power station," Eur. Phys. J. C **27**(2003) 331 [hep-ex/0301017].

[71] F. Mantovani, L. Carmignani, G. Fiorentini and M. Lissia, "Antineutrinos from the earth: The reference model and its uncertainties," Phys. Rev. D **69**, 013001 (2004) [arXiv:hep-ph/0309013].

[72] G. Fiorentini, T. Lasserre, M. Lissia, B. Ricci and S. Schönert, "KamLAND, terrestrial heat sources and neutrino oscillations," Phys. Lett. B **558** (2003) 15 [hep-ph/0301042].

[73] M. Wurm, private communication

[74] G. Zacek *et al.* (CALTECH-SIN-TUM Collaboration), "Neutrino oscillation experiments at the Gösgen nuclear power reactor," Phys. Rev. D **34**, 2621 (1986).

[75] T. Lasserre: private communication

[76] R. M. Bionta *et al.*, "Observation of a Neutrino Burst in Coincidence with Supernova SN 1987a in the Large Magellanic Cloud," Phys. Rev. Lett. **58**, 1494 (1987).

[77] K. Hirata *et al.* [KAMIOKANDE-II Collaboration], "Observation Of A Neutrino Burst From The Supernova Sn 1987a," Phys. Rev. Lett. **58**, 1490 (1987).

[78] S. Ando, "Decaying neutrinos and implications from the supernova relic neutrino observation," Phys. Lett. B **570**, 11 (2003) [arXiv:hep-ph/0307169].

[79] D. N. Spergel *et al.* [WMAP Collaboration], "First Year Wilkinson Microwave Anisotropy Probe (WMAP) Observations: Determination of Cosmological Parameters," Astrophys. J. Suppl. **148**, 175 (2003) [arXiv:astro-ph/0302209].

[80] E. Kolb, M. Turner, "The Early Universe," Westview Press, 1990

[81] S. Ando and K. Sato, "Supernova relic neutrinos and observational implications for neutrino oscillation," Phys. Lett. B **559**, 113 (2003) [arXiv:astro-ph/0210502].

[82] S. Chandrasekhar, "The Highly Collapsed Configurations of a Stellar Mass," Monthly Notices of the Royal Astronomical Society **91** (1931), 456466.

[83] S. Chandrasekhar, "The Highly Collapsed Configurations of a Stellar Mass (second paper)," Monthly Notices of the Royal Astronomical Society, **95** (1935), pp. 207–225.

[84] H. T. Janka, "Neutrinos from type II supernovae and the neutrino driven supernova mechanism," Italian Phys. Soc. Proc. **40**, 345 (1993).

[85] H. T. Janka, R. Buras, K. Kifonidis, T. Plewa and M. Rampp, "Core Collapse and Then? The Route to Massive Star Explosions," arXiv:astro-ph/0212316.

[86] A. Burrows, T. Young, P. Pinto, R. Eastman and T. A. Thompson, "A new algorithm for supernova neutrino transport and some applications," Astrophys. J. **539**, 865 (2000).

[87] S. W. Bruenn, K. R. De Nisco and A. Mezzacappa, "General Relativistic Effects in the Core Collapse Supernova Mechanism," Astrophys. J. **560**, 326 (2001) [arXiv:astro-ph/0101400].

[88] S. Yamada, H. T. Janka and H. Suzuki, "Neutrino transport in type II supernovae Boltzmann solver vs. Monte Carlo method," arXiv:astro-ph/9809009.

[89] G. G. Raffelt, M. T. Keil, R. Buras, H. T. Janka and M. Rampp, "Supernova neutrinos: Flavor-dependent fluxes and spectra," arXiv:astro-ph/0303226.

[90] R. Mayle, J. R. Wilson and D. N. Schramm, "Neutrinos from gravitational collapse," Astrophys. J. **318**, 288 (1987).

[91] H. Suzuki, "Neutrino emission from protoneutron star with modified URCA and nucleon bremsstrahlung processes", Num. Astrophys. Japan, 2:267, 1991.

[92] H. Suzuki, "Supernova neutrinos: Multigroup simulations of neutrinos from protoneutron star", 1993, Prepared for International Symposium on Neutrino Astrophysics, Takayama / Kamioka, Japan, 19-22 Oct 1992.

[93] M. Liebendoerfer, A. Mezzacappa, F. K. Thielemann, O. E. B. Messer, W. R. Hix and S. W. Bruenn, "Probing the gravitational well: No supernova explosion in spherical symmetry with general relativistic Boltzmann neutrino transport," Phys. Rev. D **63**, 103004 (2001) [arXiv:astro-ph/0006418].

[94] R. Buras, M. Rampp, H.-T. Janka, and K. Kifonidis, "Improved models of stellar core collapse and still no explosions: What is missing?", Phys. Rev. Lett., 90:241101, 2003.

[95] M. Th. Keil, "Supernova Neutrino Spectra and Applications to Flavor Oscillations." PhD thesis, Technische Universität München, 2003.

[96] M. T. Keil, G. G. Raffelt and H. T. Janka, "Monte Carlo study of supernova neutrino spectra formation," Astrophys. J. **590**, 971 (2003) [arXiv:astro-ph/0208035].

[97] A. S. Dighe and A. Y. Smirnov, "Identifying the neutrino mass spectrum from the neutrino burst from a supernova," Phys. Rev. D **62**, 033007 (2000) [arXiv:hep-ph/9907423].

[98] C. Lunardini, "The diffuse neutrino flux from supernovae: Upper limit on the electron neutrino component from the non-observation of antineutrinos at superKamiokande," Phys. Rev. D **73**, 083009 (2006) [arXiv:hep-ph/0601054].

[99] G. G. Raffelt and G. Sigl, "Self-induced decoherence in dense neutrino gases," Phys. Rev. D **75**, 083002 (2007) [arXiv:hep-ph/0701182].

[100] G. L. Fogli, E. Lisi, A. Marrone and A. Mirizzi, "Collective neutrino flavor transitions in supernovae and the role of trajectory averaging," JCAP **0712**, 010 (2007) [arXiv:0707.1998 [hep-ph]].

[101] E. Cappellaro, R. Barbon and M. Turatto, "Supernova Statistics," arXiv:astro-ph/0310859.

[102] R. Barbon, V. Buondi', E. Cappellaro and M. Turatto, "The Asiago Supernova Catalogue- 10 years after," arXiv:astro-ph/9908046.

[103] E. Cappellaro, M. Turatto, D. Y. Tsvetkov, O. S. Bartunov, C. Pollas, R. Evans and M. Hamuy, "The rate of Supernovae from the combined sample of five searches," Astron. Astrophys. **322**, 431 (1997) [arXiv:astro-ph/9611191].

[104] J. Leaman, W. Li, and A. Filippenko, "The Supernova Rate in nearby galaxies determined from the Lick Observatory Supernova Search", American Astronomical Society Meeting Abstracts, 205:7102, 2004.

[105] W. M. Wood-Vasey and SNfactory, "Supernova rates from the Nearby Supernova Factory Prototype Search", American Astronomical Society Meeting Abstracts, 205:4003, 2004.

[106] L. Strolger, "The Nearby Galaxies Supernova Search project: The Rate of Supernovae in the Local Universe." PhD thesis, University of Michigan, 2003.

[107] E. Cappellaro, R. Evans and M. Turatto, "A new determination of supernova rates and a comparison with indicators for galactic star formation," Astron. Astrophys. **351**, 459 (1999) [arXiv:astro-ph/9904225].

[108] J. Scalo, "The IMF Revisited: A Case for Variations," arXiv:astro-ph/9712317.

[109] D. W. Hogg, "A meta-analysis of cosmic star-formation history," arXiv:astro-ph/0105280.

[110] I. K. Baldry *et al.*, "The 2dF Galaxy Redshift Survey: constraints on cosmic star-formation history from the cosmic spectrum," Astrophys. J. **569**, 582 (2002) [arXiv:astro-ph/0110676].

[111] L. Hernquist and V. Springel, "An analytical model for the history of cosmic star formation," Mon. Not. Roy. Astron. Soc. **341**, 1253 (2003) [arXiv:astro-ph/0209183].

[112] D. Schiminovich *et al.* [The GALEX-VVDS Collaboration], "The GALEX-VVDS Measurement of the Evolution of the Far-Ultraviolet Luminosity Density and the Cosmic Star Formation Rate," Astrophys. J. **619**, L47 (2005) [arXiv:astro-ph/0411424].

[113] I. K. Baldry and K. Glazebrook, "Constraints on a Universal IMF from UV to Near-IR Galaxy Luminosity Densities," Astrophys. J. **593**, 258 (2003) [arXiv:astro-ph/0304423].

[114] L. E. Strigari, J. F. Beacom, T. P. Walker and P. Zhang, "The concordance cosmic star formation rate: Implications from and for the supernova neutrino and gamma ray backgrounds," JCAP **0504**, 017 (2005) [arXiv:astro-ph/0502150].

[115] O. Tengblad, G. Nyman, K. Aleklett, E. Lund, G. Rudstam and R. Von Dincklage, "Integral anti-neutrino spectra derived from experimental beta spectra of individual fission products," Nucl. Phys. A **503**, 136 (1989).

[116] M. Fukugita and T. Yanagida, "Physics of neutrinos and applications to astrophysics," *Berlin, Germany: Springer (2003) 593 p*

[117] LBNL Isotopes Project, http://ie.lbl.gov/toi.htm.

[118] A. Letourneau and D. Lhuillier, private communication.

[119] V. Kopeikin, L. Mikaelyan and V. Sinev, "Reactor as a source of antineutrinos: Thermal fission energy," Phys. Atom. Nucl. **67**, 1892 (2004) [Yad. Fiz. **67**, 1916 (2004)] [arXiv:hep-ph/0410100].

[120] International Atomic Energy Agency, http://www.iaea.org.

[121] International Nuclear Safety Center, http://www.insc.anl.gov.

[122] K. Eguchi *et al.* [KamLAND Collaboration], "First results from KamLAND: Evidence for reactor anti-neutrino disappearance," Phys. Rev. Lett. **90**, 021802 (2003) [arXiv:hep-ex/0212021].

[123] T. Araki *et al.* [KamLAND Collaboration], "Measurement of neutrino oscillation with KamLAND: Evidence of spectral distortion," Phys. Rev. Lett. **94**, 081801 (2005) [arXiv:hep-ex/0406035].

[124] T. K. Gaisser, T. Stanev and G. Barr, "Cosmic Ray Neutrinos in the Atmosphere," Phys. Rev. D **38**, 85 (1988).

[125] G. Barr, T. K. Gaisser and T. Stanev, "Flux of atmospheric neutrinos," Phys. Rev. D **39**, 3532 (1989).

[126] Y. Liu, L. Derome and M. Buenerd, "Atmospheric muon and neutrino flux from 3-dimensional simulation," Phys. Rev. D **67**, 073022 (2003) [arXiv:astro-ph/0211632].

[127] K. Zbiri and J. Martino, "Physics process of cosmogenics isotopes production on muons interactions with carbon target in liquid scintillator," arXiv:hep-ph/0607179.

[128] T. Enqvist *et al.*, "Measurements of muon flux in the Pyhaesalmi underground laboratory," Nucl. Instrum. Meth. A **554**, 286 (2005) [arXiv:hep-ex/0506032].

[129] V. A. Kudryavtsev, N. J. C. Spooner and J. E. McMillan, "Simulations of muon-induced neutron flux at large depths underground," Nucl. Instrum. Meth. A **505**, 688 (2003) [arXiv:hep-ex/0303007].

[130] T. Hagner, R. von Hentig, B. Heisinger, L. Oberauer, S. Schonert, F. von Feilitzsch and E. Nolte, "Muon induced production of radioactive isotopes in scintillation detectors," Astropart. Phys. **14**, 33 (2000).

[131] S. Agostinelli *et al.* [GEANT4 Collaboration], "GEANT4: A simulation toolkit," Nucl. Instrum. Meth. A **506**, 250 (2003).

[132] A. M. Hopkins and J. F. Beacom, "On the normalisation of the cosmic star formation history," Astrophys. J. **651**, 142 (2006) [arXiv:astro-ph/0601463].

[133] P. Huber, J. Kopp, M. Lindner, M. Rolinec and W. Winter, "New features in the simulation of neutrino oscillation experiments with GLoBES 3.0," Comput. Phys. Commun. **177**, 432 (2007) [arXiv:hep-ph/0701187].

[134] T. Schwetz, "What is the probability that theta(13) and CP violation will be discovered in future neutrino oscillation experiments?," Phys. Lett. B **648**, 54 (2007) [arXiv:hep-ph/0612223].

[135] T. Schwetz, Talk at the GLoBES Workshop, Heidelberg, Germany, 2007

[136] T. J. Loredo and D. Q. Lamb, "Neutrino from SN1987A: Implications for cooling of the nascent neutron star and the mass of the electron anti-neutrino," Annals N. Y. Acad. Sci. **571**, 601 (1989).

[137] T. J. Loredo and D. Q. Lamb, "Bayesian analysis of neutrinos observed from supernova SN 1987A," Phys. Rev. D **65**, 063002 (2002) [arXiv:astro-ph/0107260].

[138] C. Kiessig, Diploma Thesis, Technische Universitaet Muenchen, Germany, 2005

[139] W. -M. Yao *et al.* , Journal of Physics G 33, 1 (2006), Particle Data Group Review on "Statistics"

[140] http://people.richland.edu/james/lecture/m170/tbl-chi.html

[141] E. K. Akhmedov, "Neutrino physics," arXiv:hep-ph/0001264.

[142] S. M. Bilenky, J. Hosek and S. T. Petcov, " On oscillstions of neutrinos with Dirac and Majorana masses" Phys. Lett. B **94**, 495 (1980);

[143] J. Schechter and J. W. F. Valle, "Neutrino Masses In SU(2) X U(1) Theories," Phys. Rev. D **22**, 2227 (1980).

[144] M. Doi, T. Kotani, H. Nishiura, K. Okuda and E. Takasugi, "CP Violation In Majorana Neutrinos," Phys. Lett. B **102**, 323 (1981).

[145] T. Schwetz, "Neutrino oscillations: Current status and prospects," Acta Phys. Polon. B **36**, 3203 (2005) [arXiv:hep-ph/0510331].

[146] M. Maltoni, T. Schwetz, M. A. Tortola and J. W. F. Valle, "Status of global fits to neutrino oscillations," New J. Phys. **6**, 122 (2004) [arXiv:hep-ph/0405172].